Research Project Office

Technical Report

Accelerator Transmutation of Waste Project

Compendium of Initial System Point Designs for Accelerator Transmutation of Radioactive Waste

This page intentionally left blank

Compendium of Initial System Point Designs for Accelerator Transmutation of Radioactive Waste

Document Number: AAA-RPO-SYS-01-0008

Alternate Document Number: LA-UR-01-1817

Revision 0

February 2001

Abstract:

This document is a compendium of System Point Design information prepared during the summer of 2000 for the Department of Energy, Office of Nuclear Energy under the auspices of the Accelerator Transmutation of Waste (ATW) Program. The compendium was prepared using multi-institutional teams composed of staff from Los Alamos National Laboratory, Argonne National Laboratory, and Brookhaven National Laboratory. Contributing information was also provided by General Atomics. The compendium is intended to serve as a preliminary basis for concept evaluation of accelerator-driven transmutation systems with various combinations of blanket configurations and coolant, such as sodium, lead bismuth eutectic, gas and molten salt. The assessments focus predominately on nuclear transmutation performance rather than integrated systems.

Principal Author: *Signature on file*

AAA-RPO   Deborah Bennett, February 2001

Contributors:

Los Alamos National Laboratory   *Argonne National Laboratory*
Eric Pitcher   Hussein Khalil
Holly Trellue   Phillip Finck
Dave Poston   Bob Hill
Denis Beller   Won Sik Yang
Deborah Bennett   Temitope Taiwo
                                         Yousry Gohar

Brookhaven National Laboratory
Mike Todosow

Recommended for Approval:

Project Leader   *Signature on file*

AAA-RPO   Gregory J. Van Tuyle, February 2001

Distribution List

AAA Project File	H816
RMDC (BREI)	C341
Quintana, Lawrence (QA) 2 copies	H816
John Herczeg	DOE/NE-20
Frank Goldner	DOE/NE-20
Norton Haberman	DOE/NE-20
Jim Bresee	DOE/NE-20
Tom Ward	DOE/NE-20
Jack Metzler	DOE/DP
Sam Espinosa	DOE-ALO
JoAnn Torres	DOE-ALO
Ed Arthur	LANL
Bruce Matthews	LANL
Greg VanTuyle	LANL
Mike Cappiello	LANL
Steve McConnell	LANL
Kemal Pasamehmetoglu	LANL
Eric J. Pitcher	LANL
Holly Trellue	LANL
Chuck Bathke	LANL
Shelly Spearing	LANL
Kim Thomas	LANL
Bob Krakowski	LANL
Wiley Davidson	LANL
Dave Poston	LANL
Dave Hill	ANL
Phillip Finck	ANL
Hussein Khalil	ANL
Bob Hill	ANL
Yousry Gohar	ANL
Jordi Roglans	ANL
Jim Laidler	ANL
Doug Crawford	ANL
Bill Halsey	LLNL
Mike Todosow	BNL
Carmello Rodriguez	GAT
Alan Baxter	GAT

Table of Contents

List of Figures

List of Tables

Acronyms

AAA	Advanced Accelerator Applications
AD-MHR	Accelerator-Driven Modular Helium Reactor
ADS	Accelerator-Driven System
ALMR	Advanced Liquid Metal Reactor
Am-242m	metastable isotope of Americium
AMSB	Accelerated Molten Salt Breeder
ANL	Argonne National Laboratory
ATW	Accelerator Transmutation of Waste
BOC	Beginning-Of-Cycle
BOEC	Beginning-Of-Equilibrium-Cycle
BOL	Beginning-Of-Life
BP	Burnable Poison
BREI	Burns and Roe Enterprises, Inc.
BRUS-300	an LBE-cooled Russian reactor
D	Diameter
DIF3D	neutronics code for finite-difference diffusion theory problem solving
DRAGON	a lattice code
EADC	End of Accelerator-Driven Cycle
EBR-II	Experimental Breeder Reactor II
ECOC	End of Critical Operation Cycle
EFDA	European Fusion Development Agreement
efpd	effective full-power days
ENDF/B-V.2	Evaluated Nuclear Data File
EOB	End-Of-Burn
EOC	End-Of-Cycle
EOEC	End-Of-Equilibrium-Cycle
eV	electron Volt
FFTF	Fast Flux Test Facility
FP	Fission Product
GA	General Atomics
GCFR	Gas-Cooled Fast Reactor
GeV	Giga-electron Volt
GT/AD-MHR	Gas Turbine/Accelerator-Driven Modular Helium Reactor
GT-MHR	Gas Turbine Modular Helium Reactor
GWt	Gigawatt-thermal—a unit of thermal power
HT-9	an austenitic or martensitic stainless steel cladding material
ICF	Inertial Confinement Fusion
IFR	Integral Fast Reactor
IHX	Intermediate Heat Exchanger
ITC	Isothermal Temperature Coefficient
ITER	International Tokamak Experimental Reactor
JEF	Joint Evaluated File—library of neutron reaction data
JET	Joint European Torus—A tokomak facility in Culham, England run under the auspices of the EFDA
KgHM	Kilograms of Heavy Metal
kW/ℓ	kilowatts per liter—a unit of power density
LANL	Los Alamos National Laboratory
LBE	Lead-Bismuth Eutectic
LLFP	Long-Lived Fission Product

LINAC	LINear ACcelerator
LMR	Liquid Metal Reactor
LWR	Light Water Reactor
mA	milli-Ampere
MA	Minor Actinides
MC2-2	a code to calculate fast neutron spectra and multi-group cross sections
MCNP	a Monte Carlo N-Particle code
MCNP-VA	a Monte Carlo code for simulating neutral particle transport
MeV	Mega-electron Volt
MHR	Modular Helium Reactor
MONK	a Monte Carlo code for nuclear criticality safety and reactor physics analyses
MPa	Mega-Pascal—a unit of residual stress/pressure
MS	Molten Salt
MSR	Molten Salt Reactor
MW	Megawatt—a unit of power
MW/m^2	Megawatts per square meter—a unit of power density
MWd	Megawatt days
MWd/MT	Megawatt days per metric ton of heavy metal
MWth	Megawatt thermal—a unit of thermal power
MWthD	Megawatt thermals per day
n/cm2	neutrons per square centimeter—a unit of neutron fluence
NEA	Nuclear Energy Agency
NERAC	Nuclear Energy Research Advisory Committee
NSSS	Nuclear Steam Supply System
OD	Outer Diameter
OECD	Organization for Economic Cooperation and Development
ORIGEN	a computer code system for calculating the buildup, decay, and processing of radioactive materials
ORNL	Oak Ridge National Laboratory
P/D	Pitch-to-Diameter
pcm	per cent mille—10^{-5}
PF	Packing Factor
PRISM	Power Reactor Innovative Small Module ALMR
PUREX	Plutonium URanium Extraction—Commonly used process based on using tributylphosphate for fuel reprocessing
PWR	pressurized water reactor
PyC	PyroCarbon
PYRO-A	pyrochemical technique for separating TRU from SNF during the ATW fuel fabrication process
PYRO-B	pyrochemical technique for separating TRU during post-transmutation processing
R&D	Research and Development
REBUS-3	reactor fuel-cycle analysis code
RMDC	Records Management Document Control
RPO	Research Project Office
SDX	Space Dependent cross-section generation computer code
SPD	System Point Design
ST	Spherical Tokamak
TFTR	Tokamak Fusion Test Reactor
TRU	TRansUranic elements
TTW	Tokamak Transmutation of Waste
UREX	URanium Extraction—An aqueous process for processing spent fuel
VARIANT	a nodal transport and diffusion module for DIF3D

VIM	a continuous-energy Monte Carlo neutron/photon transport code
W/cc	Watts per cubic centimeter, a unit of power density
W/m^{2}K	Watts per square-meter-Kelvin—a unit of thermal transmittance
W/mK	Watts per meter-Kelvin—a unit of thermal conductivity

1   Introduction

This document is a compendium of System Point Design (SPD) information prepared during the summer of 2000 for the Department of Energy, Office of Nuclear Energy under the auspices of the Accelerator Transmutation of Waste (ATW) Program. The compendium was prepared using multi-institutional teams composed of staff from Los Alamos National Laboratory, Argonne National Laboratory, and Brookhaven National Laboratory. Contributing information was also provided by General Atomics.

The compendium is intended to serve as a preliminary basis for concept evaluation of accelerator–driven transmutation systems with various combinations of blanket configurations and coolant, such as sodium, lead bismuth eutectic, gas and molten salt. Its assessments focus predominately on nuclear transmutation performance rather than assessments of integrated systems, which would naturally include separations and fabrication processes, as well as the design elements of the accelerator.

1.1 Background

A Decision Framework was established early in January 2000, anticipating the technology choices that would need to be made in the progress of the program. The purpose of the framework was to help ensure that the program mission and objectives were met with technical credibility, and to serve as the basis for determining analytical and experimental activities.

The Decision Framework, schematically represented in Figure 1-1, assumes that the primary program objective was to:

> Determine whether and how ATW can provide a *practical* means to achieving *meaningful* reduction of transuranic and fission product isotopes in the nuclear waste stream.

The intent was to concurrently understand what information and data was already available via the knowledge map, but more importantly to perform system point design evaluations before determining the scope of the R&D needed for the program.
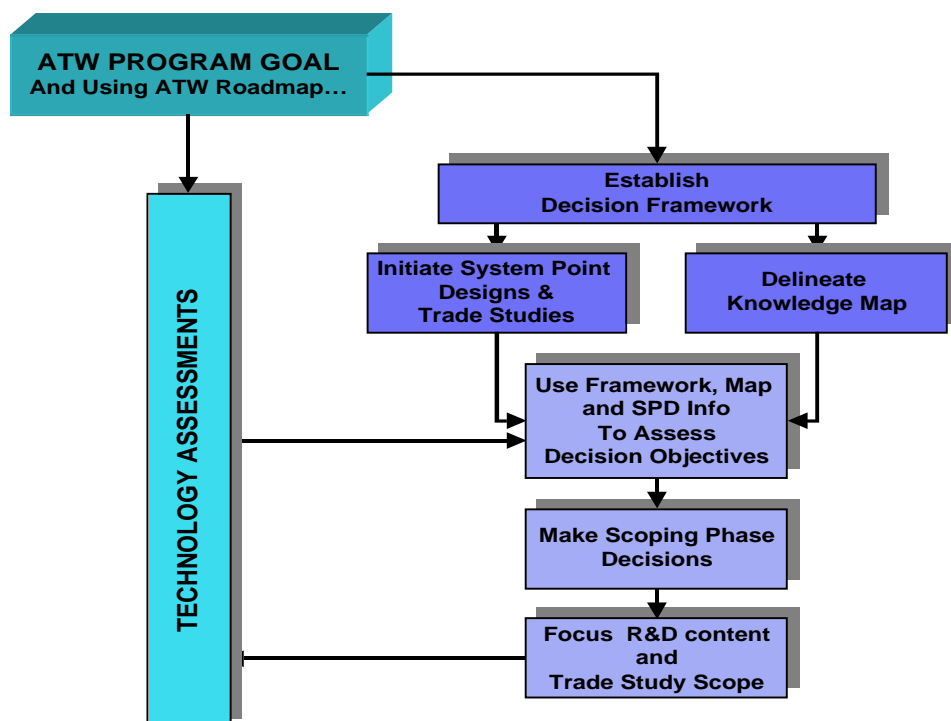
Figure 1-1.   ATW Decision Framework Schema.

The SPDs provide a systematic structure to compare a variety of technical alternatives to programmatic objectives, and are the mechanism for "establishing the playing field" amongst technology options. The purpose of the system point designs were threefold:

- To establish a common set of input, a "level" playing field and a common set of output for evaluating transmutation options

- To assess the analysis capabilities, code robustness and "comparability" of the many different analytical tools provided by participating institutions, and

- To provide a basis for generically comparing the characteristics and performance of various transmutation systems.

The purpose was *not* to design a set of optimum systems; rather the assessments were used to identify system attributes and flaws, and to provide input for R&D planning.

The System Point Designs in conjunction with the knowledge map will help identify what is fundamentally known, and what is not known. Likewise, the review of the SPDs through the decision framework should highlight how well the technologies comply with the program objectives.

Several assumptions were used as a common basis for the assessments:

- The feed stream inventory was based on data from ORNL-TM-110181 because of the variability anticipated in the spent nuclear fuel feed.

- The k_{eff} swing was assumed at 0.98 to 0.90 to minimize the impact on the accelerator design, and

- Fuel shuffling schemes were predicated on data limits for material irradiation damage at fluences of 4×10^{23} n/cm^2.

Within the decision framework context, a set of scooping assumptions, and using the information provided by "A Roadmap for Developing Accelerator Transmutation of Waste (ATW) Technology," [2] and the Roadmap's companion documents [3, 4, 5, 6, 7, 8], the system point design assessments were initiated in early spring of 2000.

1.2 Compendium Content

The compendium provides a section on the following System Point Design assessments:
- Sodium-cooled (Na) transmutation
- Molten salt (MS) transmutation
- Lead bismuth eutectic (LBE) transmutation
- Gas-cooled transmutation
- Fusion transmutation
- Electron, ICF, and Induction-LINAC transmutation

Each section has been written to provide approximately the same content:
- Scope and Objectives, including Degrees of Freedom, constraints and problem definition
- Parametric studies including neutronics, fuel cycle, fuels and materials, thermal hydraulics and safety considerations
- SPD analyses and results
- Interface Issues (separations/fuels, accelerator/target, target/blanket)
- Conclusions

1.3 Fundamental Conclusions

Three fundamental conclusions have been derived from the SPD assessments:

- Basic transmutation schemes (Na, LBE, gas and MS) can indeed transmute sufficiently, but with certain limitations

- The analytical tools used for liquid-metal systems demonstrate comparable results for comparable cases

- The analytical tools to assess gas-cooled systems provide different results

Technical assessment of system performance and characteristics, and detail on these conclusions is set forth in the actual evaluations.

References

1. Ludwig, S. B. and J.P. Renier, "Standard- and extended-burnup PWR and BWR reactor models for the ORIGEN2 computer code", ORNL-TM-11018, December 1989.

2 . "A Roadmap for Developing Accelerator Transmutation of Waste (ATW) Technology—A Report to Congress", DOE-RW-0519, October 1999.

3 . "A Roadmap for Developing ATW Technology: System Scenarios and Integration," ANL 99/16, September 1999.

4 . "A Roadmap for Developing ATW Technology: Accelerator Technology," LA-UR-99-3225, September, 1999.

5 . "A Roadmap for Developing ATW Technology: Target-Blanket Technology," LA-UR-99-3022, September, 1999.

6 . "A Roadmap for Developing ATW Technology: Separations and Waste Forms Technology," ANL-99/15, September, 1999.

7. "A Roadmap for Developing ATW Technology: Performance Assessment of a Geological Repository Containing High Level Waste and Waste from Accelerator Transmutation of Waste (ATW)," PNNL-13020, September, 1999.

8 . "A Roadmap for Developing ATW Technology: Estimated Cost of an ATW System," PNNL-13018, October 1999.

2 Sodium-Cooled Blanket

2.1 Executive Summary

This chapter describes the development of a system point design for an ATW system employing a sodium-cooled transmutation blanket. This development has so far focused primarily on the blanket component of the overall system, because the choice of blanket technologies is among the most important technical decisions faced in the ATW program. The blanket is assumed to be fueled with a non-uranium metallic dispersion fuel; pyrochemical techniques are used for recycle of residual transuranic actinides (TRU) in this fuel after irradiation. The primary objective has been to define the characteristics of a system that effectively consumes transuranics separated from LWR spent fuel and minimizes TRU losses to the waste streams. The key blanket design goal is to maximize the discharge burnup; this implies the fewest number of recycle/refabrication campaigns to destroy a given amount of material.

Parametric studies were performed to optimize the sizing of the sodium-cooled transmuter blanket, to mitigate power peaking problems near the source region, and to assess startup core performance. In these studies, a wide range of potential transmuter configurations and fuel cycles scenarios were investigated for an assumed transmuter fission-power level of 840 MW, the same power level previously adopted for the PRISM Advanced Liquid Metal Reactor (ALMR).

Compared to ATW systems employing lead-bismuth eutectic (LBE) coolant, sodium-cooled blankets require a higher TRU inventory because of increased neutron leakage. However, much higher flow rates can be used with sodium coolant that allows a significant reduction in the coolant volume fraction. For this study, the ALMR tight-lattice fuel assembly design, with a pitch-to-diameter (P/D) ratio of ~1.2, was employed. The associated increase in fuel-volume fraction allows considerable compaction of the blanket (~30% compared to the LBE-cooled design) with associated economic benefits. The extent of this size reduction is constrained by the peak linear power limit, which was estimated to be 400 W/cm for the non-uranium metallic dispersion fuel in a sodium-cooled environment.

Design options to enhance the flux and power peaking performance of the sodium-cooled ATW blanket were also investigated. Because the reactivity loss over an irradiation cycle reduces the fission power generated per source neutron, maintaining the power level (and TRU destruction rate) requires either addition of reactivity or increase of source strength. In this study, the decline in source multiplication was assumed to be compensated by increasing the source strength. The increased source strength at end-of-cycle (EOC) can lead to severe flux and power peaks in the blanket near the source. A variety of design options to mitigate this peaking behavior were identified. Refined allocations of the assemblies to high- and low- enrichment zones were developed to reduce the power peaking factors. Parametric studies indicate that an enrichment split of 1.3 gives the most favorable performance. In addition, the cycle length was shortened to 135 days (half a year at 75% capacity factor) to reduce the decline in multiplication factor. Even with improved

power peaking behavior, high flux levels in the inner blanket required a somewhat shorter fuel lifetime (compared to the outer blanket) for the same discharge fast fluence level.

The performance of the sodium-cooled ATW blanket SPD operating on a startup cycle was contrasted to the equilibrium cycle results. The main performance difference is that the transuranic inventory is ~20% lower for the startup cycle because of the higher fissile content of the LWR discharge feed stream (compared to the recycled ATW blanket with LWR TRU makeup). The evolution of the transuranic isotopics suggests a fairly rapid and smooth transition from the startup cycle performance to the equilibrium cycle performance.

A sodium-cooled blanket point design was developed based on the results of the foregoing parametric studies. This system employs TRU-10Zr/Zr dispersion fuel and the ALMR "tight lattice" fuel assembly design with pin P/D ratio of 1.2; its power density of 241 W/cc is quite similar to the ALMR fast reactor. The point design layout consists of 19 hexagonal lattice positions containing the LBE target/buffer and 132 fuel assemblies, and is surrounded by two hexagonal rows of steel reflector assemblies and one row of B_4C shield assemblies. Flattening of the blanket power distribution was accomplished by dividing the blanket into two "enrichment" zones and optimizing the relative TRU loading in each zone. An 8-batch fuel management scheme with semiannual refueling, staggered reloading of neighboring assemblies and no fuel shuffling is employed for the outer zone; the fuel residence time in the inner blanket zone is reduced to 7 cycles to limit the peak fast fluence. The fuel mass loading in each blanket zone was determined according to the specified 1.3 enrichment split such that the targeted multiplication factor (k_{eff} = 0.97 at beginning of cycle—BOC) is obtained.

The equilibrium-cycle neutronics performance of the proposed design was analyzed using the REBUS-3 code. The (inhomogeneous) flux calculations were performed using a spallation neutron source distribution generated for a 1-GeV proton beam and a prototypic LBE target. A medium-burnup (33,000 MWd/MT) PWR (pressurized water reactor) assembly with 25-year cooling time was used to specify a composition of the LWR-discharge feed stream.

Results of the performance evaluations indicate that an average discharge burnup of 275 MWd/kg (29.5 atom%) is achieved with the 3.5 to 4 year fuel residence time. The annual TRU loading is 801 kg/year, composed of 565 kg/year of recycled TRU and 236 kg/year of LWR-discharge TRU; the blanket TRU inventory at BOC is 2620 kg. The highest fuel particle fraction in the charged fuel (i.e., the outermost zone enrichment) is ~26 volume percent, which is well within the limit of the metallic dispersion fuel. Reactivity loss over the half-year cycle is 4.9%Δk. The peak fast fluence value at discharge is 4.06×10^{23} n/cm^2 for an assembly in the inner blanket zone. The power peaking factor is fairly low (~1.5 at both BOC and EOC); peak linear powers in the two blanket zones are very close to each other as desired and are just below the estimated limit of 400 W/cm.

If successfully developed, the proposed sodium-cooled system would consume LWR-discharge TRU at the maximum rate achievable per unit of fission energy produced (~0.9 g/MWthD). The overriding design objective of high-discharge burnup, to minimize the number of recycle stages and potential TRU losses to the waste stream, was shown to be

achievable in a configuration with high power density. This facilitates having a small system size and potentially favorable economics. Additionally, the burnup reactivity loss is relatively low, reducing the requirements for reactivity and/or source control. System design and operating characteristics that satisfy these goals while meeting key thermal-hydraulic and materials-related design constraints were preliminarily developed.

2.2 Introduction

This chapter describes the development of a point design for an ATW system employing a sodium-cooled transmutation blanket. This development has so far focused primarily on the blanket component of the overall system, because the choice of blanket technologies is among the most important technical decisions faced in the ATW program. Both the basic technology and the particular features of the blanket design strongly impact transmutation performance and requirements on other ATW sub-systems (spallation target, accelerator, chemical separations). The sodium-cooled concept developed here is one of several blanket technology options currently under consideration in the ATW program. It is planned to conduct screening evaluations leading to the selection of two or three of the candidate concepts for further development, and later to select a single preferred technology from among those retained in the initial screening process [9].

A discussion of the issues associated with the use of alternative coolants for ATW can be found in the reports of the ATW Roadmap working groups [10, 11]. An in-depth summary of the key neutronic, thermal hydraulic, material compatibility, coolant chemistry, and coolant activation characteristics of various liquid metal coolants is provided in Reference 12.

The organization of this chapter is as follows: Section 2.3 describes the scope and objectives of the SPD development and outlines the assumptions employed in the development. Parametric studies conducted to evaluate tradeoffs associated with adoption of various design parameters and operating strategies are presented in Section 2.4. Design parameters and performance characteristics for the blanket point design selected on the basis of these parametric studies are provided in Section 2.5. Section 2.6 summarizes conclusions of the SPD development studies and addresses requirements for:

(a) further development of the SPD, including subsystems other than the transmutation blanket, and

(b) assessment of key "interface" issues affecting the coupling of the various subsystems.

2.3 Scope and Objectives

The primary objective of the system development efforts at Argonne National Laboratory (ANL) has been to achieve efficient transmutation of the TRU separated from LWR spent fuel. It is generally recognized that a fast neutron energy spectrum is needed to accomplish the transmutation of minor actinides efficiently, because the fission-to-capture ratio for several key TRU nuclides is significantly greater in a fast spectrum [13]. The higher capture

probability per incident neutron in a thermal spectrum causes build-up of the higher actinide fraction in the proportion of the TRU loading not consumed by fission, which adversely impacts neutron balance at high burnup and complicates recycle if the burnup is incomplete. On the other hand, the higher TRU inventory of fast systems for a given power level implies a lower specific power and a correspondingly lower burnup rate. Moreover, the fuel irradiation time in a fast spectrum is limited by radiation damage to structural materials caused by the large flux of high-energy neutrons. Consequently, fuel burnup in a fast system is generally incomplete in one pass through the transmutation blanket, and *recycle of discharged fuel is required to achieve an acceptably low TRU content in the waste stream*. It is assumed in the SPD for the sodium-cooled system that fuel-recycle is performed using pyrochemical techniques described in the ATW Roadmap [14] which have since been referred to as "PYRO-B".

The major assumptions made in developing the sodium SPD are similar to those employed in the ATW Roadmap as a basis for estimating ATW system costs and analyzing deployment scenarios; they can be summarized as follows:

1. A high-power linear accelerator generates a beam of energetic (~1 GeV) protons for delivery to target/blanket "transmuter" system; the proton beam impinges on a spallation target and produces a source of neutrons that drives the subcritical blanket. The current system concept is to employ a single accelerator to drive four transmuters, and to deploy two accelerators (eight transmuters) at each ATW system site.

2. Beam delivery to the target is in the vertical direction. The target concept has not been developed at this time, and several options are under consideration for use in conjunction with the sodium-cooled blanket; these options include a liquid LBE target, a sodium-cooled tungsten target, and a gas-cooled tungsten target.

3. The blanket is fueled with solid, uranium-free fuel clad with a low-swelling stainless steel alloy similar to the HT-9 alloy developed in the U.S. Advanced Liquid Metal Reactor Program [15, 16]. The fission power level of each transmuter module is 840 MWth—consistent with the ALMR power level selected on the basis of favorable economics (through modular fabrication and installation) and excellent safety characteristics (through passive removal of decay heat using ambient air as an inexhaustible heat sink).

4. The transmutation blanket is coupled to systems for heat removal, steam generation and electricity production. The transmuter structures, the primary coolant and the components of the primary heat transport system are contained within a vessel in a pool-type arrangement. An intermediate heat-transport circuit transfers heat from the primary coolant in the intermediate heat exchanger (IHX) to the secondary water/steam coolant in the steam generator.

5. Chemical separations required to extract uranium and fission products from the LWR discharge fuel are performed with the UREX process [14], and the TRU-containing output stream from this process is treated with a subsequent pyrochemical process

("PYRO-A") [14] to produce metallic TRU feed for use in ATW fuel fabrication. Recovery of the TRU remaining in the ATW fuel after irradiation in the ATW blanket is performed using the "PYRO-B" [14] process. To minimize off-site shipments of nuclear materials, the (modular) facilities required to accomplish the separations and to incorporate process wastes into durable waste forms suitable for disposal are collocated with the accelerator and transmutation subsystems at the ATW plant site.

6. Key long-lived fission products (LLFP, i.e., I-129 and Tc-99) are separately recovered during the LWR spent fuel pre-treatment steps. The extent of transmutability of these species will dictate whether it is more appropriate to immobilize these species in suitable waste forms or to transmute them in the ATW blanket. Accordingly, initial system development efforts have focused on transmutation of TRU only. This approach provides a basis for future evaluations of overall system impacts of LLFP transmutation.

The central objective of the system development studies conducted to date has been to define the characteristics of a transmutation system that minimizes transuranic losses to the waste streams. It should be emphasized that neither the feasibility nor optimality of the system developed with this objective has been demonstrated; for example, alternative systems may exhibit superior economic or safety performance. Additional studies will be needed in the future to refine the point design and to optimize it with respect to a broader set of criteria.

As shown in Section 2.4, the objective of minimizing TRU losses to the waste stream is accomplished by maximizing the discharge burnup of ATW fuel (to minimize the number of recycle passes) and minimizing the fractional TRU loss per pass in recycle and refabrication. The achievable discharge burnup is believed to be constrained primarily by the fast-neutron irradiation damage to the cladding (fast fluence limit). The discharge burnup value currently targeted (~30 atom%) is high for conventional LMR fuels and remains to be demonstrated for the metallic dispersion fuel currently identified as the reference fuel form for the sodium-cooled (and the LBE-cooled) transmuter. However, this burnup appears to be a reasonable development goal for the dispersion fuel type, particularly uranium-free fuels employing a non-fissioning matrix (e.g., zirconium or molybdenum); at a fixed heavy atom (fractional) burnup, the fission product density is much lower with a non-fissioning matrix than with a uranium matrix. Thus to the extent achievable fuel burnup is governed by fission product accumulation, higher burnup fractions can be targeted for non-uranium fuels.

Analyses of the sodium SPD have so far focused primarily on the equilibrium fuel cycle, because system performance under equilibrium conditions is believed to be a good basis for design optimization. Performance of the system under non-equilibrium conditions has only been preliminarily explored, as discussed in Section 2.4. In the equilibrium cycle, the charged fuel contains the transuranics recovered via recycle from the discharged fuel, supplemented by LWR-discharge TRU to make up for the TRU deficit in the recycled component (i.e., for the ~30% TRU consumed by fission during irradiation in the ATW blanket). Determination of the equilibrium composition has so far neglected the very small proportion of TRU lost during recycle and refabrication.

2.4 Parametric Studies

Under the assumptions and constraints outlined in the previous section, parametric studies have been conducted to evaluate tradeoffs associated with adoption of various blanket design parameters and operating strategies. Full advantage is taken of the parametric studies performed as part of the LBE-cooled ATW transmuter study [17]. In particular, the zirconium matrix metallic-dispersion fuel form developed for the LBE system is employed. In addition, the performance objectives (Section 2.4.1) reflect the general trends observed in the LBE-cooled ATW trade-off studies (e.g., a preference for low inventory transmuter options). The primary topics addressed in the sodium-cooled transmuter design studies are:

- Sizing of the transmuter blanket
- Power/flux peaking caused by the source-driven configuration
- Relative performance of startup and equilibrium fuel cycles

In this section, the approaches and results of these parametric studies are presented. The rationales for selected performance objectives are discussed in Section 2.4.1. The imposed design constraints are presented in Section 2.4.2, and computational methods applied in this analysis are described in Section 2.4.3. The results of the parametric studies are summarized in Section 2.4.4 with subsections addressing the three major issues identified above. These studies evaluate a wide variety of alternative blanket configurations and fuel cycle scenarios. The SPD described in Section 2.5 incorporates design features developed on the basis of the blanket sizing and power peaking studies described in Sections 2.4.4.1 and 2.4.4.2, respectively.

2.4.1 Performance Objectives

The main purpose of the ATW system is to facilitate spent fuel disposal by removing the TRU and possibly LLFP's from the spent fuel and transmuting these constituents in the ATW blanket. Accordingly, the overriding performance objective for the ATW system is to minimize the fraction of the initial TRU inventory that is not transmuted and lost to the waste stream. Because there is a fraction of the TRU inventory lost every time the material is processed, developing high-efficiency processing technology and limiting the number of processing operations required are design targets. From the viewpoint of transmuter design, the key design goal is to maximize the discharge burnup; this implies minimizing the number of recycle/refabrication campaigns to destroy a given amount of material.

The primary design goal to eliminate TRU from the final waste stream is also the reason for utilizing uranium-free fuel forms. This prevents the generation of new TRU by in-reactor transmutation of uranium into plutonium. Because all current reactors operate on uranium-based fuel forms, a fuel development program will be required for this waste transmutation mission; accommodation of high burnup is a primary development goal for this new fuel form. For this application, a dispersion fuel where TRU-10Zr fuel particles are dispersed in a zirconium metal matrix has been proposed [14]. Extensive experience with U-10Zr and U/Pu-10Zr fuels in the EBR-II fuel development program demonstrated the compatibility of similar fuel forms with sodium coolant; sodium was also utilized as a bond material within the pin. The dispersion fuel will be designed so that the fission products are contained within

the fuel particles, which are contained within the matrix. Thus, this fuel form is expected to have superior irradiation performance (much less swelling than metal plutonium alloys) and there is no conceptual limit to the burnup.

Given the design goal of high discharge burnup, the required fuel irradiation time will be roughly proportional to the TRU inventory of the transmuter blanket. Low inventory options offer several advantages from a global fuel cycle perspective. Although the total amount of material destroyed is dictated solely by the power level, with low inventory of TRU, a higher rate of burnup accumulation (MWd/kg per year or atom%/year) is achieved. In addition, low inventory transmuters require less of the TRU inventory targeted for transmutation to run a single system; thus, additional transmuters can be started from the same initial inventory, increasing the overall destruction rate. Low inventory systems also have a smaller final discharge (un-transmuted) inventory at the end of their operation campaign.

Conversely, design options with high inventory offer several improvements to the performance of the transmuter blanket. One of the major problems associated with utilization of uranium-free fuel is the complete loss of internal conversion of the uranium matrix, which creates fissile material (Pu-239) with fuel burnup. This leads to magnified reactivity losses with fuel burnup compared to conventional systems. For reactor systems, which must maintain criticality, this is a crucial design consideration. For the "pure burner" design developed for the ALMR as part of the U.S. Plutonium Disposition Study [13], reactivity loss rates were reduced by maximizing the TRU inventory; this was done by increasing the core volume and adding a fixed poison. Since the TRU loss rate is determined solely by the system power level, this effectively increases the ratio of EOC TRU mass to BOC TRU mass for a given cycle length, leading to smaller reactivity loss rates. In general, high inventory designs will be larger than low inventory options. The associated reduction of power density may be desirable to reduce the heat loads for the unproven non-uranium fuel forms. On the other hand, there will be economic penalties associated with any blanket size increase.

The relative performance of high and low inventory ATW design options was evaluated in Reference 17 for the LBE-cooled ATW system. Results indicate that reactivity losses can be kept reasonably small through the use of sufficiently short cycle lengths (e.g., 3 to 6 months). The resulting reactivity losses can be compensated by a combination of increased source strength or potential reactivity insertion (see Section 2.4.2). Therefore, low TRU inventory has been adopted as a preferred option for the sodium-cooled transmuter studies. As discussed above, this approach will result in compact (low cost) design options with superior fuel cycle performance.

2.4.2 Design Constraints

For conventional fast reactor systems, fuel pin integrity is insured by imposing discharge burnup limits for the fuel matrix and peak fast fluence limits for the cladding material. Typically, the fuel lifetime is constrained to 4-5 years at which point the irradiated fuel is near both limits. For the zirconium matrix dispersion fuel employed here, there is no conceptual burnup limit. Therefore, the fuel lifetime may be limited only by damage considerations for

the structural materials. For this analysis, a peak fast fluence limit of 4.0×10^{23} n/cm^2 is assumed; this value is based on data for low-swelling ferritic alloy (HT-9) developed in the ALMR program [15, 16].

The TRU fraction in the fuel is determined such that the effective multiplication factor at BOC is 0.97. The reactivity loss and declining source multiplication during the operating cycle are assumed in the current design analyses to be compensated by increased source strength. To prevent a need for accelerator capacity to increase by more than a factor of three, the EOC effective multiplication factor must be at least 0.91; this limit constrains the cycle length depending on the reactivity loss rate.

The maximum *volume* fraction of TRU-Zr fuel particles in the proposed dispersion fuel is 50%. However, the dispersion fuel will be easier to fabricate and likely have improved irradiation performance at much lower fuel volume fractions. Thus, design options which result in reduced fuel volume fraction within the dispersion matrix are preferred.

Finally, the size and power density of the transmuter blanket is constrained by fuel heat load and heat transfer considerations. In particular, the peak linear power is constrained by the need to limit peak fuel centerline temperatures to prevent fuel melting. Estimates of the peak linear power limit for the proposed fuel form and for ternary (U-Pu-10Zr) metallic alloy fuel, (the reference fuel form in the PRISM ALMR [15]) are derived in Table 2-1. The TRU-10Zr composition of the fuel particles in the ATW dispersion fuel has a significantly lower (~150°C) solidus temperature compared to the ternary metal fuel alloy. However, the thermal conductivity of the dispersion (composite) fuel is significantly improved because the zirconium matrix is highly conductive and its thermal properties are not expected to degrade with irradiation as observed for fuel alloys. The net result is an estimated increase in the allowable peak linear power from 375 W/cm to 450 W/cm. Note that the peak linear power limit is lower with LBE coolant because of a much larger temperature rise in the coolant itself. This difference is attributed primarily to higher coolant flow rate and improved thermal conductivity in the sodium. Given the large uncertainties associated with thermal properties of the non-uranium dispersion fuel, it was considered prudent to impose a conservative design constraint. Thus, a peak linear power limit of 400 W/cm was assumed in these parametric studies.

Table 2-1. Estimation of Peak Linear Power for ATW Dispersion Fuel (U-10Zr/Zr) and ALMR Metallic Alloy Fuel (U-27Pu-10Zr)

Parameter	ALMR Metal Fuel Sodium Coolant	ATW Dispersion Fuel Sodium Coolant	ATW Dispersion Fuel LBE Coolant
Coolant Film Heat Transfer Coefficient (W/m^{2}K)	1.42E5	1.42E5	3.77E4
Clad Thermal Conductivity (W/mK)	26.8	26.8	26.8
Fuel Solidus Temperature (^{o}C)	990	840	840
Fuel Thermal Conductivity (W/mK)	15.3	13.8	13.8
Matrix Thermal Conductivity (W/mK)	-	22.2	22.2
Fuel Volume Fraction (%)	100	~40	~30
Irradiation Decrease in Fuel Conductivity (%)	50	50	50
Effective Fuel Matrix Thermal Conductivity (W/mK)	7.65	16.1	17.6
Peak Linear Power Estimate (W/cm)	**374**	**454**	**332**

2.4.3 Computational Methods and Modeling Assumptions

Analyses of the sodium-cooled SPD have so far focused primarily on the equilibrium fuel cycle, because system performance under equilibrium conditions is believed to be a good basis for design optimization (startup cycle performance is compared to the equilibrium results in Section 2.4.4.3). Equilibrium cycle performance characteristics were calculated using the REBUS-3 fuel-cycle analysis code [18, 19]. The region-dependent multigroup cross sections used in the neutronic analyses were originally generated for the ALMR pure-burner design as described in Reference 13; they are based on ENDF/B-V.2 basic data processed using the MC^2-2 [20] and SDX [21] codes for a 21-group energy structure.

In the equilibrium fuel-cycle model, the charged fuel contains the transuranics recovered via recycle from the discharged ATW fuel, supplemented by LWR-discharge TRU to make up for the TRU consumed by fission. Determination of the equilibrium composition neglected the very small proportion of TRU lost during recycle and refabrication, and assumed 5% of rare-earth fission products carried over by the recycled ATW TRU. The TRU mass loading in

the fuel which meets the targeted subcriticality level at the beginning-of-equilibrium-cycle (BOEC) was determined using the REBUS-3 enrichment search techniques. REBUS-3 also computes both batch-dependent and batch-averaged compositions at BOEC and EOEC for each specified depletion region. In this study, five (equal length) axial depletion zones were consistently used; in the planar dimension, depletion zones consisted of individual fuel assemblies or groups of neighboring assemblies with similar reaction rates. Irradiation swelling of the fuel was modeled in the depletion calculations as a uniform 5% axial expansion of the fresh fuel, based on IFR experiments for U-Pu-Zr ternary metal fuel, even though the proposed dispersion fuel is expected to exhibit less irradiation swelling.

Preliminary sensitivity studies of the effect of various flux computational options available in REBUS-3 were performed as part of the LBE-cooled ATW blanket design studies [17]; solutions obtained with the nodal diffusion option in hexagonal-Z geometry [22], the finite difference options in triangular-Z and R-Z geometries [23], and the VARIANT P_1 approximation in hexagonal-Z geometry [24] were compared. Both the inhomogeneous source problem and the corresponding homogeneous eigenvalue problem (i.e., a system without the spallation source made artificially critical by use of an eigenvalue to scale neutron production) were considered.

The flux solution sensitivity studies demonstrated that the global performance parameters are very similar for the different flux calculation methods. In addition, the integral parameters estimated with the eigenvalue calculations were found to agree well with the results of the corresponding inhomogeneous source calculations; peak flux and power were not as accurately predicted by the eigenvalue calculations. Thus, for computational convenience, homogeneous (eigenvalue) neutronic calculations performed using the hexagonal-Z nodal diffusion option of DIF3D were employed as a basis for optimizing the global design parameters (e.g., system size) of the sodium-cooled ATW blanket as described in Section 2.4.4.1.

The increase in source strength required to compensate the lower EOEC neutron multiplication leads to large increases in flux in the vicinity of the source region, which creates flux and power peaking problems. In Section 2.4.4.2, design options to mitigate the power peaking inherent to the source-driven configuration are investigated. For this analysis, inhomogeneous source problems were solved using a "generic" spallation neutron source distribution generated for a 1-GeV proton beam and a prototypic LBE target [25]. Even though the spallation neutron source distributions need to be generated for specific transmuter (target/blanket) configurations, inhomogeneous source analyses can be performed with sufficient accuracy using generic source distributions appropriate to the accelerator beam proton energy and the spallation target material and geometry. For these analyses, the flux calculation method was switched to the triangular-Z finite difference option of DIF3D to estimate the peak values more accurately. These same techniques were used for the final SPD evaluation presented in Section 2.5.

2.4.4 Discussion of Parametric Study Results

In this section, results of the sodium-cooled ATW transmuter design studies are summarized. These studies address sizing of the transmuter blanket (Section 2.4.4.1),

mitigation of power peaking problems near the source region (Section 2.4.4.2), and startup core performance (Section 2.4.4.3).

2.4.4.1 Blanket Sizing

A preliminary 840 MWth LBE-cooled ATW transmuter [26] was used as the starting point for developing the sodium-cooled system. This LBE configuration employs the seven central assembly locations for the LBE target and buffer as shown in Figure 2-1. The target/buffer will need to be a separated zone in the sodium-cooled system and its precise design is not specified at this point in time. Although alternative solid target concepts are under consideration for the sodium-cooled system, the LBE target/buffer option is attractive because of its high neutron production rates. Thus, for consistency with the LBE-cooled system trade-off studies, the LBE spallation target and buffer zone shown in Figure 2-1 were retained for the sodium-cooled transmuter design studies.

Target (1)   Buffer (6)

Low Enr. Fuel (102)   High Enr. Fuel (90)

Reflector (114)   Shield (66)
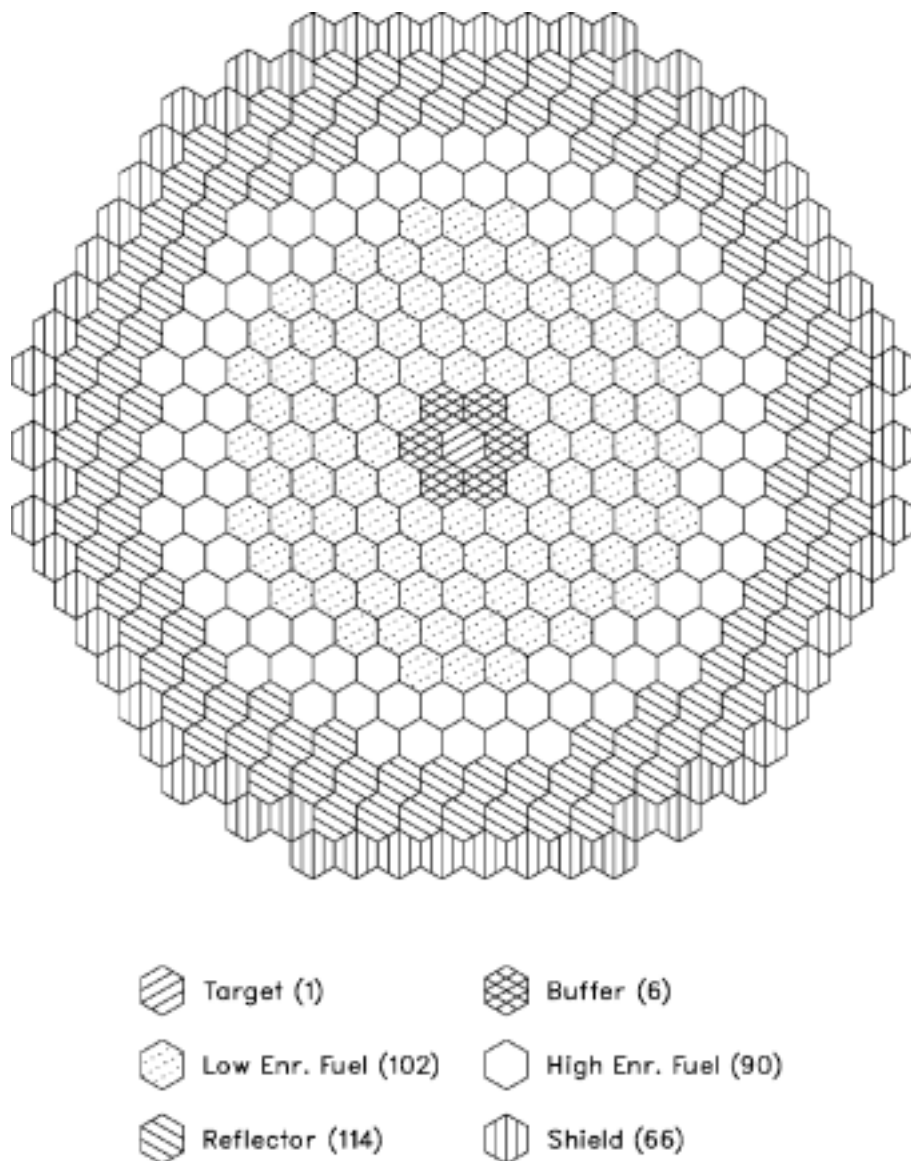
Figure 2-1.   192 Fuel Assembly LBE-cooled ATW Configuration

The preliminary LBE-cooled blanket is composed of 192 fuel assemblies in two "enrichment" zones. The enrichment is varied by using a higher-volume fraction of the TRU-10Zr fuel particles within the zirconium matrix in the outer region. An enrichment split of 1.2 was assumed. The assembly design parameters for this LBE-cooled point design are shown in Table 2-2.

Table 2-2.   Assembly Design Parameters for the LBE-Cooled Blanket and the ALMR

		LBE-Cooled ATW Design	Sodium-Cooled ALMR Design
Pin Diameter (cm)		0.635	0.744
Cladding Thickness (cm)		0.056	0.056
Pitch-to-Diameter Ratio		1.727	1.197
Number of Fuel Pins per Assembly		210	271
Fuel Smear Density (%)		75	75
Volume Fractions (as fabricated)	Fuel	0.200	0.377
	Structure	0.105	0.257
	Coolant	0.695	0.366
Hexagonal Assembly Pitch (cm)		16.14	16.14

The lattice design is quite loose with a P/D ratio of 1.73 resulting in a coolant volume fraction of nearly 70%. The high coolant volume fraction is necessary to achieve the low coolant velocity required for the heavy liquid metal coolant. In addition, seven of the 217 pin locations contain dummy structural pins for holding down the assembly; this hold-down mechanism is required with the heavy liquid metal coolant but not with sodium coolant. The net result is a low fuel volume fraction of only 20% as compared to a smeared fuel volume fraction of 38% in the ALMR design [15].

First, the performance effects were evaluated for a direct replacement simple exchange of LBE coolant with sodium, using the loose (LBE) lattice design shown in Table 2-1. In addition, the fuel cycle parameters of the LBE system described in Reference 26 were retained (i.e., a fuel residence time of six 145-day cycles was assumed). This evaluation illustrates the impact of sodium coolant (relative to LBE) on the reactor performance. Performance results are compared for the two coolants in Table 2-3. From a reactor physics viewpoint, the main difference between the sodium and LBE coolant is increased scattering (without moderation) in the LBE. Thus, the LBE reduces neutron escape from the interior regions of the blanket and provides superior reflection for neutrons that leak out of the active zone. Thus, a much higher (~30%) TRU inventory is required to achieve the BOEC multiplication target of 0.97 when sodium coolant is used. For a fixed fuel lifetime, a corresponding decrease in the average discharge burnup (by 20%) is observed. As identified in Section 2.4.2, the high inventory has a favorable impact of reducing the reactivity loss rate. In addition, the power-peaking factors are lower in the sodium system because the LBE coolant retains more neutrons in the peak power regions.

Table 2-3. Performance Parameters of LBE Configuration with LBE and Sodium Coolant

LBE Configuration (Figure 2-1)		LBE-Cooled	Sodium Substitution	Extended Fuel Lifetime
Number of Fuel Batches		6	6	8
Cycle Irradiation Time (days)		145	145	175
Fuel Particle Fraction (volume% in matrix)	Inner zone	27.5	34.2	38.2
	Outer zone	33.5	41.8	**46.8**
Multiplication Factor	BOEC	0.970	0.970	0.969
	EOEC	0.912	0.928	0.922
Burnup Reactivity Loss (% Δk)		5.80	**4.17**	4.69
Power Peaking Factor	BOEC	1.452	1.385	1.378
	EOEC	1.453	1.381	1.380
Peak Linear Power (W/cm)		317	287	311
Discharge Burnup (MWd/KgHM)	Average	272	**218**	**314**
	Peak	373	294	422
Peak Fast Fluence (10^{23} n/cm^2)		3.96	2.55	4.03
Net TRU Consumption Rate (kg/year)		237	237	237
Equilibrium Loading (kg/year)	LWR TRU	237	237	237
	Recycled TRU	581	782	469
	Total TRU	819	1018	706
Heavy Metal Inventory (kg)	BOEC	2256	**2899**	3024
	EOEC	2130	2774	2873

The low fast fluence for the sodium case (2.5 vs. 4.0×10^{23} n/cm^2 for the LBE case) indicates that fuel lifetime can be extended. A scoping study was performed with the result that the fuel lifetime can be extended from 6x145 = 870 effective full-power days (efpd) to 1400 efpd before the fluence limit is exceeded for the sodium-cooled case. Results calculated for a fuel management scheme of eight 175-day irradiation intervals (1400 efpd fuel lifetime) are also given in Table 2-3. A corresponding increase in average burnup from 218 MWd/kg to 314 MWd/kg is observed. Because the *average* burnup of the blanket also

increases, a 4% increase in the TRU inventory is required to maintain the BOEC multiplication factor. An important result is that *the sodium-cooled design achieves a higher average discharge burnup than the LBE-cooled design* (314 MWd/kg vs. 272 MWd/kg*) at the same discharge fluence level*. This difference is attributed to the moderating effect of the sodium coolant. The neutron energy spectrum is harder when the LBE coolant is utilized, resulting in a higher fast fluence to total flux ratio. This difference is particularly pronounced for designs such as the LBE-cooled ATW configuration where the coolant volume fraction is quite high (70%, as shown in Table 2-2).

One drawback of the design where sodium is simply substituted in the LBE configuration is that the volume fraction of fuel particles (47% in the outer zone) is close to the 50% limit. Moreover, the resulting configuration does not take advantage of the possibility of designing a more compact system (reduced coolant volume fraction at higher flow rate) with sodium coolant. Thus, modifications to the assembly design, which increase the fuel volume fraction, were investigated; these changes effectively allocate additional space for zirconium matrix material. The most significant change was to switch from the loose lattice (P/D ~1.7) LBE design to a conventional tight-lattice (P/D ~1.2) design. The assembly design proposed for the sodium-cooled ALMR [15] was utilized; its design parameters are shown in Table 2-2. This change nearly doubles the fuel matrix volume as the smeared fuel volume fraction increases from 20% to 38%. This volume fraction increase also reflects the elimination of the dummy pins, which are not required in sodium coolant systems. Furthermore, the smear density of the fuel was increased from 75% to 85%; this change was recommended by the ATW fuel developers who do not anticipate a need for large gaps, which were required to accommodate fuel swelling in the ALMR ternary-metal fuel design [27]. These three changes together increase the fuel volume fraction by a factor of 2.15.

Performance results obtained with the increased fuel volume fraction are compared to the performance characteristics of the LBE and sodium-cooled loose lattice systems in Table 2-4. The fuel particle fraction in the fuel matrix is decreased to ~20%, roughly half the volume fraction required for the loose lattice assembly design. The exchange of coolant for fuel matrix material and additional structural material (see volume fractions in Table 2-2) leads to a 10% increase in the required TRU inventory as a result of increased leakage and parasitic capture in the structural materials. The higher inventory decreases the average discharge burnup to 286 MWd/kg. Note that the fast fluence does *not* decrease despite the reduction in discharge burnup. This is attributed to spectral hardening associated with the decreased coolant volume fraction in the tight-lattice design. The tight-lattice sodium design exhibits performance characteristics similar to the LBE-cooled configuration. However, the TRU inventory is 50% higher in the sodium-cooled configuration for the same net TRU consumption rate. The LBE design has a specific TRU consumption rate of 10.5% per year as compared to 7% per year for this sodium-cooled option. Therefore, design options to reduce the TRU inventory were explored next.

Table 2-4.   Effect of Lattice Design Variation on Performance Parameters

LBE Configuration (Figure 2-1)		LBE Loose Lattice	Sodium Loose Lattice	Sodium Tight Lattice
Number of Fuel Batches		6	8	8
Cycle Irradiation Time (days)		145	175	175
Fuel Particle Fraction (volume% in matrix)	Inner zone	27.5	38.2	**19.6**
	Outer zone	33.5	46.8	**23.7**
Multiplication Factor	BOEC	0.970	0.969	0.970
	EOEC	0.912	0.922	0.925
Burnup Reactivity Loss (%Δk)		5.80	4.69	4.51
Power Peaking Factor	BOEC	1.452	1.378	1.495
	EOEC	1.453	1.380	1.489
Peak Linear Power (W/cm)		317	311	**260**
Discharge Burnup (MWd/KgHM)	Average	272	314	286
	Peak	373	422	395
Peak Fast Fluence (10^{23} n/cm^2)		3.96	4.03	4.00
Net TRU Consumption Rate (kg/year)		237	237	236
Equilibrium Loading (kg/year)	LWR TRU	237	237	236
	Recycled TRU	581	469	537
	Total TRU	819	706	773
Heavy Metal Inventory (kg)	BOEC	2256	3024	3373
	EOEC	2130	2873	3222

The ALMR tight-lattice design introduces an additional row of pins within an assembly of the same physical dimensions. As shown in Table 2-4, this reduces the peak linear power from 311 W/cm to 260 W/cm despite larger power peaking factors in the tight-lattice case. There remains significant margin to the peak linear power limit of 400 W/cm derived in Section 2.4.2. Thus, more compact configurations using the tight-lattice design were evaluated. In addition to lowering the TRU inventory requirements, reductions in the core volume provide the economic benefit of reducing the system size and blanket hardware requirements (e.g., fewer fuel assemblies).
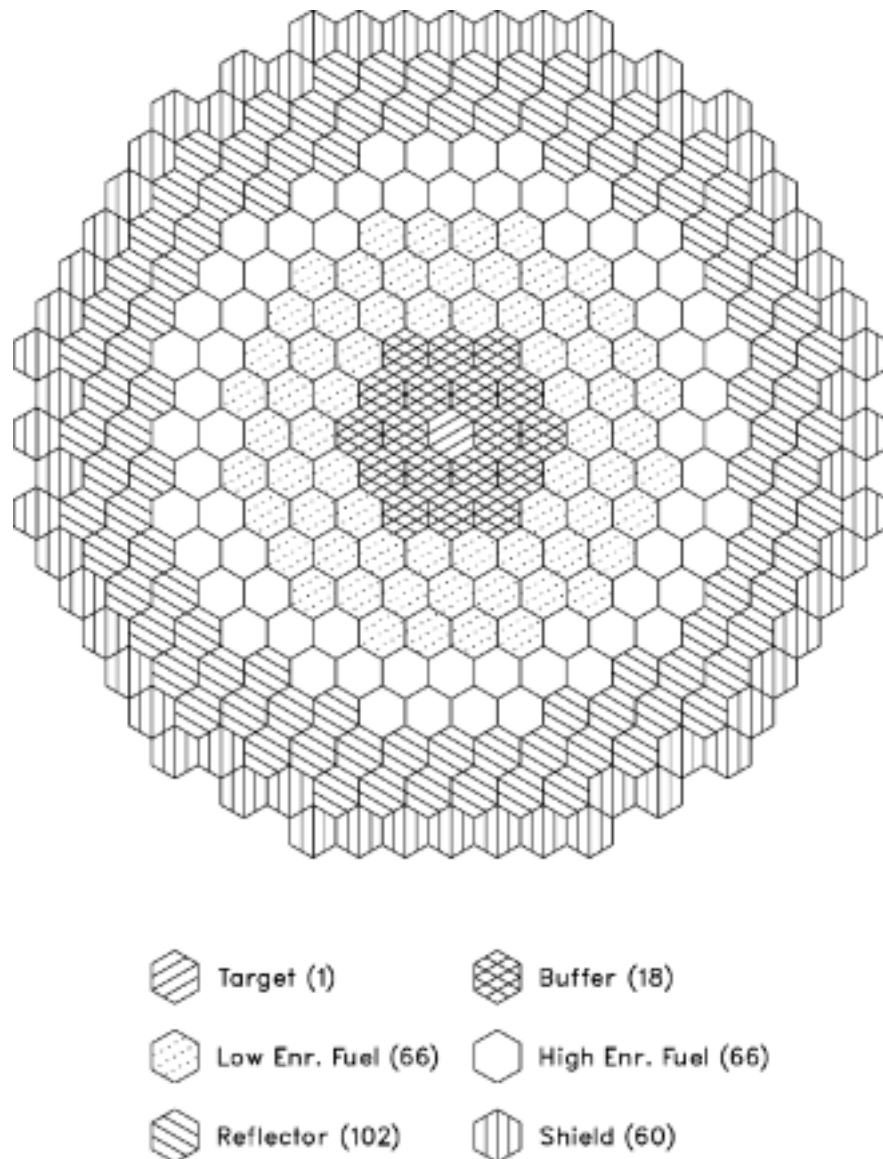
Figure 2-2.   Compact (132 Fuel Assembly) Sodium-Cooled ATW Configuration

For this evaluation, the core height and assembly design were retained, and fuel assemblies
were progressively eliminated from the periphery of the ATW configuration. Results are
given in Table 2-5 for cases where the number of fuel assemblies was reduced from 192
(Figure 2-1) to 132 and 120 assemblies. To avoid exceeding the assumed fluence limit, the
fuel residence time must be decreased roughly in proportion to the volume decrease. For
both revised configurations, a six-cycle management scheme was utilized with the 175-day
cycle length retained. The 120-assembly case has a peak linear power of 419 W/cm, which
exceeds the design limit, as well as a peak fast fluence of 4.45×10^{23} n/cm^2. Thus, the
132 assembly configuration shown in Figure 2-2 was identified as a favorable size for the
sodium-cooled blanket configuration. The number of fuel assemblies is reduced by ~30%

compared to the LBE-cooled blanket. The TRU inventory is reduced by 25% compared to 192 fuel assembly sodium-cooled configuration, increasing the specific consumption rate to 9.5% per year. The 372 W/cm peak linear power and 3.83×10^{23} n/cm^2 leave some margin to the design limits to accommodate increased flux and power peaking when the inhomogeneous source is modeled (the foregoing parametric analyses employed eigenvalue calculations of the neutron flux distribution). The impact of this peaking and refinements to the configuration to mitigate associated performance effects are analyzed in detail in Section 2.4.4.2.

Table 2-5. Performance Parameters of Compact Sodium-Cooled Configurations

		192 Fuel Assemblies	132 Fuel Assemblies	120 Fuel Assemblies
Number of Fuel Batches		8	6	6
Cycle Irradiation Time (days)		175	175	175
Fuel Particle Fraction (volume% in matrix)	Inner zone	19.6	21.6	21.4
	Outer zone	23.7	26.2	25.9
Multiplication Factor	BOEC	0.970	0.970	0.970
	EOEC	0.912	0.913	0.905
Burnup Reactivity Loss (%Δk)		4.51	5.68	6.48
Power Peaking Factor	BOEC	1.495	1.467	1.462
	EOEC	1.489	1.447	1.441
Peak Linear Power (W/cm)		260	372	**419**
Discharge Burnup (MWd/KgHM)	Average	286	281	310
	Peak	395	380	424
Peak Fast Fluence (10^{23} n/cm^2)		4.00	3.83	4.45
Net TRU Consumption Rate (kg/year)		236	236	236
Equilibrium Loading (kg/year)	LWR TRU	236	236	236
	Recycled TRU	537	551	478
	Total TRU	773	787	714
Heavy Metal Inventory (kg)	BOEC	3373	**2602**	2320
	EOEC	3222	2452	2169

2.4.4.2 *Power Peaking Trade-Off Studies*

In this section, design options to enhance the flux and power peaking performance of the sodium-cooled ATW blanket are evaluated. For this investigation, it is important to consider the impact of the inhomogeneous source on the flux and power distributions. Performance results for the eigenvalue neutronics computation (as utilized in Section 2.4.4.1) and the inhomogeneous source model (described in Section 2.4.3) are compared in Table 2-6. The fuel enrichment requirements and mass flows are very close; the TRU inventory is ~1%

greater for the source-driven computation. The reactivity loss over the cycle is also slightly higher for the source calculation. These results confirm that the eigenvalue calculation adequately predicts the global performance parameters for the modest subcriticality levels of interest.

Table 2-6. Comparison of Performance Predictions based on Eigenvalue and Inhomogeneous Source Calculations

132 Assembly Configuration (Figure 2-2)		Eigenvalue Calculation	Source Calculation
Fuel particle fraction (volume% in matrix)	Inner zone	21.6	21.7
	Outer zone	26.2	26.3
Net TRU consumption rate (kg/year)		236	236
Equilibrium loading (kg/year)	LWR TRU	236	236
	Recycled TRU	551	556
	Total TRU	787	792
Heavy metal inventory (kg)	BOEC	2602	2623
	EOEC	2452	2472
Multiplication Factor	BOEC	0.970	0.970
	EOEC	0.913	0.907
Burnup reactivity loss (% Δk)		5.68	6.31
Power peaking factor	BOEC	1.467	1.470
	EOEC	1.447	**1.708**
Peak linear power (W/cm)		372	**459**
Discharge burnup (MWd/KgHM)	Average	281	280
	Peak	380	459
Peak fast fluence (10^{23} n/cm^2)		3.83	**4.83**

However, significant differences are observed in the EOEC power peaking. Because the multiplication factor is lower at EOEC, the required neutron source strength increases by roughly a factor of three (if no other reactivity control techniques are used) to maintain the power output. This leads to a large flux peak in the interior fuel assemblies close to the spallation target. For the configuration shown in Figure 2-2, this phenomenon also leads to a power peak in the innermost row of assemblies, with a peak linear power of 459 W/cm. In addition, the fast fluence in this innermost row increases to 4.83×10^{23} n/cm^2.

Several design options can be conceived to mitigate this peaking behavior:

- The enrichment zoning of the blanket can be tailored to suppress the peak.

- The cycle length can be shortened to reduce the decline in multiplication factor between BOEC and EOEC.

- The blanket size can be increased to reduce the power density and specific power; the reduced cycle burnup also mitigates the multiplication factor decline.

- Fuel shuffling can be employed to preferentially place high burnup assemblies and limit exposure time in the inner locations of the blanket near the source.

- Fewer irradiation cycles can be employed for the innermost fuel assemblies. This does not reduce the flux or power peaking itself but does reduce the discharge fast fluence for the limiting (interior) fuel assemblies.

Increased blanket size is an undesirable option because the TRU inventory would be larger as shown in Section 2.4.4.1. Fuel shuffling could be utilized to accommodate the power peak, but in-residence fuel movement complicates fuel handling and is particularly undesirable for pool type liquid-metal-cooled reactors. The final option (decreased inner region residence) is also not favored because it penalizes the discharge burnup of the inner region fuel. Thus, the current parametric studies have focused on the first two options (enrichment zoning and reduction of cycle duration). Furthermore, a tentative limit of two enrichment zones was imposed for this study. Additional enrichment zones could be employed to better flatten the power shape, but utilization of numerous enrichments (different fuel particle volume fractions within the dispersion matrix) complicates both fuel fabrication and fuel handling.

First, alternate allocations of the assemblies to high and low enrichment zones were investigated for the 132 fuel assembly transmuter shown in Figure 2-2; the inner-to-outer blanket zone enrichment split of 1.2 was retained. The most favorable performance was observed when the low enrichment zone was sized at two rows thickness; this reduces the number of low enrichment assemblies from 66 to 42. The resulting blanket configuration is shown in Figure 2-3. Performance results for this configuration are summarized in Table 2-7. The TRU inventory is nearly the same for the two configurations. Thus, the increased number of high enrichment assemblies leads to a ~5% decrease in the fuel particle volume fraction for both zones. This leads to a lower power level in the low enrichment zone with a compensating power increase in the 24 assemblies reallocated from the inner zone in the original configuration to the outer zone. The power peaking factor decreases from 1.71 to 1.625 with an EOEC peak linear power of 435 W/cm in the inner row. However, the *flux* does not decrease in the interior region because the EOEC multiplication factor is not significantly affected; thus, the peak fast fluence is not significantly reduced.

Target (1)   Buffer (18)

Low Enr. Fuel (42) High Enr. Fuel (90)

Reflector (102)   Shield (60)
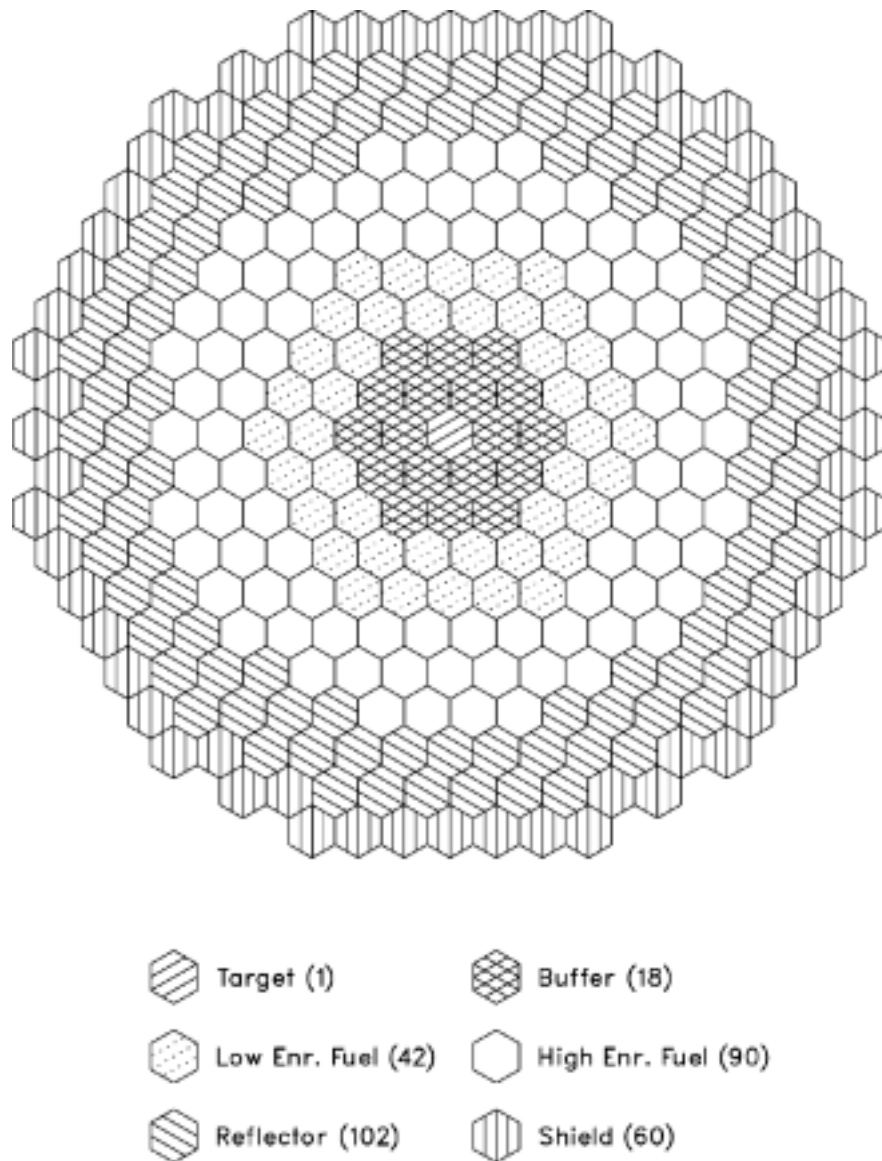
Figure 2-3.   Final (132 Fuel Assembly) Sodium-Cooled ATW Configuration

Table 2-7. Performance Effects of Alternate Enrichment Zoning and Reduced Cycle Length Options

Configuration		Figure 2-2	Figure 2-3	Figure 2-3
Number of Fuel Batches		6	6	8
Cycle Irradiation Time (days)		175	175	135
Fuel Particle Fraction (volume% in matrix)	Inner zone	21.7	**20.7**	21.0
	Outer zone	26.3	**25.0**	25.4
Heavy Metal Inventory (kg)	BOEC	2623	2593	2609
	EOEC	2472	2442	2492
Multiplication Factor	BOEC	0.970	0.971	0.970
	EOEC	0.907	0.906	**0.921**
Burnup Reactivity Loss (%Δk)		6.31	6.49	4.95
Power Peaking Factor	BOEC	1.470	1.516	1.509
	EOEC	**1.708**	**1.625**	**1.563**
Peak Linear Power (W/cm)		459	435	411
Discharge Burnup (MWd/KgHM)	Average	280	282	286
	Peak	459	465	460
Peak Fast Fluence (10^{23} n/cm^2)		4.83	4.81	4.72

To reduce flux peaking, the EOEC multiplication factor can be increased by using a fuel management strategy with a shorter cycle length. Thus, conversion to an eight-batch scheme with the cycle length reduced from 175 days to 135 days (roughly conserving fuel lifetime) was evaluated; results are given in Table 2-7 for the configuration shown in Figure 2-3. The EOEC multiplication factor increases from 0.906 to 0.921; this implies a ~20% decrease in source intensity. Since the source is centrally located, this further reduces the inner row peaking factor from 1.625 to 1.563 with a peak linear power of 411 W/cm (close to the 400 W/cm limit). The reduced source strength also decreases the flux in the interior assemblies; thus, a slight decrease in the peak fast fluence is observed in this case.

Finally, variations in enrichment split between the high and low enrichment zones were evaluated. Using the blanket configuration shown in Figure 2-3, the enrichment split was varied between 1.2 and 1.8; key performance results are summarized in Table 2-8. As the enrichment split is increased, the BOEC power peaking factor increases because the power peak is located in the outer core. Conversely, the EOEC power peak initially decreases

because it is located in the inner core region. At an enrichment split of roughly 1.3 the peak EOEC power in the inner and outer zones are roughly equal, and the lowest peaking factor of 1.515 is obtained. At higher enrichment splits, the EOEC power peak is located in the outer core, thus peaking becomes more severe with increasing outer zone enrichment. The results in Table 2-8 show that the peak fast fluence also decreases with increasing enrichment split. The fluence peak is located in the inner (low enrichment) zone, and shifting of the TRU loading (and fission rate) into the outer region reduces the inner zone flux. Based on these results, an enrichment split of 1.3 was specified for the sodium-cooled SPD. This is the only split that meets the peak linear power limit of 400 W/cm. Since the peak discharge fast fluence exceeds the assumed limit for all cases, a modified fuel cycle is required. In the final recommended point design described in Section 2.5, the fuel lifetime for the inner (low enrichment) fuel assemblies is reduced from eight to seven cycles. This results in discharge fast fluence within the design limit with only a slight penalty in the TRU burnup performance.

Table 2-8. Performance Results of Enrichment Split Parametric Study

Final Configuration (Figure 2-3)					
Enrichment Split		1.2	1.3	1.4	1.6
Fuel Particle Fraction (volume% in matrix)	Inner zone	21.2	20.2	19.2	17.4
	Outer zone	25.7	26.6	27.3	28.5
Heavy Metal Inventory (kg)	BOEC	2617	2638	2649	2670
	EOEC	2500	2521	2533	2553
Multiplication Factor	BOEC	0.970	0.971	0.970	0.970
	EOEC	0.921	0.921	0.920	0.919
Burnup Reactivity Loss (%Δk)		4.92	4.95	5.00	5.12
Power Peaking Factor	BOEC	1.478	1.508	1.535	1.573
	EOEC	1.566	1.515	1.546	1.596
Peak Linear Power (W/cm)		427	**399**	406	419
Discharge Burnup (MWd/KgHM)	Average	285	283	282	280
	Peak	460	447	439	420
Peak Fast Fluence (10^{23} n/cm^2)		4.71	**4.55**	4.44	4.22

2.4.4.3 Startup Cycle Performance

In this section, the performance of the sodium-cooled ATW design operating on a startup cycle (i.e., using LWR-discharge transuranics for the ATW feed stream) is contrasted to the base equilibrium (with recycle) case. For the startup case, an equilibrium REBUS-3 calculation is performed with processed LWR transuranics as the sole source of fuel material (no recycled feed). This computation roughly models the behavior of the ATW blanket in its initial core loadings and the condition of the fuel material for its first pass through the transmutation system. The comparison of startup and equilibrium cycle performance was performed for the blanket configuration developed in Section 2.4.4.2 (Figure 2-3) with an enrichment split of 1.3. The cycle length of 135 days (~1/2 year at a 75% capacity factor) was retained. An eight-batch fuel management strategy was employed for the high-enrichment fuel assemblies and a seven-batch strategy for the interior low enrichment fuel assemblies.

Performance results for the startup case are compared to the recycle case in Table 2-9. The TRU volume fraction and TRU inventory for the startup case are ~20% lower than the

equilibrium recycle; this is attributed to changes in the TRU isotopics as discussed below. The reduced inventory leads to a greater reactivity loss over the burnup cycle (lower EOEC multiplication factor), which in turn exacerbates the EOEC power peak. It appears a higher enrichment split and/or shorter cycle length are desirable to reduce the power peaking in the initial (low inventory) loadings. On the positive side, the reduced inventory yields a proportional increase in the average discharge burnup with associated fuel-cycle performance benefits.

Table 2-9. Performance Characteristics of Sodium-Cooled Blanket for Startup and Recycle Scenarios

		Recycle	Startup
Fuel Particle Fraction (volume% in matrix)	Inner zone	19.9	**16.0**
	Outer zone	26.2	**21.0**
Cycle Irradiation Time (days)		135	135
Multiplication Factor	BOEC	0.970	0.971
	EOEC	0.920	0.909
Burnup Reactivity Loss (%Δk)		4.94	6.13
Power Peaking Factor	BOEC	1.501	1.453
	EOEC	1.508	**1.559**
Peak Linear Power (W/cm)		397	449
Discharge Burnup (MWd/kg)	Average	275	**340**
	Peak	411	527
Peak Fast Fluence (10^{23} n/cm^2)		4.06	4.26
Net TRU Consumption Rate (kg/year)		236	236
Equilibrium Loading (kg/year)	LWR TRU	236	647
	Recycled TRU	565	0
	Total TRU	801	647
Heavy Metal Inventory (kg)	BOEC	2620	**2025**
	EOEC	2504	1909

The evolution of the TRU isotopics in the ATW fuel cycle is illustrated in Table 2-10 where the charge and discharge compositions for the startup and recycle cases are compared.

After the initial in-core residence the Pu-239 fraction has decreased from 53% to 34%. The proportion of Pu-239 and other fissile nuclides is reduced relative to the fertile transuranics, which tend to concentrate due to their lower cross sections. This phenomenon is the cause of the lower TRU enrichment requirements for the startup core where the fissile fraction is highest. The isotopics change significantly during the first irradiation campaign. The Pu-240 has already increased to nearly its equilibrium level (~33%). It takes longer for the higher capture products—Pu-242, Am-243, and Cm-244—to reach their equilibrium concentration. The Am-241 fraction actually decreases because the initial feed has a much longer post-irradiation cooling time, yielding additional Pu-241 decay, than the ATW discharge and recycle compositions. The evolution of isotopic fractions displayed in Table 2-10 suggests a fairly rapid and smooth transition from the startup cycle performance to the equilibrium recycle performance.

Table 2-10. Evolution of TRU Isotopics (weight%) in the ATW Fuel Cycle

Isotope	Startup Cycle		Equilibrium Recycle		
	Initial Feed (LWR TRU)[a]	Once-Through Discharge	Equilibrium Feed[b]	Equilibrium Discharge	0.8y Cooled Eq. Discharge
U-234	0.000	0.080	0.468	0.580	0.621
U-235	0.004	0.012	0.110	0.153	0.154
U-236	0.002	0.013	0.149	0.204	0.207
U-238	0.478	0.642	1.022	1.249	1.249
Np-237	5.023	3.541	2.896	1.990	1.997
Pu-238	1.272	5.773	5.039	6.226	6.552
Pu-239	**53.196**	**34.254**	28.729	18.499	18.502
Pu-240	21.533	31.800	31.492	35.437	35.548
Pu-241	3.782	5.683	5.523	6.780	6.525
Pu-242	4.686	**7.285**	**10.555**	13.005	13.007
Am-241	8.967	6.831	6.850	5.068	5.316
Am-242m	0.014	0.565	0.340	0.480	0.478
Am-243	0.926	**1.800**	**3.404**	4.440	4.440
Cm-242	0.000	0.771	0.030	0.519	0.147
Cm-243	0.002	0.066	0.039	0.057	0.056
Cm-244	0.104	**0.763**	**2.471**	3.682	3.570
Cm-245	0.009	0.111	0.711	1.005	1.005
Cm-246	0.001	0.009	0.443	0.628	0.628

[a] Processed transuranics from medium burnup PWR at 25 years cooling [28].
[b] Equilibrium feed is a mixture of recycled ATW transuranics and processed LWR transuranics as required for makeup.

2.5 System Point Design

Based on the results of parametric studies discussed in the previous section, a sodium-cooled blanket SPD was developed. The proposed blanket layout, shown in Figure 2-3, consists of 19 LBE target/buffer and 132 fuel assemblies. The blanket is surrounded by two

rows of steel reflector assemblies and one row of B_4C shield assemblies. The principal design parameters of the proposed design are summarized in Table 2-11.

The equilibrium-cycle neutronics performance of the proposed design was analyzed using the REBUS-3 code. Flux calculations were performed using the triangular-Z finite difference option of DIF3D. Inhomogeneous source problems were solved using a generic spallation neutron source distribution generated for a 1-GeV proton beam and a prototypic LBE target. A semiannual fuel management scheme (with assumed capacity factor of 75%) was employed with seven-cycle residence time for the inner (low-enrichment) fuel assemblies and eight-cycle residence time for the outer (high-enrichment) fuel assemblies; each fuel assembly remains in the same position for its entire core residence with no shuffling or rotation. The charged fuel contains the transuranics recovered via recycle from the discharged ATW fuel, supplemented by LWR-discharge transuranics as a makeup feed. The LWR-discharge feed stream is based on the composition of a medium-burnup (33,000 MWd/MT) PWR assembly with 25-year cooling [28]. The isotopic composition of this feed stream is compared with the equilibrium-cycle ATW discharge composition in Table 2-10.

Table 2-11. Design Parameters of Proposed ATW Sodium-Cooled Blanket Design

Proton Energy (GeV)			1.0
Target Material			LBE
Fuel Material			(TRU-10Zr)-Zr
Pin Diameter (cm)			0.744
Cladding Thickness (cm)			0.056
Pitch-to-Diameter Ratio			1.197
Number of Pins per Assembly			271
Fuel Smear Density (%)			85
Volume Fractions (as fabricated)	Fuel (smeared)		0.377
	Structure		0.257
	Coolant		0.366
Hexagonal Assembly Pitch (cm)			16.14
Number of Assemblies	LBE Target/Buffer		19
	Fuel	Inner Zone	42
		Outer Zone	90
		Total	132
	Reflector		102
	Shield		60
TRU Fraction Split Factor (outer zone/inner zone)			1.3
Active Fuel Height (cm)			107
Equivalent Fuel Region Diameter (cm)			208
Maximum Blanket Diameter (cm)			300
Number of Fuel Batches	Inner Zone		7
	Outer Zone		8
Cycle Irradiation Time (days)			135

The main performance parameters for the selected point design are summarized in Table 2-12. The average discharge burnup of 275 MWd/kg (29.5 atom%) is achieved with a 3.5 to 4 year fuel residence time. The burnup reactivity loss is ~5% with the adopted half-year cycle duration. The volume fraction of fuel particles in the matrix required to achieve the targeted subcriticality level at BOEC is 20% in the inner zone and 26% in the outer zone, which is significantly lower than the dispersion fuel limit. The peak fast fluence value of 4.06×10^{23} n/cm^2 in the inner zone assemblies is close to the assumed fluence limit. Slight changes to the enrichment zoning, cycle length, or fuel management (e.g., rotation of the innermost row) could be used to further reduce the inner zone discharge fluence, if desired.

Table 2-12. Performance Characteristics of Proposed ATW Sodium-Cooled Blanket Design

Fuel Particle Fraction (volume% in matrix)	Inner zone	19.9
	Outer zone	26.2
Multiplication Factor	BOEC	0.970
	EOEC	0.920
Burnup Reactivity Loss (%Δk)		4.94
Core-Average Power Density (kW/ℓ)		241
Power Peaking Factor	BOEC	1.501
	EOEC	1.508
Peak Linear Power (W/cm)	Inner zone	393 (at EOEC)
	Outer zone	397 (at BOEC)
Discharge Burnup (MWd/kg)	Average	275
	Peak	411
Peak Fast Fluence (10^{23} n/cm^2)	Inner Zone	4.06
	Outer Zone	3.97
Net TRU Consumption Rate (kg/year)		236
Equilibrium Loading (kg/year)	LWR TRU	236
	Recycled TRU	565
	Total TRU	801
Heavy Metal Inventory (kg)	BOEC	2620
	EOEC	2504

The blanket was sized to meet the peak linear power constraint of 400 W/cm as discussed in Section 2.4.4.1. The peak linear power in the outer zone is 397 W/cm, which occurs at BOEC. Because of the increased source strength at EOEC to compensate for the reduced multiplication factor, the peak linear power of 393 W/cm in the inner zone occurs at EOEC. These power peaks could be reduced further if more elaborate fuel management schemes were employed (i.e., more than two enrichment zones or fuel shuffling). It is important to note that the 400 W/cm peak linear power limit, derived in Section 2.4.2, was based on a conservative estimate that assumed a 40% fuel particle fraction. For the 26% fuel particle volume fraction employed in the SPD, the estimated limit would be closer to 500 W/cm. This

higher linear power limit would allow additional compaction of the sodium-cooled blanket design (~20% volume reduction), with associated economic and fuel cycle (reduced TRU inventory) benefits. Thus, an accurate determination of the linear power limit for the zirconium matrix metal dispersion fuel is a key consideration for future system design studies.

The batch-averaged power density and total neutron flux for each fuel assembly of the proposed point design (at BOEC and EOEC) are shown in Figure 2-4 through Figure 2-7 Figure 2-4 shows the power peak of 344 kW/ℓ in the middle of the blanket zone at BOEC. At EOEC (Figure 2-5) the power has decreased in the outer blanket region and the power peak in the innermost row (near the source) is similar to the middle blanket power peak in the high enrichment zone. This shows the efficacy of the enrichment zoning in smoothing the problematic EOEC power distribution. The flux results (Figure 2-6 and Figure 2-7) show that the blanket flux peak is always located in the innermost row, unlike the power peak, leading to higher discharge fluences levels in the inner zone for a fixed irradiation time. Note that the EOEC total flux level is higher to compensate for burnup of the TRU inventory while maintaining constant fission power. The decrease in TRU inventory from BOEC to EOEC is ~5% as shown in Table 2-12; the flux level in the middle blanket assemblies is observed to increase by a similar amount. However, much larger increases in flux level (20-25%) occur in the innermost blanket row; this is attributed to the increased source strength required at EOEC to maintain constant fission power (compensate for the reduced multiplication factor).
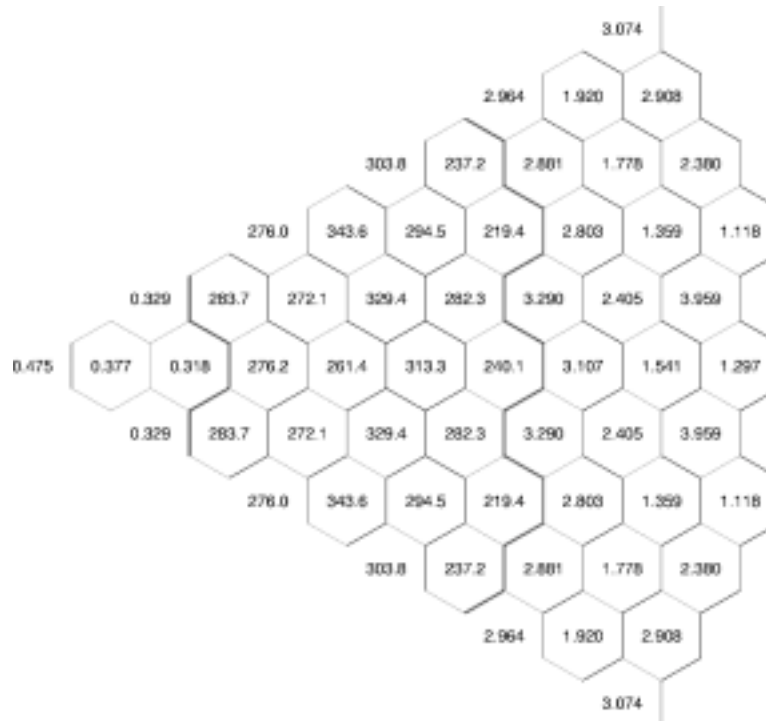
Figure 2-4.   Average Power Density (kW/ℓ) at Blanket Mid-Plane at BOEC

Figure 2-5.   Average Power Density (kW/ℓ) at Blanket Mid-Plane at EOEC

Figure 2-6.   Average Total Flux (10^{15} n/cm^2) at Blanket Mid-Plane at BOEC
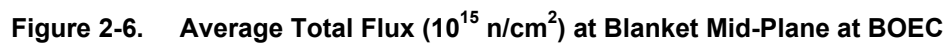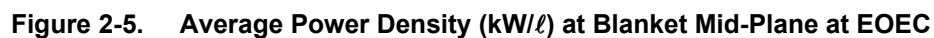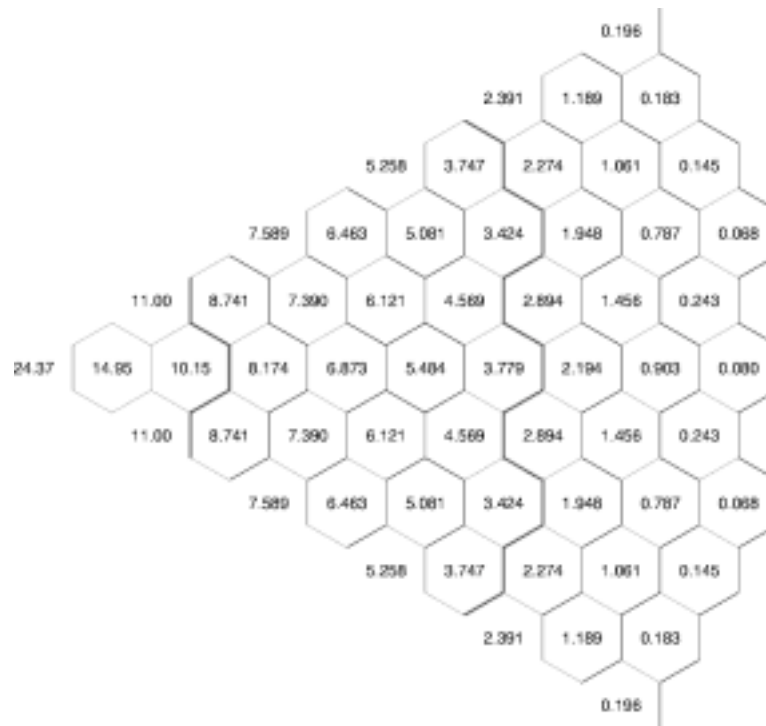
Figure 2-7.   Average Total Flux (10^{15} n/cm^2) at Blanket Mid-Plane at EOEC

2.6 Additional System Development Issues and Requirements

The parametric studies leading to the proposed SPD have defined the characteristics of a sodium-cooled transmutation blanket that enables efficient consumption of LWR discharge TRU. The key system objective of high ATW fuel discharge burnup (to minimize the number of successive recycle stages and associated TRU losses) was shown to be achievable in a configuration with comparatively high power density (enabling small system size and potentially favorable economics) and relatively low burnup reactivity loss (to reduce requirements for reactivity and/or source control). System design and operating characteristics that satisfy these goals while satisfying material-related design constraints and taking advantage of the *extensive experience base with design and operation of sodium-cooled, critical systems* were preliminarily developed. Perhaps more significantly, a systematic approach was devised for meeting these key objectives subject to the assumed constraints. This approach should greatly facilitate future efforts to optimize the system's performance (e.g., for updated values of the constraining variables or taking a broader set of performance objectives into consideration).

Two key assumptions made in developing the proposed point design are the power level of the transmutation system (840 MWth) and its minimum subcriticality level (k_{eff} = 0.97 at the start of cycle); both parameters strongly affect system characteristics and directly impact the accelerator beam power required per transmuter. The choice of transmuter (fission) power level is based largely on the recent design experience with the PRISM ALMR, which

indicates that favorable economics and safety performance can be achieved with the 840 MWth system size. The applicability of this experience to the accelerator driven system configuration should be examined in future studies. With respect to degree of subcriticality, the assumed level is believed to be a good compromise between the competing objectives of minimizing accelerator power (favors high k_{eff}) and precluding the potential for criticality as a result of operational or accidental reactivity insertions (favors low k_{eff}). However, explicit dynamic and safety analyses will be required to optimize the choice of subcriticality level.

Future evaluations of system dynamic behavior and safety characteristics must be performed in conjunction with (a) development of the heat transport system (nuclear steam supply system, NSSS), (b) design of the LBE spallation target and accelerator beam delivery system, and (c) development of the system control strategy. Key design objectives will be to incorporate passive safety features and to assure that the thermal stresses resulting from planned and unplanned accelerator beam interruptions do not excessively limit the lifetime of transmuter structures and components. These system development efforts and supporting dynamic analyses are currently at an early stage. Note that heat transport systems and passive safety features using sodium coolant have been demonstrated for existing fast reactor systems and much of this technology can directly integrated into a sodium-cooled ATW system.

With respect to transmutation performance, the current study has focused on the equilibrium-cycle mass flows, assuming that TRU losses during recycle are negligible. Future studies are needed to assess the impact of non-zero TRU losses on the fuel cycle mass flows in general (including fuel composition effects) and the waste streams in particular. Moreover, a blanket management/control strategy should be developed for accommodating the evolution of fuel composition (and reactivity) during the transition to the equilibrium, as well as for variations in the LWR feedstock composition and other deviations from equilibrium conditions.

Significant R&D efforts will be required to confirm the feasibility of non-uranium fuels and of the targeted high recovery factors in the recycle/refabrication of this fuel type. These R&D requirements are discussed elsewhere [11, 29]. A related need in the Systems area is the definition and modeling of the recycle waste streams. This evaluation should be conducted as part of a larger effort to characterize the waste generation for the entire ATW system—both during operation and in the stage of facility decontamination and decommissioning.

References

9   "Accelerator-Driven Transmutation of Waste (ATW): A Six-Year Science-Based Technology Development Program," Los Alamos National Laboratory, Rev. 0, March 17, 2000.

References (continued)

10 D. J. Hill, *et al*., "A Roadmap for Developing ATW Technology: Systems Scenarios and
Integration," Argonne National Laboratory Report ANL/RE-99/16, September 1999.

11 F. Venneri, *et al*., "Roadmap for the Development of Accelerator Transmutation of
Waste: Target and Blanket System," Los Alamos National Laboratory Report
LA-UR-99-3022, September 1999.

12 B. W. Spencer, "The Rush to Heavy Liquid Metal Reactor Coolants—Gimmick or
Reasoned," ICONE-8729, *Proceedings of 8th International Conference on Nuclear
Engineering (ICONE 8)*, Baltimore, MD, April 2000.

13 R. N. Hill, *et al*., "Physics Studies of Weapons Plutonium Disposition in the Integral Fast
Reactor Closed Fuel Cycle," *Nuclear Science and Engineering*, 121, 17-31, 1995.

14 "A Roadmap for Developing Accelerator Transmutation of Waste (ATW) Technology—A
Report to Congress," DOE/RW-0519, October 1999.

15 E. L. Gluecker, "U.S. Advanced Liquid Metal Reactor (ALMR)." *Progress in Nuclear
Energy*, 31, 43-62, 1997.

16 R. D. Legett and L. C. Walters, "Status of LMR Fuel Development in the United States,"
J. Nuclear Materials, 204, 23-32, 1993.

17 W. S. Yang and H. Khalil, "ATW System Point Design Employing LBE Cooled Blanket,"
Draft ATW Report, July 15, 2000.

18 B. J. Toppel, "A User's Guide to the REBUS-3 Fuel Cycle Analysis Capability," ANL-83-
2, Argonne National Laboratory, 1983.

19 W. S. Yang and H. S. Khalil, "Analysis of the ATW Fuel Cycle Using the REBUS-3 Code
System," *Trans. Am. Nucl. Soc*., 81, 277, 1999.

20 H. Henryson II, *et al*., "MC2-2: A Code to Calculate Fast Neutron Spectra and Multigroup
Cross Section," ANL-8144, Argonne National Laboratory, 1976.

21 W. M. Stacy, Jr., *et al*., "A New Space-Dependent Fast-Neutron Multigroup Cross-
Section Processing Capability," *Trans. Am. Nucl. Soc*., 15, 292, 1972,

22 R. D. Lawrence, "The DIF3D Nodal Neutronics Option for Two- and Three-Dimensional
Diffusion Theory Calculations in Hexagonal Geometry," ANL-83-1, Argonne National
Laboratory, 1983.

References (continued)

23 K. L. Derstine, "DIF3D: A Code to Solve One-, Two-, and Three-Dimensional Finite-Difference Diffusion Theory Problems," ANL-82-64, Argonne National Laboratory, 1984.

24 G. Palmiotti, E. E. Lewis, and C. B. Carrico, "VARIANT: Variational Anisotropic Nodal Transport for Multidimensional Cartesian and Hexagonal Geometry Calculation," ANL-95/40, Argonne National Laboratory, 1995.

25 B. C. Na, P. Wydler, and H. Takano, "OECD/NEA Comparison Calculations for an Accelerator-Driven Minor Actinide Burner: Analysis of Preliminary Results," Second Workshop on Utilization and Reliability of High Power Proton Accelerators, OECD Nuclear Energy Agency, Aix-en-Provence, France, November 22-24, 1999.

26 W. S. Yang and H. Khalil, "System Development Analyses," ATW Program Monthly Report, April 2000.

27 Personal Communication, Steven L. Hayes and Douglas C. Crawford, June 28, 2000.

28 R. N. Hill, "LWR Feed Inventory Specification for ATW System Studies," Argonne National Laboratory Intra-Laboratory Memo, June 12, 2000.

29 D. C. Crawford, *et al*., "Accelerator Transmutation of Waste: Fuel Development Plan for FY'01 through FY'05", June 29, 2000 (draft).

3 System Point Design Employing an LBE-Cooled Blanket

3.1 Introduction

A transmuter concept that received extensive review in the ATW Roadmap [30] is an LBE-cooled fast-spectrum transmuter. This coolant offers several attractive features in a transmuter environment:

- Lead and bismuth are excellent spallation target materials, with spallation neutron production rates on par with the best sub-actinide elements. Thus the coolant could, if practicable, be used as the target material.

- The eutectic has a relatively low melting point (as low as 124 ºC), offering the option of operating the system at low temperatures. Further, its high boiling point (1670 ºC) offers a margin of safety.

- LBE is not reactive with water, so direct heat exchange with water is straightforward (although steam flashing may be a concern).

- The high atomic masses of lead and bismuth preserve a very hard neutron spectrum, allowing for large coolant channels in the transmuter.

- Both lead and bismuth have low neutron absorption cross sections, offering good neutron economy.

These attributes have led researchers in the past to consider the use of liquid lead, bismuth, and LBE as reactor coolants. Indeed, the Russians have successfully implemented LBE as a coolant in a class of Russian nuclear submarines, and have proposed a power reactor concept, the BRUS-300, that uses LBE coolant [31]. In the 1950's and 1960's, researchers at Brookhaven National Laboratory investigated a liquid metal fuel reactor concept, predicated on liquid U-Bi fuel flowing through a graphite core [32].

Further discussions on the merits of LBE coolant and of the issues associated with its use in ATW can be found in the reports of the ATW Roadmap working groups [33, 34]. Spencer, *et al*. [35] provide an in-depth summary of the key neutronic, thermal hydraulic, material compatibility, coolant chemistry, and coolant activation characteristics of LBE and other fast reactor coolants.

The scope and objectives of the SPD are detailed in the Section 3.2. Section 3.3 provides results of parametric studies conducted to evaluate tradeoffs associated with adoption of various design parameters and operating strategies. Design parameters and performance characteristics for the blanket point design selected on the basis of these parametric studies are provided in Section 3.4. Section 0 summarizes conclusions of the SPD development studies and addresses requirements for (a) further development of the SPD, including

subsystems other than the transmutation blanket, and (b) assessment of key "interface" issues affecting the coupling of the various subsystems.

3.2 Scope and Objectives

The primary objective of the system development efforts has been to achieve efficient transmutation of the TRU separated from LWR spent fuel. It is generally recognized that a fast neutron energy spectrum is needed to accomplish the transmutation of minor actinides efficiently, because the fission-to-capture ratio for several key TRU nuclides is significantly greater in a fast spectrum [36]. The higher capture probability per incident neutron in a thermal spectrum causes build-up of the higher actinide fraction in the proportion of the TRU loading not consumed by fission, which adversely impacts neutron balance at high burnup and complicates recycle if the burnup is incomplete. On the other hand, the higher TRU inventory of fast systems for a given power level implies a lower specific power and a correspondingly lower burnup rate. Moreover, the fuel irradiation time in a fast spectrum is limited by radiation damage to structural materials caused by the high flux of fast neutrons. Consequently, fuel burnup in a fast system is generally incomplete in one pass through the transmutation blanket, and *recycle of discharged fuel is required to achieve an acceptably low TRU content in the waste stream*. The point design for the LBE system assumes that fuel recycle is performed using pyrochemical techniques referred to as "PYRO-B" in the ATW Roadmap [30].

The major assumptions made in developing the LBE SPD are similar to those employed in the ATW Roadmap as a basis for estimating ATW system costs and analyzing deployment scenarios; they can be summarized as follows:

A high-power linear accelerator generates a beam of energetic (~1 GeV) protons for delivery to a target/blanket "transmuter" system; the proton beam impinges on a spallation target and produces a source of neutrons that drives the subcritical blanket. The proton beam is delivered vertically downward onto a liquid LBE target that is approximately 50 cm in diameter and sufficiently long to range out the primary protons. Approximately 25 spallation neutrons leak to the surrounding subcritical blanket per proton delivered on target.

The blanket is fueled with solid, uranium-free fuel clad with a low-swelling stainless steel alloy similar to the HT-9 alloy developed in the U.S. ALMR Program [37, 38]. The fission power level of each transmuter module is 840 MWth—consistent with the ALMR power level selected on the basis of favorable economics (through modular fabrication and installation) and excellent safety (passive removal of decay heat using ambient air as an inexhaustible heat sink).

The transmutation blanket is coupled to systems for heat removal, steam generation and electricity production. The chemical inertness of LBE (no rapid reaction with air or steam/water) introduces the possibility of eliminating the intermediate heat transport loop conventionally employed in sodium-cooled liquid metal reactors; steam generator modules can thus be placed in the vessel containing the transmuter and its primary heat removal system (pool-type arrangement).

Chemical separations required to extract uranium and fission products from the LWR discharge fuel are performed with the UREX process [30], and the TRU-containing output stream from this process is treated with a subsequent pyrochemical process, "PYRO-A," to produce metallic TRU feed for use in ATW fuel fabrication. Recovery of the TRU remaining in the ATW fuel after irradiation in the ATW blanket is performed using the "PYRO-B" process [30]. To minimize off-site shipments of nuclear materials, the (modular) facilities required to accomplish the separations and to incorporate process wastes into durable waste forms suitable for disposal are collocated with the accelerator and transmutation subsystems at the ATW plant site.

Key long-lived fission products (I-129 and Tc-99) are separately recovered during the LWR spent fuel pre-treatment steps. It has not yet been decided whether to immobilize these species in suitable waste forms or to transmute them in the ATW blanket. Accordingly, initial system development efforts have focused on transmutation of TRU only. This approach provides a basis for future evaluations of overall system impacts of LLFP transmutation.

The central objective of the system development studies conducted to date has been to define the characteristics of a transmutation system that minimizes transuranic losses to the waste streams. It should be emphasized that neither the feasibility nor optimality of the system developed with this objective has been demonstrated; for example, alternative systems may exhibit superior economic or safety performance. Additional studies will be needed in the future to refine the point design and to optimize it with respect to a broader set of criteria.

As shown in Section 3.3, the objective of minimizing TRU losses to the waste stream is accomplished by maximizing the discharge burnup of ATW fuel (to minimize the number of recycle passes) and minimizing the fractional TRU loss per pass in recycle and refabrication. The achievable discharge burnup is believed to be constrained primarily by the fast-neutron irradiation damage to the cladding (fast fluence limit). The discharge burnup value currently targeted (~30 atom%) is high for conventional LMR fuels and remains to be demonstrated for the metallic dispersion fuel currently identified as the reference fuel form for the LBE-cooled transmuter. However, this burnup appears to be a reasonable development goal for the dispersion fuel type, particularly uranium-free fuels employing a non-fissioning matrix (e.g., zirconium or molybdenum); at a fixed heavy atom (fractional) burnup, the fission product density is much lower with a non-fissioning matrix than with a U matrix. If fuel burnup is governed by fission product accumulation, non-uranium fuels can be expected to achieve higher burnup fractions.

Analyses of the LBE SPD have so far focused primarily on the equilibrium fuel cycle, because system performance under equilibrium conditions is believed to be a good basis for design optimization. Moreover, the analyses have mostly assumed a specific composition for LWR-discharge TRU. Performance of the system under non-equilibrium conditions, and for a range of LWR-discharge TRU compositions are of interest, but have been only preliminarily explored as discussed in Section 3.3. In the equilibrium cycle, the charged fuel contains the transuranics recovered via recycle from the discharged fuel, supplemented by LWR-discharge TRU to make up for the TRU deficit in

the recycled component (i.e., for the ~30% TRU consumed by fission each cycle). Determination of the equilibrium composition has so far neglected the very small proportion of TRU lost during recycle and refabrication.

3.3 Parametric Studies

This section describes parametric studies conducted to evaluate tradeoffs associated with adoption of various design parameters and operating strategies for the LBE transmutation system. These parametric studies have focused primarily on achieving two important and somewhat contradictory performance objectives:

1. maximizing discharge burnup, so as to minimize the number of successive recycle stages and associated recycle losses, and

2. minimizing burnup reactivity loss over an operating cycle, to minimize reduction of source multiplication with burnup.

A wide range of potential transmuter designs have been examined, starting with the 840 MWth "pure burner" PRISM ALMR design previously developed at ANL for weapons-grade plutonium disposition [36]. The burner design was converted to an accelerator-driven LBE-cooled subcritical system by replacing the central assemblies with an LBE target and the sodium coolant with LBE. To reduce the possible ranges of design parameters, a set of design constraints for an LBE-cooled system were first developed. Possible ranges of the coolant and fuel volume fractions and the blanket power density were derived based on these design constraints.

Within this reduced design parameter space, studies aimed at maximizing the discharge burnup were first pursued with the fuel residence time and cycle duration fixed. Variations in the fuel pin diameter and pitch (i.e., variations in fuel, coolant, structure volume fractions), assembly height, and blanket size and arrangement were analyzed. Possible approaches to reducing the burnup reactivity loss while simultaneously achieving high discharge burnup were subsequently investigated. In addition, the effects of variations of the fuel matrix material and of the LWR-discharge TRU composition were analyzed.

The remainder of this section is organized as follows: The rationale for the selected performance objectives is discussed in Section 3.3.1. The imposed design constraints are presented in Section 3.3.2, and computational methods applied in the various analyses are described in Section 3.3.3. Parametric studies focused on maximizing discharge burnup are summarized in Section 3.3.4; these studies evaluate alternative assembly designs, blanket sizes and configurations, and fuel matrix materials, as well as the use of absorber materials. Finally, in Section 3.3.5, blanket design approaches to reducing the burnup reactivity loss are described.

3.3.1 Performance Objectives

The main purpose of the ATW system is to facilitate spent fuel disposal by removing the TRU and LLFP from the spent fuel and transmuting these constituents in the ATW blanket. Accordingly, one practical measure for the performance of the ATW system is the fraction of the initial TRU inventory that is not transmuted and lost to the waste stream; minimization of this fraction is obviously desirable. As discussed below, the goal of minimizing this fractional loss motivates the design for maximum discharge burnup. On the other hand, the source multiplication in the subcritical blanket decreases with burnup due to the reactivity loss. In order to minimize the resulting needs for increasing accelerator power and/or introducing an excess reactivity that would have to be compensated via active reactivity control, it is desirable to minimize the burnup reactivity loss. Therefore, maximizing discharge burnup and minimizing burnup reactivity loss over an operating cycle were chosen as the primary performance objectives in the physics design of the LBE-cooled blanket.
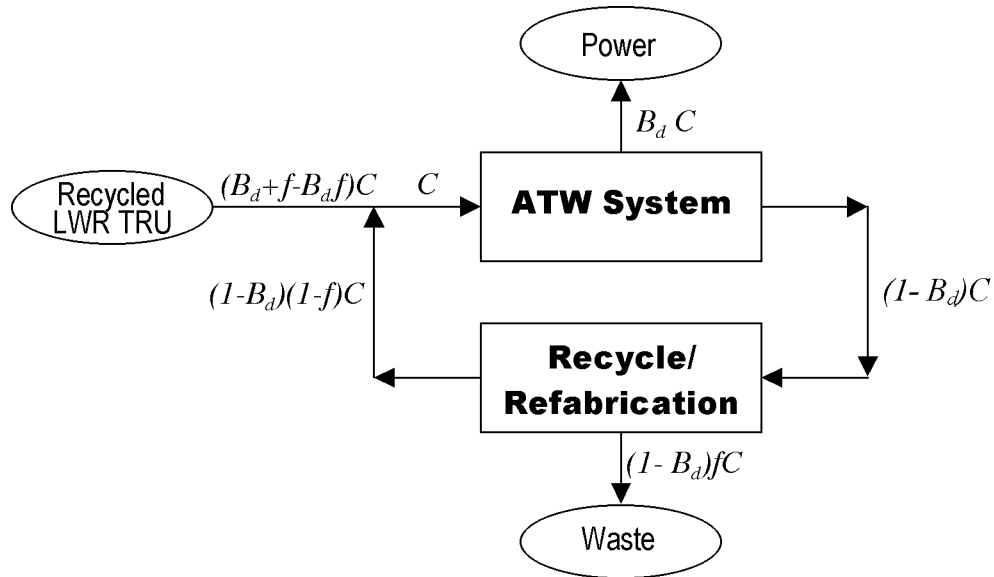
Figure 3-1. Schematic Diagram of TRU Mass Flows in the Equilibrium Cycle

As illustrated in Figure 3-1, if C is the equilibrium amount of TRU charged to the blanket per cycle and B_d is the equilibrium-cycle fractional discharge burnup, then $B_d C$ is converted into energy and $(1 - B_d)C$ is discharged from the blanket each cycle. Denoting the fraction of TRU lost in recycle/refabrication as f, then $(1 - B_d)(1 - f)C$ is reloaded into the blanket, and the amount of LWR-discharge TRU supplied as makeup for TRU consumed by fission becomes $(B_d + f - B_d f)C$. Consequently, the fractional loss of the initial TRU inventory is given by

Equation 3-1
$$l_w = \frac{(1 - B_d)f}{B_d + f - B_d f}$$

In order to minimize this fractional loss, it is necessary to maximize the fractional discharge burnup and minimize the fractional loss in recycle/refabrication. Achievement of high

discharge burnup is thus an important goal for the ATW blanket design and fuel development tasks.

The incentive to minimize burnup reactivity loss can be illustrated by noting that the fission power produced by the subcritical blanket varies with static reactivity ρ as:

Equation 3-2 $P_{fission} \propto SI_s /(-\rho)$

where ρ is related to the effective multiplication factor k ($k < 1$) as $\rho = 1 - 1/k$, S is the spallation neutron source, and I_s is the source importance factor [39]. As transuranic actinides are depleted over an irradiation cycle, k decreases and ρ becomes more negative. Thus, absent compensating measures, the fission power declines with fuel depletion, making it difficult to design an economic heat removal system and, if the system produces electricity, reducing the generation of electric power whose sale is intended to reduce net system cost.

The decline in blanket fission power over an irradiation cycle can be mitigated in two ways:

1. Gradual addition of reactivity (e.g., by continuous replacement of depleted fuel with fresh fuel, by withdrawal of control rods, or by the use of burnable poisons).

2. Increase of the spallation neutron source strength S, by gradually increasing beam power.

Irrespective of the method used to compensate for the reactivity decline, there are strong economic and safety incentives to minimize the decline itself. For example, the use of control rods to compensate burnup reactivity loss adds to system complexity/cost and creates a potential accident initiator (inadvertent reactivity insertion through control rod withdrawal or ejection). Control on accelerator beam current requires an accelerator that is "over-designed" for the lower TRU depletion state early in the irradiation cycle and creates potential for source increase accidents.

Burnup reactivity loss over an operating cycle $\delta\rho_c$ can be expressed as the product of an average reactivity loss rate and the irradiation time per cycle T_{ci} (T_{ci} is the product of the capacity factor and the cycle duration T_c). Analogously, discharge burnup B_d can be expressed as the product of the specific power P_s and the *total* fuel irradiation time nT_{ci}, where n is the number of irradiation cycles. Recognizing that the reactivity loss over a cycle $\delta\rho_c$ is roughly proportional to the cycle burnup B_c, i.e.,

Equation 3-3
$$\delta\rho_c \propto B_c = B_d / n = P_s T_{ci}$$

it is readily apparent that attainment of a *high* discharge burnup B_d and *low* burnup reactivity loss $\delta\rho_c$ requires a sufficiently large number of irradiation cycles n to limit the cycle burnup B_c.

3.3.2 Design Constraints

Denoting the average power density (in W/cc) as q_v, the total fuel residence time (in days) in the blanket as T_R, and the fuel volume fraction as v_f, the discharge burnup B_d (in atom%) can be represented as:

Equation 3-4
$$B_d = c T_R q_v / v_f e_{tru}$$

where e_{tru} is the TRU mass per unit of fuel volume in the fuel and c is a constant. This relation suggests that the discharge burnup can be maximized by designing for the maximum power density and fuel residence time and the minimum fuel volume fraction and TRU mass loading in the fuel. However, these quantities are interrelated and limited by various design constraints as described below.

With lead-based coolant, corrosion and erosive wear of core structural materials are intensified as coolant velocity increases, and hence the coolant velocity must be limited [40]. Consequently, the coolant volume fraction must be large enough to provide adequate cooling. If the limiting coolant velocity (in m/sec) is V_c and the coolant temperature rise (in °K) is ΔT_c, the coolant volume fraction v_c should satisfy the following inequality:

Equation 3-5
$$v_c \geq \frac{p_f L_c q_v}{c_p \rho_c \Delta T_c V_c}$$

where p_f is in the power peaking factor, L_c is the active core height (m), and ρ_c (kg/m^3) and c_p (J/kg°K) are the coolant density and specific heat, respectively.

The peak linear power is constrained by the need to limit peak fuel centerline temperature. To satisfy the peak linear power limit, the fuel volume fraction should satisfy the following inequality:

Equation 3-6
$$v_f \geq \frac{\pi}{4} \frac{s_p p_f d^2 q_v}{q'_m}$$

where q'_m (W/m) is the limiting value of peak linear power, d is the fuel pin diameter, and s_p is the exposure-stage factor accounting for the higher power density of fresh fuel assemblies. For the reference TRU-Zr metallic dispersion fuel [41] and LBE coolant, a peak linear power limit of 33 kW/m (derived on the basis of simple heat transfer calculations) is assumed pending more detailed analytical and experimental evaluations.

The peak fast fluence and the discharge burnup are limited by the need to ensure the fuel pin integrity. In the proposed dispersion fuel where TRU-10Zr fuel particles are dispersed in a zirconium metal matrix, fission products are retained within the fuel particles, which are contained within the matrix. As a result, there is no conceptual (or experimentally determined) limit on achievable burnup. On the other hand, there is likely a fast fluence limit for the core structural material (assumed to be a low-swelling stainless steel alloy similar to HT-9), and the peak fast fluence limit is assumed to be ~4×10^{23} n/cm^2. This peak fluence limit on the blanket structural material constrains the fuel residence time, and hence the discharge burnup.

The TRU mass per unit of fuel volume (e_{tru}) is determined such that the desired sub-criticality level at BOC is achieved for the selected blanket configuration and fuel management scheme. This quantity is constrained by the maximum volumetric fraction of fuel particles (assumed here to be TRU-10wt%Zr) in the dispersion fuel. This maximum volume fraction is 50%, but lower volume fractions are preferred. A TRU-10Zr fuel particle volume fraction of 50% is equivalent to a TRU weight fraction of ~61% in the composite fuel.

The limitation on maximum coolant velocity constrains the allowable values of volumetric power density and coolant fraction. For a specified maximum coolant velocity, the minimum coolant volume fraction required for adequate cooling increases as the power density increases. On the other hand, the minimum *fuel* volume fraction required to satisfy the specified constraint on peak linear power increases as the power density increases, and hence by volume conservation the maximum *coolant* volume fraction decreases. Figure 3-2 shows the maximum and minimum coolant fractions estimated as functions of average power density for a peak linear power of 33 kW/m and typical values of core height (1.0 m), coolant temperature rise (150°C), and power peaking factor (1.5). Consequently, as Figure 3-2 shows, there exists an upper limit on the achievable power density. For example, if the coolant velocity limit is 2.0 m/sec, then ~175 kW/ℓ is the maximum feasible power density for fuel pins of 0.635 cm diameter.
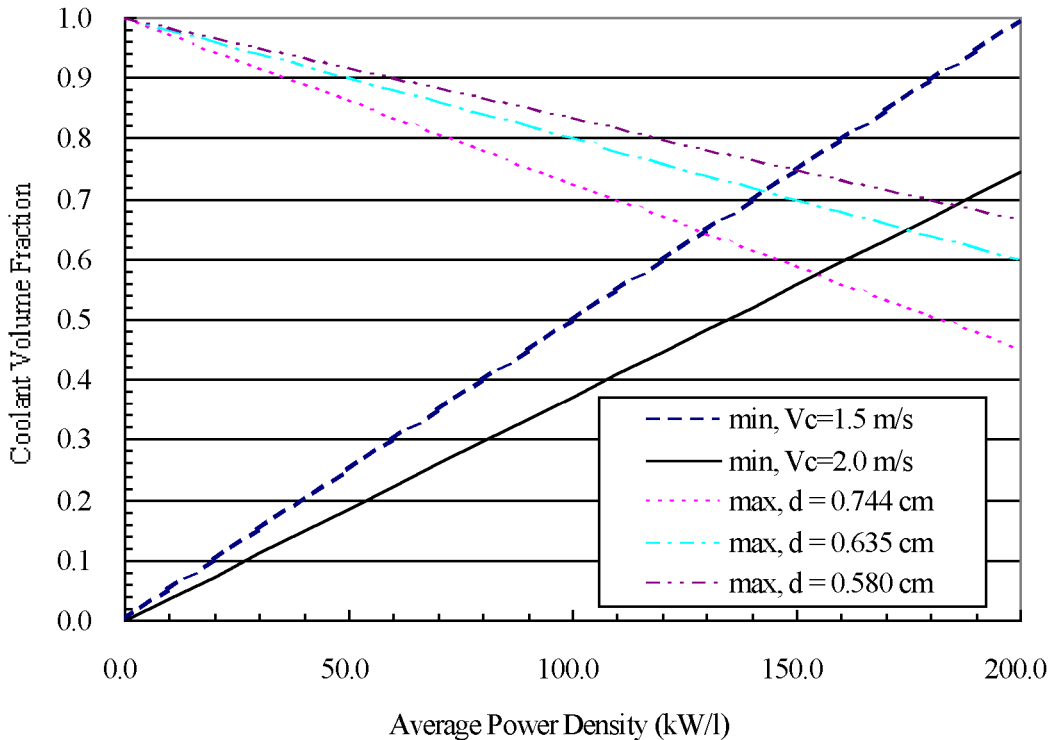
Figure 3-2. Coolant Volume Fraction versus Average Power Density

3.3.3 Computational Methods and Modeling Assumptions

3.3.3.1 Discrete Ordinates Methods

Analyses of the LBE SPD have so far focused primarily on the equilibrium fuel cycle, because system performance under equilibrium conditions is believed to be a good basis for design optimization. Equilibrium cycle performance characteristics were calculated using the REBUS-3 fuel cycle analysis code [42, 43]. In the REBUS-3 equilibrium cycle model, the charged fuel contains the transuranics recovered via recycle from the discharged ATW fuel, supplemented by LWR-discharge TRU to make up for the TRU consumed by fission. Determination of the equilibrium composition neglected the very small proportion of TRU lost during recycle and refabrication and assumed 5% of the rare-earth fission products are carried over by the recycled ATW TRU.

The TRU mass loading in the fuel which meets the targeted subcriticality level at BOEC (k_{eff} = 0.97) was determined using the REBUS-3 enrichment search techniques [42]. REBUS-3 also computes both batch-dependent and batch-averaged compositions at BOEC and EOEC for each specified depletion region. In this study, five (equal length) axial depletion zones were consistently used; in the planar direction, depletion zones consisted of

individual fuel assemblies or of neighboring assemblies with similar reaction rates. Axial expansion of the fuel was modeled in the depletion calculations as a uniform 5% axial expansion of the fresh fuel, based on IFR experiments for U-Pu-Zr ternary metal fuel; this likely overestimates the expansion effect for the proposed dispersion fuel.

REBUS-3 flux calculations can be performed using a variety of neutronics solution options. To determine the sensitivity of the results to the choice of solution option, analyses for an 840 MWth ATW blanket design were performed using different flux computational options as well as different geometries and mesh sizes. An operating cycle length of 145 days (at an assumed capacity factor of 75%) and a six batch refueling strategy were assumed. A scattered reloading scheme without fuel shuffling was employed, and two enrichment (TRU fraction in charged fuel) zones were used to flatten the power distribution. A comparison was performed of solutions obtained using the nodal diffusion option in hexagonal-Z geometry [44], the finite difference options in triangular-Z and R-Z geometries [45], and the VARIANT P_1 approximation in hexagonal-Z geometry [46]; both the inhomogeneous source calculation and the corresponding homogeneous eigenvalue calculation (i.e., a system without the spallation source made artificially critical by use of an eigenvalue to scale neutron production) were considered in the comparison to determine whether the latter type of calculation can be employed in the parametric physics design studies. Region-dependent multigroup cross sections used in the neutronics analyses are based on ENDF/B-V.2 and were generated for a 21-group energy structure using the MC^2-2 [47] and SDX [48] processing codes.

Table 3-1 compares the global equilibrium-cycle performance parameters for the various flux solution methods. These results show that the global performance parameters computed with different flux calculation methods are essentially the same. They also show that the integral parameters estimated with eigenvalue calculations are very similar to those obtained from inhomogeneous source calculations. Only the EOEC source multiplication factors differ significantly from the corresponding eigenvalues; this is attributed to differences in the flux distribution around the source region, which increase at EOEC due to the increased source intensity required to preserve the power level. These differences in the EOEC multiplication factor cause the indicated differences in burnup reactivity loss, because the burnup reactivity loss was simply estimated as the difference between the BOEC and EOEC multiplication factors.

**Table 3-1. Comparison of Equilibrium Cycle Performance Parameters Obtained with Various
REBUS-3 Flux Computation Options**

Parameter		DIF3D-nodal (Hex-Z)	VARIANT (Hex-Z)[a]	DIF3D-FD (6 tri/hex)[b]	DIF3D-FD (24 tri/hex)[c]	DIF3D-FD (R-Z)
Homogeneous Eigenvalue Problem						
TRU Fraction of Fresh Fuel (volume%)	Low	22.26	22.31	22.22	22.28	22.18
	High	26.71	26.77	26.66	26.74	26.62
Multiplication Factor (eigenvalue)	BOEC	0.97051	0.97001	0.96982	0.97012	0.96971
	EOEC	0.91629	0.91583	0.91552	0.91590	0.91530
Burnup Reactivity Loss (%)		5.4	5.4	5.4	5.4	5.4
Average Discharge Burnup (MWd/kg)		262	261	262	262	263
TRU Destruction Rate (kg/yr)		237	237	237	237	237
BOEC TRU Inventory (kg)		2361	2367	2356	2363	2351
Inhomogeneous Source Problem						
TRU Fraction of Fresh Fuel (volume%)	Low	22.36	22.43	22.35	22.42	22.34
	High	26.83	26.92	26.82	26.90	26.81
Source Multiplication Factor	BOEC	0.96958	0.96954	0.96970	0.97035	0.97044
	EOEC	0.90932	0.90945	0.90957	0.91064	0.91022
Burnup Reactivity Loss (%)		6.0	6.0	6.0	6.0	6.0
Average Discharge Burnup (MWd/kg)		261	260	261	260	261
TRU Destruction Rate (kg/yr)		237	237	237	237	237
BOEC TRU Inventory (kg)		2373	2380	2371	2379	2370

[a] P_1 approximation, 6th order polynomial inside a node, linear approximation for surface flux
[b] Triangular-Z geometry, 6 triangular meshes per hexagon
[c] Triangular-Z geometry, 24 triangular meshes per hexagon

Thus, for computational convenience, homogeneous (eigenvalue) neutronic calculations
performed using the hexagonal-Z nodal diffusion option of DIF3D were mostly employed as

a basis for optimizing the global design parameters of the ATW blanket. For the detailed analyses of the proposed LBE SPD, however, inhomogeneous source problems were solved using a "generic" spallation neuron source distribution generated for a 1-GeV proton beam and a prototypic LBE target [49]. Even though the spallation neutron source distributions depend on specific transmuter (target/blanket) configurations, the use of generic source distributions appropriate to the accelerator beam proton energy and the spallation target material and geometry yields sufficiently accurate performance estimates. Moreover, for these system point design analyses, the flux calculation method was switched from the hexagonal-z nodal option to the triangular-Z finite difference option of DIF3D to enable more accurate estimation of the peak flux, fluence and burnup values.

3.3.3.2 Monte Carlo Methods

Neutron transport in the LBE transmuter was modeled using the Monte Carlo radiation transport code MCNP. ENDF/B-VI continuous-energy cross sections were used in these calculations.

Time-dependent nuclide build-up and depletion were modeled using Monteburns [50], a code that couples MCNP with ORIGEN-2 [51]. In the ORIGEN-2 burnup calculations, Monteburns replaces one-group neutron absorption cross sections from the ORIGEN-2 library with more accurate one-group cross sections calculated by MCNP. Monteburns automatically updates nuclide inventories in the MCNP transport calculation at each time step. Absorption data for nuclides for which ENDF/B-VI data do not exist were taken from the ORIGEN-2 library.

3.3.4 Discharge Burnup Maximization Studies

In this section, optimization studies aimed at maximizing discharge burnup are presented. These studies were first focused on finding optimum values of such key system variables as power density (i.e., blanket size), fuel volume fraction, fuel residence time, etc., subject to the design constraints discussed in Section 3.2. The analyses assumed a TRU-Zr dispersion fuel and a specific composition for LWR-discharge TRU. After defining a partially optimized design on the basis of these studies, variations of the fuel matrix material and the LWR-discharge TRU composition were investigated.

As mentioned in Section 3.3, the 840 MWth PRISM ALMR design was used as the starting point for the optimization studies. The burner design was converted to an accelerator-driven LBE-cooled subcritical system by replacing the central seven assemblies with LBE target and buffer and the sodium coolant with LBE. The Pu-Zr binary metal fuel was changed to a TRU-Zr dispersion fuel, but the core structural material (HT-9) was retained, as were the compositions of the radial reflector and shield assemblies. For the parametric studies described in this section, fuel pin and assembly design parameters were varied while retaining the PRISM assembly lattice pitch (6.355 in). The number of fuel assemblies and the active fuel height were also varied.

For the neutronics calculation model, the assembly design geometric data were modified by correction factors to account for axial fuel expansion and cold-to-hot dimensional changes. The active fuel height was increased by 5% in the neutronics model, and the fuel density was uniformly decreased by 5%. In addition, the fuel and structural materials were assumed to thermally expand when they are heated to operating temperatures. Uniform radial and axial expansion factors of 1.00596 and 1.00489 were assumed based on SS-316 gridplate expansion and HT-9 cladding expansion from room temperature to full power conditions; thus the fuel and structural densities were modified by a factor of 0.98338.

3.3.4.1 *Effects of Blanket Size and Material Volume Fractions*

Equation 3-4 shows the discharge burnup increases as the power density and the fuel residence time increase and as the fuel volume fraction and the TRU content of the fuel decrease. The TRU content of the fuel is determined by the requirement that the multiplication factor at BOEC satisfies a desired value, e.g., 0.97. Thus it is a function of blanket size, material volume fractions, cycle duration, number of batches, and so on. Consequently, the discharge burnup also depends on these factors in addition to being proportional to the power density and fuel residence time. To meet the high discharge-burnup goal, optimum values of blanket size and material volume fractions were first investigated *with the fuel residence time and cycle duration fixed*.

The LBE-cooled subcritical system obtained by minimally modifying the PRISM pure burner design has an average power density of 80 kW/ℓ. However, in order to increase the burnup rate, it is desirable to increase the power density as close to the maximum feasible value as possible. Furthermore, a more compact blanket configuration through a higher power density is desirable to decrease the system cost. Thus, several 840 MWth blanket configurations with higher power density were developed by reducing the number of assemblies. The average power density was varied up to 165 kW/ℓ, which is about the maximum power density achievable with the fuel pin diameters considered. The reduced number of fueled assemblies reduces the heavy metal inventory requirements and thus increases the rate of TRU consumption as a function of the initial inventory (increases burnup rate). Moreover, fuel-cycle costs are reduced because fewer fuel pins and assemblies would have to be fabricated. Figure 3-3 through Figure 3-7 show the planar view of the various blanket configurations analyzed.

Equation 3-6 indicates that the maximum power density increases as the pin diameter decreases. Accordingly, in developing the higher power-density ATW configurations, the fuel pin diameter was reduced from the PRISM value (0.744 cm) to that of the Fast Flux Test Facility (FFTF, 0.580 cm) while retaining the PRISM hexagonal assembly lattice pitch. The number of fuel pins per assembly was correspondingly varied between 96 and 271 to obtain adequate coolant-volume fractions.
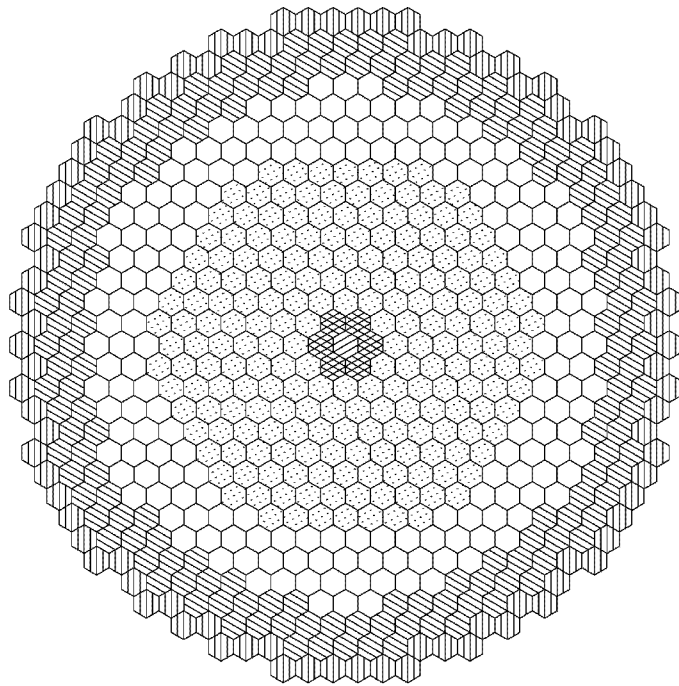
Target (1)   Buffer (6)
Low Enr. Driver (204)   High Enr. Driver (186)
Reflector (162)   Shield (90)

Target (1)   Buffer (6)
Low Enr. Driver (144)   High Enr. Driver (132)
Reflector (138)   Shield (78)

Figure 3-3.   Preliminary ATW Blanket Configuration Based on PRISM Pure Burner Design (*Equivalent Fuel Region OD = 3.38m*)

Figure 3-4.   276-Assembly Configuration (*Equivalent Fuel Region OD = 2.85 m*)

Target (1)   Buffer (6)
Low Enr. Driver (114)   High Enr. Driver (102)
Reflector (126)   Shield (72)

Target (1)   Buffer (6)
Low Enr. Driver (102)   High Enr. Driver (90)
Reflector (114)   Shield (66)
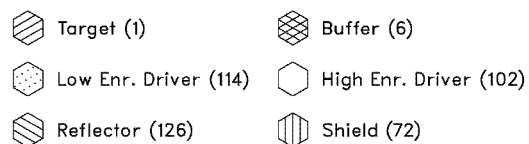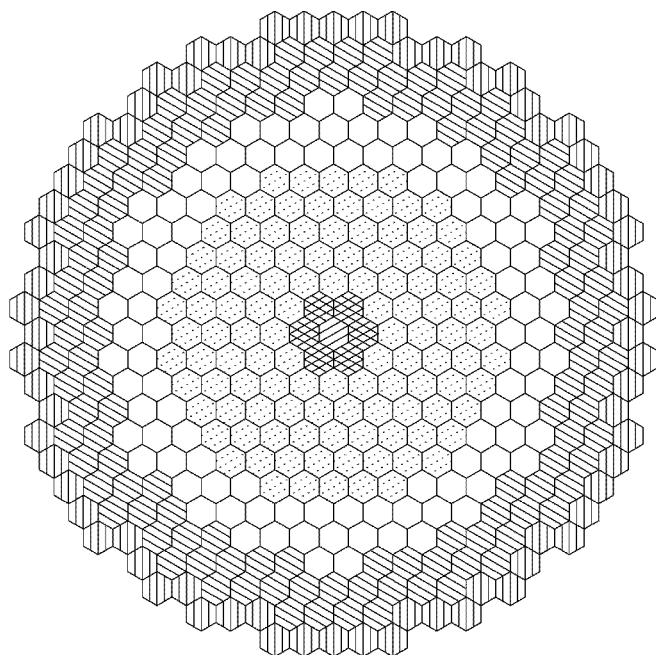
Figure 3-5.   216-Assembly Configuration (*Equivalent Fuel Region OD = 2.53 m*)
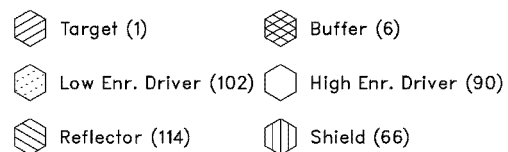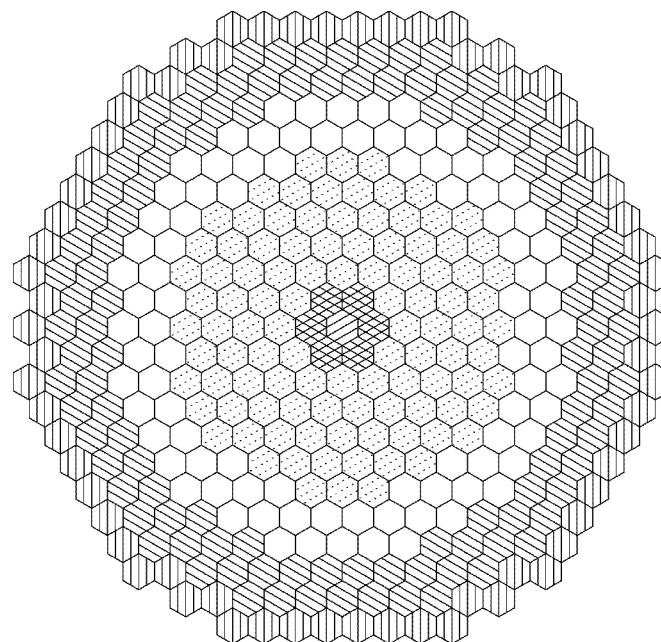
Figure 3-6.   192-Assembly Configuration (*Equivalent Fuel Region OD = 2.39 m*)
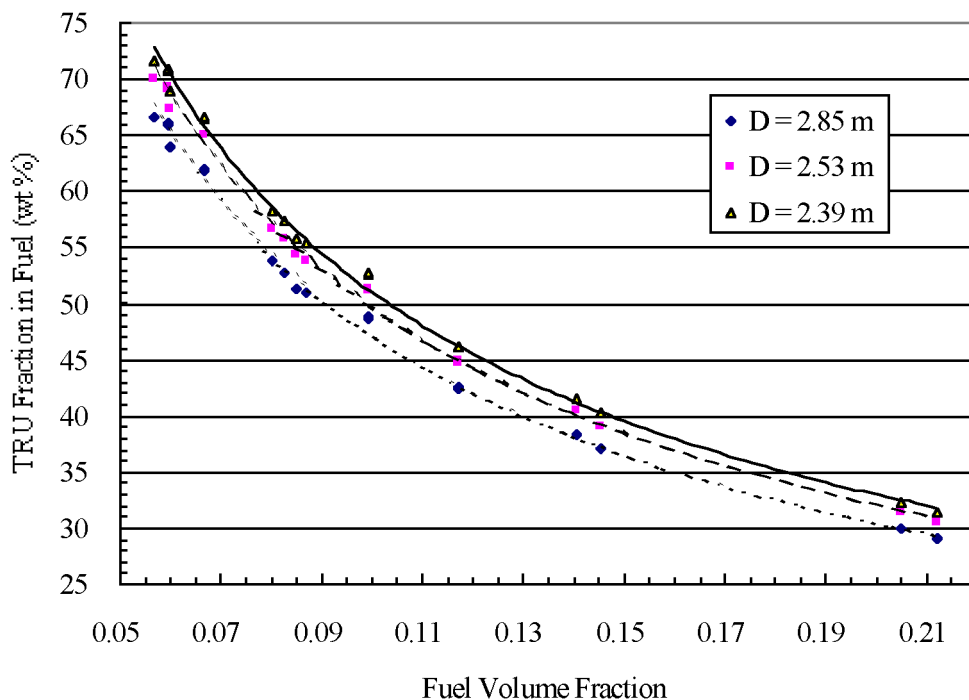
Figure 3-7.   TRU Fraction of Charged Fuel vs. Fuel Volume Fraction and Effective Fuel Region Diameter (D)

Figure 3-7 shows the required TRU weight fraction in fuel (assuming the TRU density is 15.9 g/cc and the Zr density is 6.5 g/cc) for a fixed fuel residence time as a function of the fuel volume fraction and the effective blanket diameter (excluding the reflector and shield). A fuel residence time of three years at 75% capacity factor was assumed with a cycle length of one year. The TRU weight fraction in fuel was calculated in each case such that the multiplication factor at the BOC is 0.97. These results show that the required TRU fraction in fuel decreases monotonically as the fuel volume fraction or the blanket size increases. The small fluctuations around the smooth fitting lines are due to the variations in cladding thickness and blanket geometry.

Since the TRU fraction in fuel is a monotonic function of fuel volume fraction and blanket size, the discharge burnup is also a monotonic function of these variables in the variable domain of interest. Figure 3-8 shows the discharge burnup calculated (for fixed fuel residence time) as a function of fuel volume fraction and equivalent blanket diameter; the curves in this figure are least squares fits. As shown in Figure 3-8, the discharge burnup increases monotonically as the fuel volume fraction and blanket size decrease. These results indicate that there is no extreme point in the variable domain of interest, and hence the maximum discharge burnup is obtained by designing for the minimum fuel volume fraction and blanket size. The minimum blanket size is constrained by the maximum coolant velocity and the peak linear power. The minimum fuel volume-fraction is limited by the smallest feasible pin diameter and the highest TRU content feasible in the dispersion fuel

form. In order words, *for a fixed fuel residence time*, the achievable discharge burnup is
limited by fuel fabrication and thermal-hydraulic design constraints.
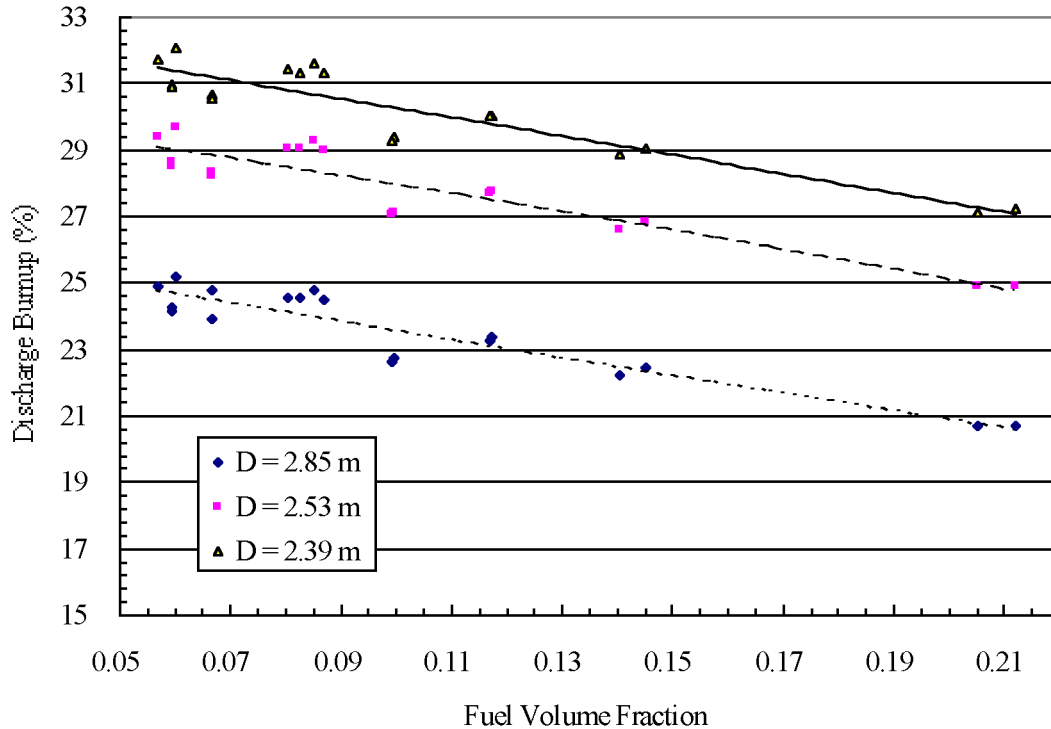
**Figure 3-8.   Discharge Burnup vs. Fuel Volume Fraction and Effective Fuel Region Diameter
(D)**

Since the same amount of energy is produced for fixed power level and fuel residence time,
the maximum discharge burnup obviously corresponds to the minimum TRU inventory in the
blanket. The above results show that that the minimum inventory is achieved through
minimum blanket size and pin diameter, and maximum TRU content in fuel. However, this
minimum fuel inventory yields the largest burnup reactivity loss since the burnup reactivity
loss is proportional, for fixed cycle duration, to the discharge burnup as discussed in
Section 3.3.5.

The above results also indicate that the maximum discharge burnup achievable *with three-
year residence time* is ~30% under reasonable fuel fabrication and thermal-hydraulic design
constraints. The TRU fraction in fuel required to attain this burnup level is about 30% by
volume, which corresponds to a 51% TRU mass fraction in the fuel. In order to increase the
discharge burnup significantly over 30%, the fuel residence time would have to be
increased. The allowable increase in fuel residence time is limited by the peak fluence limit
on the structural material. The peak fast fluence based on a three-batch annual refueling
scheme is compared for the zirconium and molybdenum matrix fuels *as functions of burnup*
in Figure 3-9. It shows that the peak fast fluence is proportional to the discharge burnup for
both the zirconium and the molybdenum matrix cases. It can be also seen from Figure 3-9

that the maximum discharge burnup achievable with these dispersion fuels is ~29% under the peak fast fluence limit assumed for HT-9 cladding (~4×10^{23} n/cm^2). These results indicate that the achievable discharge burnup would be constrained primarily by the fast-fluence irradiation damage to the cladding (fast fluence limit).
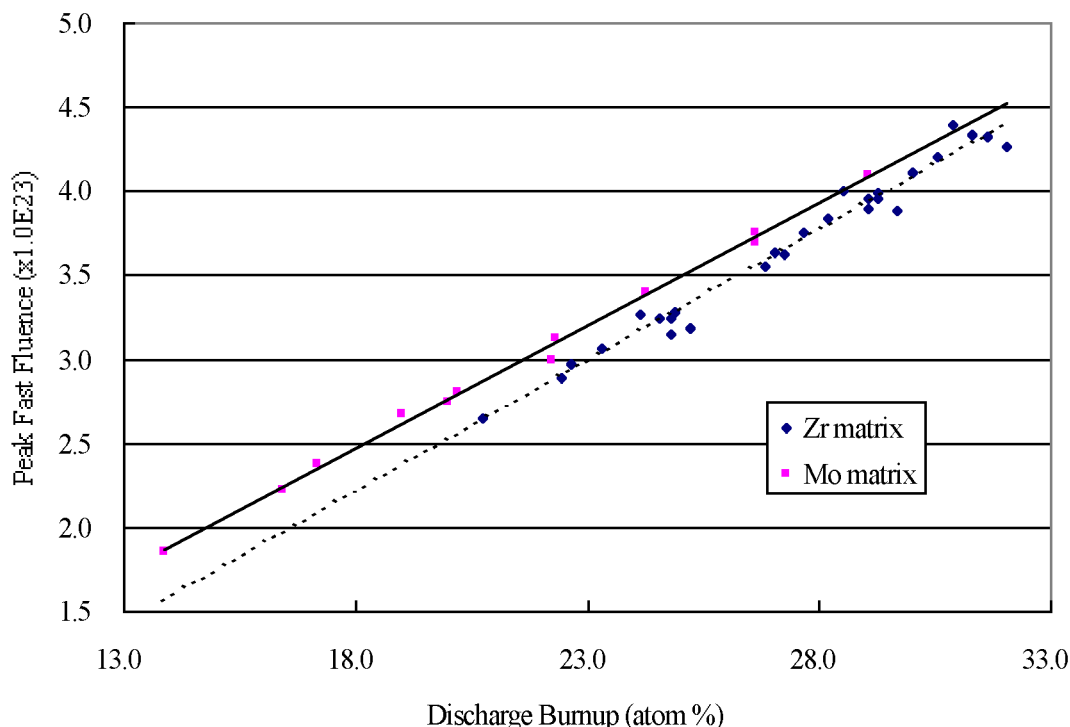
Figure 3-9.   Peak Fast Fluence vs. Discharge

Based on the results of the foregoing parametric studies, a preliminary LBE-cooled blanket was developed to achieve the targeted high discharge burnup under the constraints discussed in Section 3.3.2. Since the discharge burnup increases monotonically as the blanket size decreases, the relatively compact 192-assembly design shown in Figure 3-6 was selected as the blanket geometry. In order to attain the discharge burnup of ~29% achievable under the peak fast fluence limit (see Figure 3-9), the required fuel volume fraction appropriate for the selected blanket configuration was determined from Figure 3-8 to be ~0.14. The corresponding TRU volume fraction required for 3-batch annual refueling scheme was found to be ~22.5% (see Figure 3-7). To attain the targeted fuel volume fraction of ~0.14 while satisfying the thermal-hydraulic constraints previously discussed, a fuel pin diameter of 0.635 cm was selected.

The principal design parameters of this preliminary design are summarized in Table 3-2. For this design, equilibrium fuel cycle analyses were performed with 6-batch semi-annual refueling scheme as well as 3-batch annual refueling scheme to investigate the effects of cycle length on burnup reactivity loss. The total fuel residence time was kept the same in all cases, in keeping with the constraint on peak fast fluence. Neutronics calculations were performed using the hexagonal-Z nodal diffusion option of DIF3D, run in the eigenvalue

mode. The TRU composition of a 10-year cooled PWR spent fuel of 33 MWd/kg burnup was used to represent the composition of the LWR-discharge TRU feed-stream used as make-up for the TRU consumed by fission during each cycle.

Table 3-2. Design Parameters for the Preliminary LBE-Cooled Blanket Design

Pin Diameter (cm)			0.635
Cladding Thickness (cm)			0.056
Pitch-to-Diameter Ratio			1.727
Number of Pins per Assembly			217
Fuel Smear Density (%)			75
Volume Fraction (at operating temp.)	Fuel		0.140
	Structure		0.103
	Coolant		0.695
Hexagonal Assembly Pitch (cm)			16.142
Number of Assemblies	LBE Target/Buffer		7
	Fuel	Inner zone	102
		Outer zone	90
		Total	192
	Reflector		114
	Shield		66
TRU Fraction Split Factor (Outer Zone/Inner Zone)			1.2
Active Fuel Height (cm)			106.68
Equivalent Fuel Region Diameter (cm)			239.11
Maximum Blanket Diameter (cm)			345.20

Neutronics performance parameters are compared in Table 3-3. These results show that the discharge burnup of ~29% is achievable with the assumed three-year fuel residence time. The TRU mass fractions of the fuel required to obtain the targeted BOEC k_{eff} of 0.97 are well below the limit for dispersion fuel, even though a higher TRU fraction is used in the outer blanket zone than the inner zone to flatten the power distribution. The highest outer-zone value (46.2 wt%) is equivalent to ~33 volume% of TRU-10Zr fuel particles in the dispersion

fuel. Performance characteristics obtained for the 3-batch annual and 6-batch semiannual fuel management schemes are generally very similar, except for the burnup reactivity loss.

Table 3-3. Performance Parameters for the Preliminary LBE-Cooled Blanket Design

		Annual cycle	**Semiannual cycle**
Number of Fuel Batches		3	6
Cycle Irradiation Time (days)		273	145
TRU Fraction In Fuel (weight%)	Inner zone	38.6	40.3
	Outer zone	44.3	46.2
Multiplication Factor	BOEC	0.9695	0.9702
	EOEC	0.8566	0.9123
Burnup Reactivity Loss (%Δk)		11.3	5.8
Core-Average Power Density (kW/ℓ)		166.0	166.0
Power Peaking Factor	BOEC	1.45	1.45
	EOEC	1.45	1.45
Peak Linear Power (kW/m)		30.4	30.7
Discharge Burnup (atom%)	Average	29.1	29.1
	Peak	39.9	39.9
Peak Fast Fluence (10^{23} n/cm^2)		3.91	3.96
Net TRU Consumption Rate (kg/year)		237	237
Equilibrium Loading (kg/year)	LWR TRU	237	237
	Recycled TRU	581	579
	Total TRU	818	816
Heavy Metal Inventory (kg)	BOEC	2192	2256
	EOEC	1955	2130

By adopting the 6-batch semiannual refueling scheme instead of 3-batch annual refueling, the burnup reactivity loss is halved without affecting discharge burnup. The semiannual cycle case requires a slightly higher TRU fraction in the charged fuel, because the smaller proportion of the blanket (one-sixth) refueled each cycle in this case yields a slightly higher average burnup at BOEC. This results in an increased BOEC TRU inventory.

Sensitivity studies on the effect of clad and coolant fractions in the blanket were carried out using the Monteburns code. For these studies, a steady-state mode of operation was assumed, with base-case volume fractions of 55% coolant, 25% cladding, and 20% fuel. The fuel was composed of ~87% Zr, ~12% actinides, and ~1% fission products (Tc-99 and I-129). The cladding and coolant fractions were varied accordingly. Results appear in Table 3-4 below.

Table 3-4. Effect of Cladding Fraction on Steady-State Actinide Inventory and Power Density

Clad Vol. Fraction in Blanket	10%	18%	25%
Actinide Inventory (kg)	2200	2400	2500
Ave. Fuel Power Density (W/cc)	450	600	850

The larger cladding fractions have higher power densities because the zirconium-to-actinide ratio of the fuel is lower. This is due to the smaller fraction of fuel in the smeared mixture. Additionally, the actinide inventory increases with increasing clad fraction to overcome parasitic absorptions in the cladding. The higher steady-state inventory implies the discharge burnup decreases with increasing clad fraction.

3.3.4.2 Fuel Matrix Material Variations

As alternative to the zirconium matrix of the reference metallic-dispersion fuel form, the use of molybdenum matrix was considered, primarily because of its greater compatibility with the LBE coolant, implying that potential fuel pin failure might be more benign. Furthermore, molybdenum is a stronger absorber than zirconium; its use therefore increases the TRU inventory (which affects fractional TRU burnup and reactivity loss rates) and possibly introduces some Doppler feedback, which might be an important factor in mitigating the consequences of severe accidents.

To estimate the Doppler feedback contribution of the molybdenum matrix, a preliminary analysis was performed using the continuous-energy Monte Carlo code VIM [52]. The results showed that the molybdenum matrix provides no significant Doppler feedback. Additional parametric studies were performed to compare the fuel cycle performance of systems using Mo and Zr based fuels. For fixed values of BOC multiplication factor (k_{eff} = 0.97), fuel residence time and cycle length, the BOC TRU inventory was found to be ~33% greater with the Mo matrix than with Zr, due to the significantly greater Mo absorption cross section. As a result, discharge burnup and burnup reactivity loss with the Mo matrix fuel were each reduced by ~23% compared to corresponding values with the Zr matrix.

The peak fast fluence and the burnup reactivity loss based on a three-batch annual refueling scheme were compared for the two matrix materials *as functions of burnup*. As previously shown in
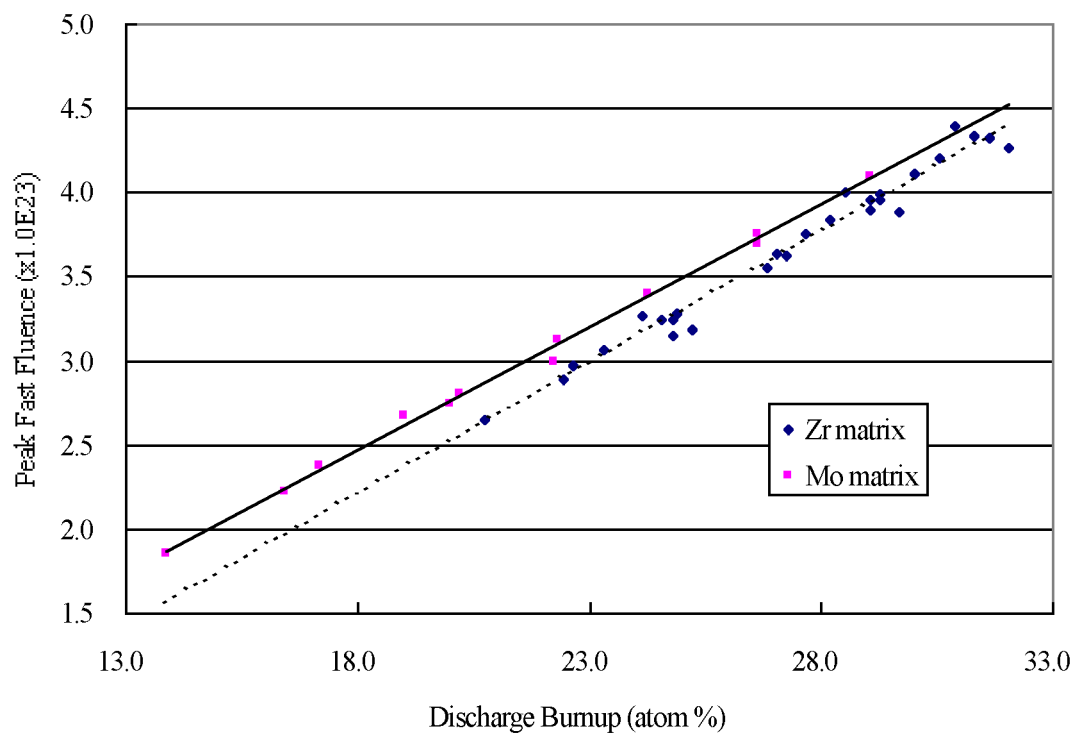
Figure 3-9, the peak fast fluence is proportional to the discharge burnup for both the zirconium and the molybdenum matrix case. It can be also seen from
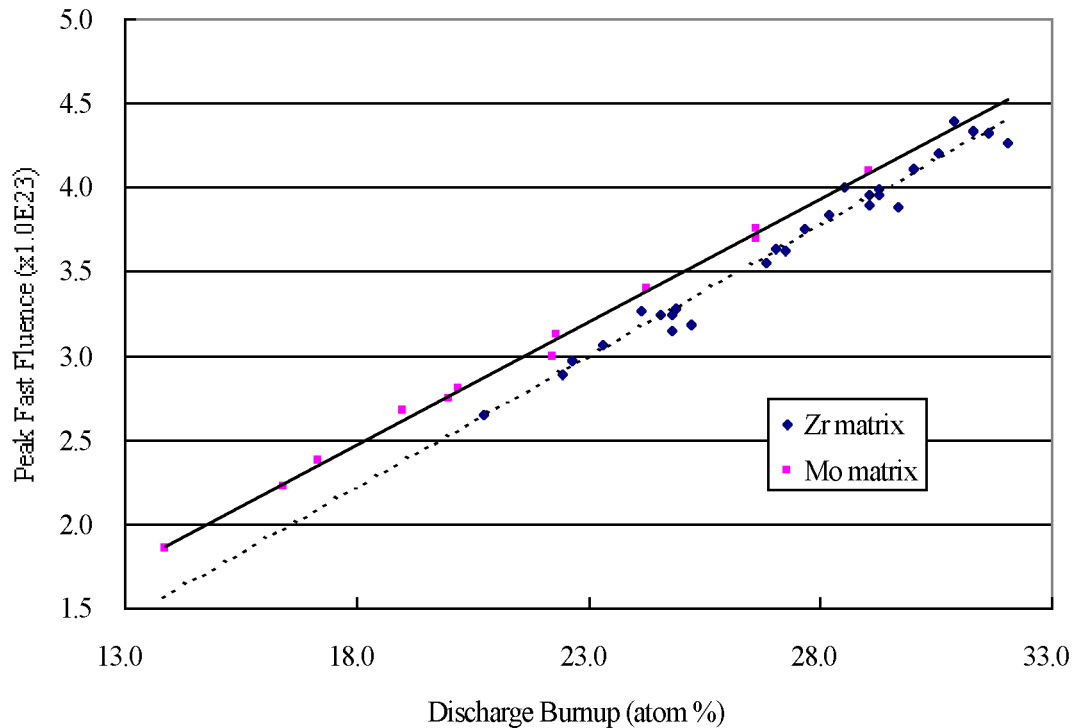
Figure 3-9 that the maximum discharge burnup achievable with the molybdenum matrix is slightly lower that that of the zirconium matrix fuel for a given peak fast fluence limit. In other words, under the same peak-fast-fluence limit, a slightly higher discharge burnup can be achieved with the zirconium matrix fuel than with the molybdenum. Figure 3-10 compares the burnup reactivity loss based on a three-batch annual refueling scheme for the two matrix materials *as functions of burnup*. It can be seen from Figure 3-11 that the burnup reactivity loss becomes slightly higher with the molybdenum matrix fuel when based on the same discharge burnup. (To achieve the same discharge burnup, the molybdenum matrix fuel requires a higher power density or a longer residence time.) *These results suggest that the molybdenum matrix has no advantage over the zirconium matrix from the neutronics point of view*.
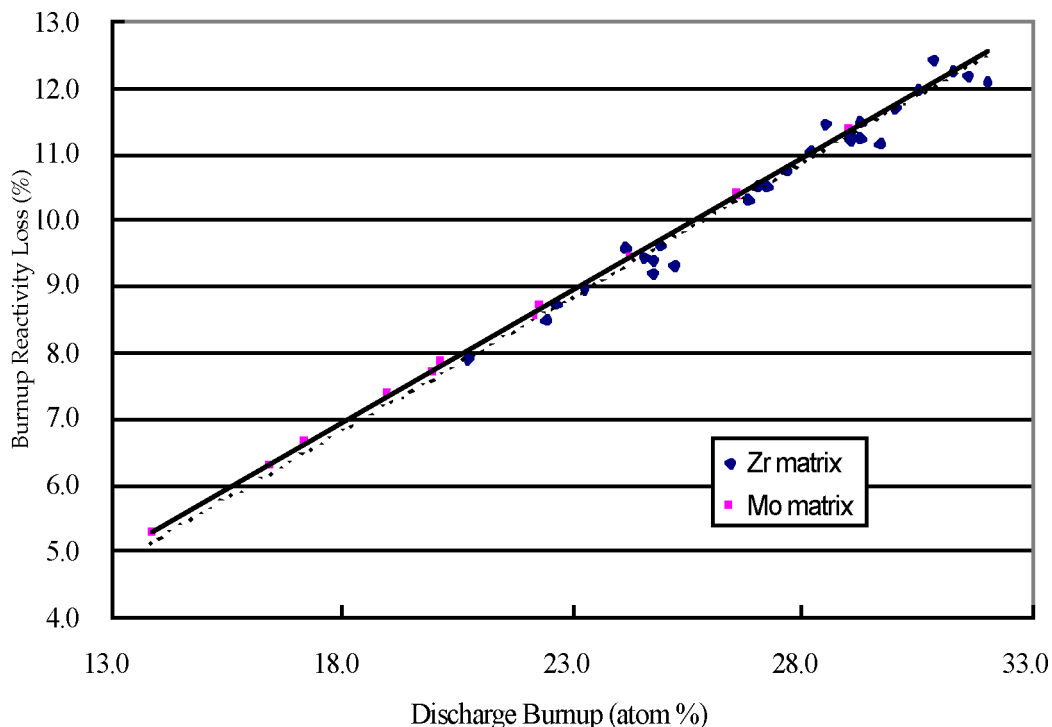
Figure 3-10. Burnup Reactivity Loss vs. Discharge
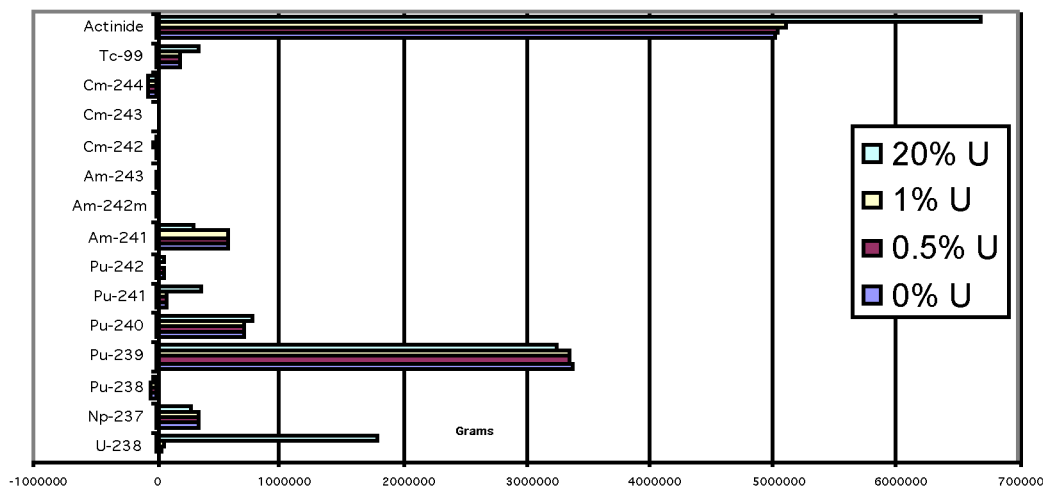
Figure 3-11. Net Destruction with Different U Feed Fractions

3.3.4.3 *Effect of LWR Discharge Composition Variations*

The isotopic composition of the LWR-discharge TRU used in the above-described parametric studies was derived from ORIGEN-2 [51] depletion calculations for a typical PWR assembly with a nominal burnup of 33 MWd/kg and 10-year cooling time. Because the LWR spent fuel inventory to be transmuted by ATW systems would in reality be composed

of spent fuel assemblies differing in assembly type, burnup level and cooling time, the ATW blanket needs to be designed with sufficient flexibility to accommodate different feed stream compositions; the option of blending different TRU feed streams to maintain a composition within a narrow range may not be feasible in practice. An investigation of the effects of different feed stream TRU compositions on neutronics and fuel-cycle performance characteristics is described in this section.

Table 3-5.   Isotopic Composition (wt%) of a PWR Assembly of 33 MWd/kg Burnup

	10-Year Cooling	30-Year Cooling
U-235	0.004	0.004
U-236	0.002	0.002
U-238	0.477	0.479
Np-237	4.839	5.101
Pu-238	1.428	1.225
Pu-239	53.101	53.227
Pu-240	21.437	21.550
Pu-241	7.770	2.976
Pu-242	4.675	4.689
Am-241	5.127	9.709
Am-242m	0.015	0.014
Am-243	0.925	0.926
Cm-243	0.003	0.002
Cm-244	0.184	0.086
Cm-245	0.009	0.009
Cm-246	0.001	0.001

For the preliminary LBE-cooled blanket configuration described in the previous section, equilibrium fuel cycle analyses were performed using two different feed streams: 10-year and 30-year cooled PWR spent fuel of 33 MWd/kg burnup. Table 3-5 compares the isotopic compositions of these two feed streams, based on 99.995% uranium removal. The main difference between the two compositions is in the Pu-241 and Am-241 proportions, due to the relatively short half-life of Pu-241 (~14 years); the other isotopic fractions are fairly similar. The effect of this composition difference on the computed equilibrium-cycle performance parameters is summarized in Table 3-6 for the 3-batch annual refueling

schemes. For fixed values of BOC multiplication factor (k_{eff} = 0.97), fuel residence time and cycle length, the BOC TRU inventory is seen to be slightly greater (by ~3% for annual refueling and by ~2.5% for semiannual refueling) with the 30-year cooled feed stream composition than with 10-year cooled composition. This inventory difference is due to the lower fissile (Pu-241) and higher fertile (Am-241) fractions in the 30-year cooled feed stream. As a result of the higher inventory, discharge burnup and burnup reactivity loss are lower with the 30-year cooled feed stream. However, the differences are not large, suggesting that variations in LWR-discharge composition can be readily accommodated and that the use of a "standard" LWR spent-fuel composition as a basis for design optimization is appropriate.

Table 3-6. Comparison of Blanket Performance Parameters for Two LWR TRU Feed Streams

		Spent-Fuel Cooling Time (years)	
		10	**30**
TRU Fraction In Fuel (weight%)	Inner Zone	38.6	39.4
	Outer Zone	44.3	45.1
Cycle Irradiation Time (days)		273	273
Multiplication Factor	BOEC	0.9695	0.9699
	EOEC	0.8566	0.8654
Burnup Reactivity Loss (% Δk)		11.3	10.5
Power Peaking Factor	BOEC	1.45	1.45
	EOEC	1.45	1.45
Peak Linear Power (kW/m)		30.4	30.1
Discharge Burnup (atom%)	Average	29.1	28.4
	Peak	39.9	39.3
Peak Fast Fluence (10^{23} n/cm^2)		3.91	3.88
Net TRU Consumption Rate (kg/year)		237	237
Equilibrium Loading (kg/year)	LWR TRU	237	237
	Recycled TRU	581	602
	Total TRU	818	839
Heavy Metal Inventory (kg)	BOEC	2192	2257
	EOEC	1955	2020

3.3.4.4 *Effect of Uranium Fraction in the ATW Feed Stream*

With the LWR waste separations processes currently contemplated for ATW, the amount of uranium that makes its way into the transmuter feed stream is predicted to be 0.005% of that originally in the LWR waste [53]. This translates into about 0.5% U in the ATW feed stream. Additional separations steps can be carried out to reduce this quantity, if deemed necessary. As a means of evaluating the impact of the U fraction in the feed stream, Monteburns calculations were carried out assuming U fractions ranging from 0 to 20%.

These were performed using the 1-GWt steady-state LBE system; results are shown in Table 3-7. After about 40 cycles (almost steady-state), the actinide feed rate required to maintain BOEC reactivity at k_{eff} = 0.97 increases as the fraction of uranium in the feed stream drops. This is due to breeding of Pu-239 from neutron capture by the U-238 in the feed. In contrast, the actinide inventory decreases with lower uranium fraction. The neutron economy (indicated by the quantity $\eta - k_{eff}$) is also better with higher U fraction in the feed because the breeding of Pu-239 means fewer neutrons are needed to maintain k_{eff}.

Table 3-7.   Results from Sensitivity Study on Uranium Fraction in Actinide Feed Stream

U Fraction in Feed Stream	0%	0.5%	1%	20%
Actinide Feed Rate (g/day)	1170	1150	1145	1100
Power Density (W/cc)	775	800	825	850
Inventory (kg)	2300	2350	2400	2500
$\eta - k_{eff}$	0.73	0.74	0.75	0.82

The net destruction (beginning inventory plus the amount of feed added during each cycle minus ending inventory) for the various isotopes is shown in Figure 3-11. Note that the net actinide destruction is greatest in the 20% U case, due to the larger quantity of U-238 destroyed. The initial Tc-99 content was spiked in the 20% uranium case as well (and not the others), which is why it had a greater net destruction. This could be an important aspect for future studies.

The results show that there were few major changes in the net destruction of other isotopes, indicating that differences between 0, 0.5, and 1% uranium has little effect on these preliminary transmutation calculations.

3.3.5 Burnup Reactivity Loss Reduction Studies

The preliminary LBE-cooled blanket configuration described in Section 3.3.4.1 was developed with the main objective of achieving high discharge burnup. In fact, this design yields the maximum discharge feasible burnup under the peak fast fluence constraint, which appears to be the limiting parameter for discharge burnup. On the other hand, this preliminary configuration also yields the largest burnup reactivity loss *for the selected (fixed) values of fuel residence time and cycle duration,* because the burnup reactivity loss is (under these conditions) proportional to the discharge burnup as shown in Figure 3-10. As discussed in Section 3.3.2, reduction of the burnup reactivity loss while retaining high discharge burnup requires an increased number of irradiation cycles to limit the cycle burnup. Reduction of cycle burnup (to reduce reactivity loss over the cycle) can be accomplished by decreasing the specific power or the cycle length (see Equation 3-3).

These two possible approaches to reducing burnup reactivity loss while simultaneously achieving high discharge burnup were studied. The first approach is to reduce the cycle length while retaining the comparatively high specific power of the preliminary blanket design. Keeping the 3-year fuel residence time (at 75% capacity factor), which is the longest irradiation time feasible under the peak fast fluence constraint assumed for the HT-9 structural material, the number of irradiation cycles was increased to six from three; this results in a half-year cycle duration. As shown in Table 3-3, the (fluence-constrained) discharge burnup is close to 30%. The burnup reactivity loss for this system is reduced from ~11% to ~5.8% by reducing cycle duration from one year to six months. Further reduction of the burnup reactivity loss to about 3% should be feasible with a 3-month cycle—at the expense of an increase to 12 in the number of irradiation cycles and in the associated number of fuel management batches.

Table 3-8.   Comparison of Design Parameters for the Low and High Specific-Power Designs

Parameter		Low Specific Power Design	High Specific Power Design
Fuel Pin Outer Diameter (cm)		0.744	0.635
Cladding Thickness (cm)		0.056	0.056
Pitch-to-Diameter Ratio		1.474	1.727
Hexagonal Assembly Pitch (cm)		16.14	16.14
Number of Fuel Assemblies		390	192
Volume Fractions	TRU-Zr Fuel	0.115	0.140
	HT-9 Structure	0.150	0.103
	Hf-Zr Absorber	0.142	-
	LBE Coolant	0.593	0.695
Maximum Blanket Diameter (m)		4.44	3.45

The alternative blanket design approach is to design for a low specific power and comparatively long cycle duration. Design requirements are apparent if the specific power is expressed as

$$P_s = cq_v / v_f \rho_{tru} \tag{3.3.1}$$

where q_v is the average power density (W/cc), v_f is the fuel volume fraction, ρ_{tru} is the TRU density in fuel, and c is a constant. This relation shows that the targeted low specific power can be achieved by designing for low power density and high TRU loading density. To obtain a low power density, the large blanket configuration derived from the PRISM pure burner design (see Figure 3-3) was used. To obtain a high TRU loading density, an

absorbing material (hafnium) was employed in the fuel assemblies. The use of Hf (a resonance absorber) not only raises the fuel inventory needed to achieve a specified multiplication factor *k*, but also contributes a (small) negative Doppler effect. Design parameters of this system are compared in Table 3-8 with those of the high specific-power system.

Table 3-9. Comparison of Performance Characteristics for the Low- and High- Specific Power Designs

	Low Specific-Power Design	High Specific-Power Design	
		Annual Cycle	6-Month Cycle
Number of Fuel Batches	10	3	6
Cycle Length (days)	273	273	145
Burnup Reactivity Loss (% Δk)	3.1	11.3	5.8
Core-Average Power Density (kW/ℓ)	83.0	166.0	166.0
Power Peaking Factor	1.59	1.45	1.45
Peak Linear Power (kW/m)	14.0	30.4	30.7
Average Discharge Burnup (atom%)	25.8	29.1	29.1
Peak Fast Fluence (10^{23} n/cm^2)	3.95	3.91	3.96
Net TRU Consumption Rate (kg/year)	242	237	237
Equilibrium Loading (kg/year) — LWR TRU	242	237	237
Equilibrium Loading (kg/year) — Recycled TRU	700	581	578
Equilibrium Loading (kg/year) — Total	942	818	815
BOEC Heavy Metal Inventory (kg)	8249	2192	2256

Equilibrium cycle analyses of the low power density were performed with an operating cycle length of 12 months at a capacity factor of 75%. The total fuel irradiation time was found to be 10 years under the assumed peak fast fluence constraint of ~4×10^{23} n/cm^2. The TRU loading was calculated such that k at BOC is 0.97. Calculated performance characteristics are compared in Table 3-9 with those of the high specific-power system described above. The burnup reactivity loss of this system (3.1%) is significantly lower than that of the high specific-power system (with either annual or semi-annual refueling), but its discharge burnup is also somewhat lower despite of a significantly longer fuel residence time (10 years). The blanket volume and TRU inventory for this system are substantially larger than the corresponding quantities for the high specific-power system. Fundamentally, this system exhibits a low reactivity loss because of the large number of fuel management batches; a comparably small cycle reactivity loss could be attained with the higher power density system by using the same number of batches (and proportionally reducing cycle duration).

The particular effect of employing the Hf absorber was also examined by analyzing the performance of the low specific-power system with the Hf removed from the fuel. As discussed in Section 3.4.2 in connection with use of Mo as a fuel matrix, an absorber increases the required TRU loading to achieve the desired subcriticality at BOC, and hence reduces the discharge burnup for a fixed residence time. Without the Hf absorber, the equilibrium TRU loading is reduced by ~31%, the discharge burnup (for fixed irradiation time) is increased by ~42%, and the burnup reactivity loss is increased from 3.1% Δk to 5.1% Δk.

In summary, the goal of achieving a low burnup reactivity loss, which is important for reasons of economics and safety, can be attained by design for either a low specific power or a short irradiation cycle time (or both). The low specific-power approach requires a low power density and high TRU inventory, as well as a large number of irradiation cycles (and fuel management batches) to achieve the targeted high discharge burnup. The short irradiation-cycle approach, which permits a blanket with higher power density and specific power, requires more frequent refueling. This latter approach is preferred at the present time because it employs a more compact (economical) blanket and because the more frequent refueling may not adversely impact system availability given the likely need for periodic shutdown for maintenance or replacement of accelerator, beam delivery and spallation target components.

3.3.6 Comparison of Different System Designs

Three modes of operation were explored using Monteburns. The basic geometry for all of them appears in Figure 3-12. The fixed parameters of a BOC k_{eff} = 0.97 and an EOC k_{eff} > 0.90 were set for all three cases.

The first mode of operation assumed a three-layer blanket surrounding an LBE target. This core ran for a four-month cycle, at which time the fuel was moved successively inward by one region. The innermost region was removed at the end of each cycle and underwent recycling that included the removal of fission products and uranium, and addition of new LWR-discharge TRU to offset fuel depletion by transmutation. This feed was then placed in the outermost region of the blanket to undergo another burnup cycle (in these scoping calculations, recycling is assumed to be instantaneous). The fuel resides in each of the three blanket regions for a single four-month cycle, for a total core residence time of one year.

Due to the waste generation and TRU losses anticipated with the back-end recycle process, a scheme in which the fuel is cycled through the core only once, without back-end recycling, was also evaluated. This design had nine concentric blanket regions, with new actinide material added to the outer region. Each cycle, fuel elements are progressively moved inward by one region. Spent fuel from the innermost region represents the waste stream to a repository.

Finally, a blanket composed of only two regions, one of low enrichment and one with high enrichment, was evaluated. As opposed to the other two cases, the operating mode for this

scheme did not include shuffling at the end of each cycle. Rather, one-third of the fuel in each region was replaced at the end of each cycle, so that each region contained three ages of fuel. With one-year cycles, the fuel residence time in the transmuter is three years. Again, there was no back-end recycling of the removed fuel assumed in this case.
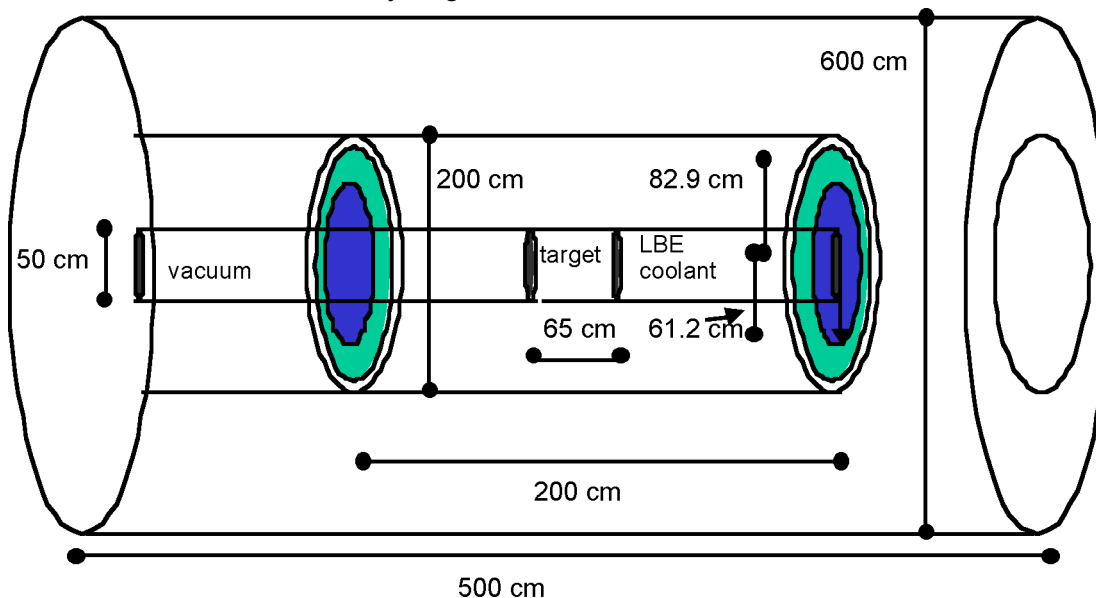
Figure 3-12. Basic MCNP Geometry of the LBE System

3.3.6.1 Recycle and Shuffling at the End of Each Cycle

The advantage of back-end recycling used in this example is that the waste stream consists of fission products extracted at each cycle, TRU-contaminated effluents from the recycling process, and the actinide inventory in the blanket at the "end" of plant life. Thus, over time, a steady-state condition is reached in which the amount of actinide feed being added is the same amount that is burned each cycle, thus reaching a steady-state inventory. The change in actinide inventory from beginning to end is shown in Figure 3-13.

The initial k_{eff} of the system is designed to be around 0.97. With the current scheme of fuel removal and shuffling, the reactivity decreases to around 0.92 during a four-month cycle. Initial calculations reveal that the beam current (assuming 1-GeV protons) for a cycle would have to be around 20 mA initially to supply the required power for a k_{eff} of 0.97. The beam requirement would increase over the cycle as the reactivity decreases unless appropriate control mechanisms were implemented to handle the reactivity swing.
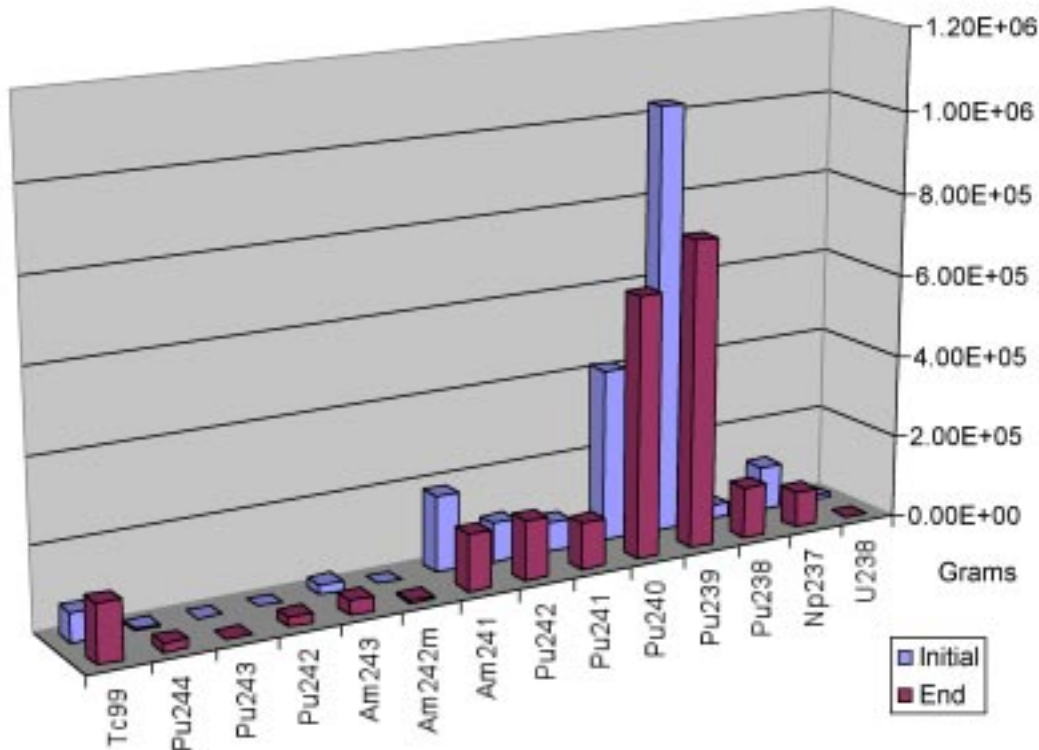
Figure 3-13. Inventories for Steady-State Case

3.3.6.2 *No Recycle, With Shuffling*

In the nine-region blanket of this case, fresh fuel is added to the outer region at the beginning of each cycle, and rods from the inner region are removed at the end of each cycle and sent to a repository. Rods are then moved inward one region at the end of each cycle, which is assumed to be one year in duration. The following figures show what fractional discharge burnup as a function of total irradiation time in the system (this is initial inventory plus all feed minus the amount left divided by the initial inventory plus feed). The imposed fuel clad fluence limit of 4×10^{23} n/cm^2 is reached at after about four years for a 1000 MWth system (or six years at 75% availability), with a corresponding discharge burnup of a little more than 40%. A reduction of the actinide inventory by less than a factor of two does not meet the ATW requirement of substantially reducing the waste stream entering a repository. This case demonstrates the need for back-end recycling of the discharged fuel from a fast-spectrum transmuter.

The change in reactivity over a year cycle for this case was unfortunately rather large (k_{eff} went from 0.97 to 0.85). This suggests that the cycle length should be shortened. Thus, another case was run with a cycle length around 9 months, which produced the desired drop

in reactivity from 0.97 to 0.90. The beginning and ending inventories for this system are shown in Figure 3-14.
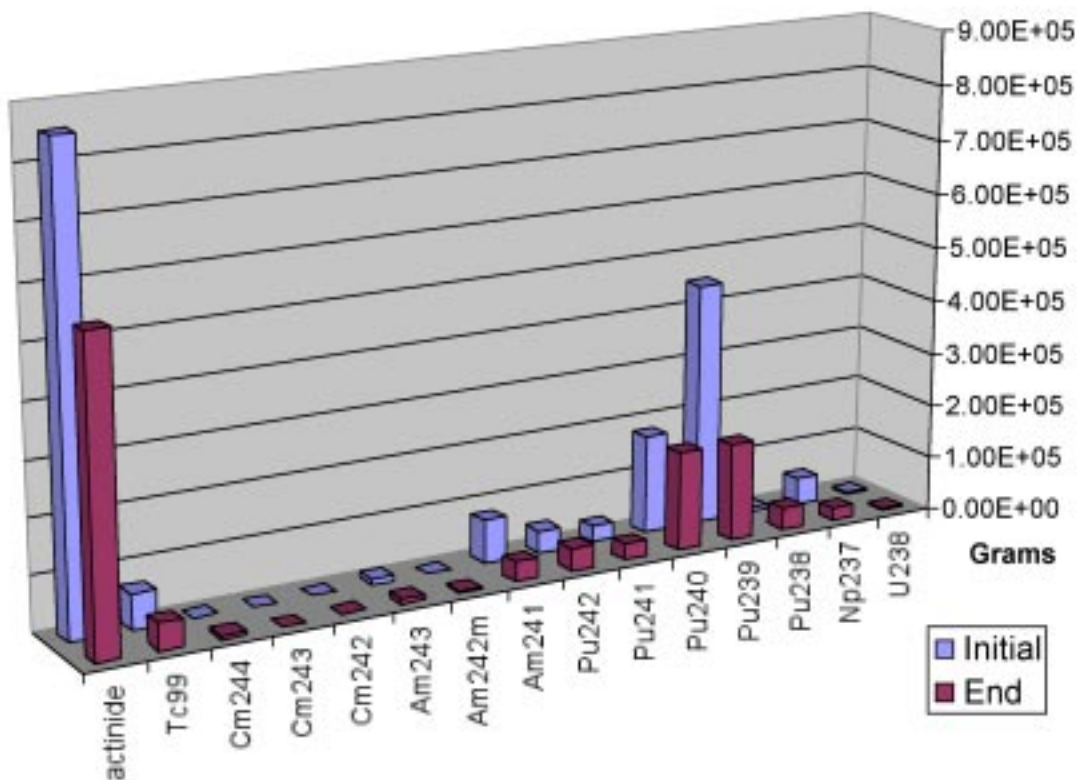
Figure 3-14.   Inventories for Case with No Removal but with Shuffling

3.3.6.3   No Separations or Shuffling

The third case does not involve the complication of shuffling fuel at the end of each cycle. Power flattening is achieved by using two different fuel enrichments, and distributing fresh fuel evenly throughout the blanket at the start of each cycle. As with the previous case, this one assumed a once-through fuel cycle, with similar results: for the established fuel clad fluence limit, the discharge burnup is too low to be of benefit for a once-through cycle. Recycling of the fuel discharged from this blanket is necessary. Actinide inventories for the beginning- and end-of-cycle are shown in Figure 3-15.
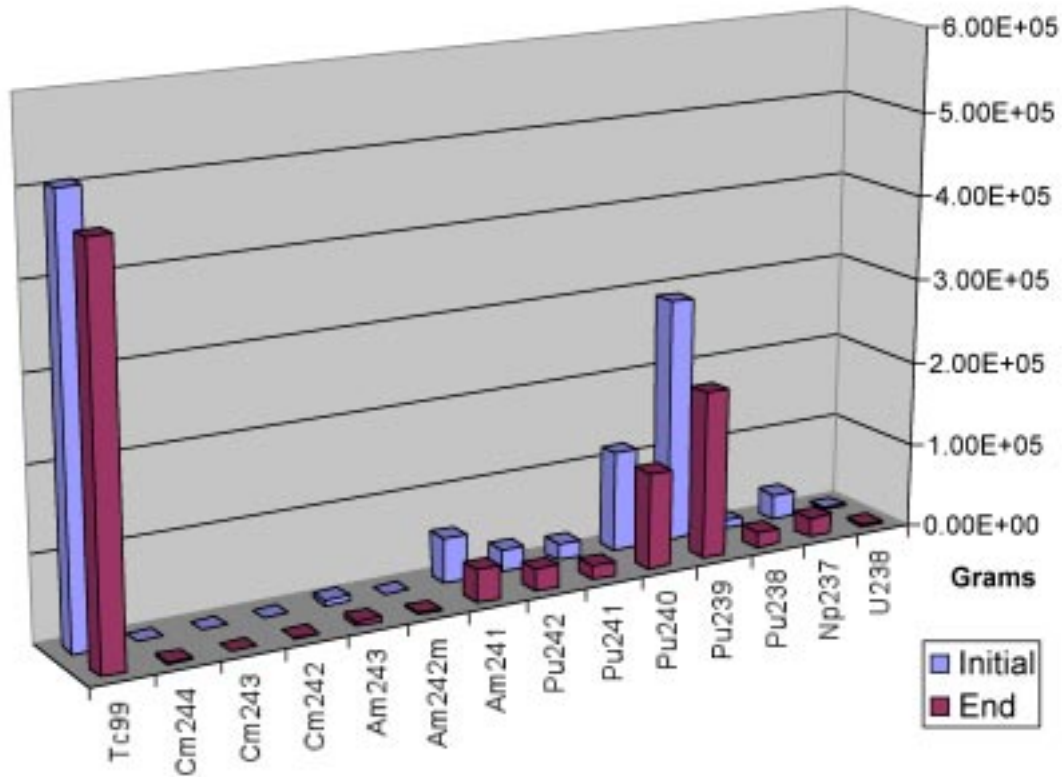
Figure 3-15   Actinide Inventories for No Removal or Shuffling Case

Figure 3-16 compares the actinide burnup rate as a function of fluence for all systems studied up to the imposed fuel clad fluence limit of 4×10^{23} n/cm^2. The case with shuffling appears more efficient in burning actinides than the case without shuffling. This is because shuffling is a bit more effective at flattening the flux profile and distributing neutrons evenly throughout the system. As shown in Figure 3-17, the burn rate of Tc-99 was about the same for each case.
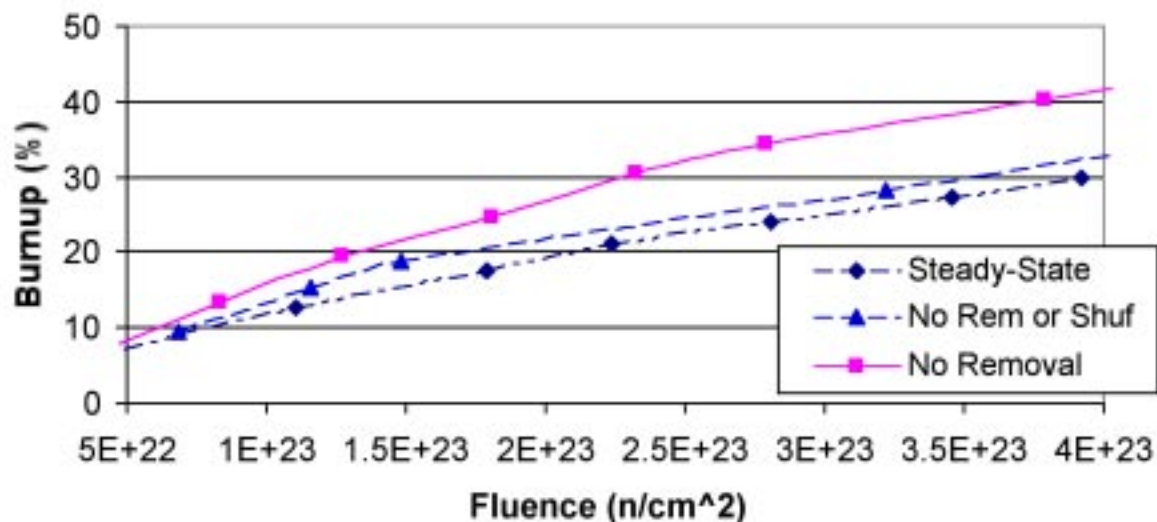
Figure 3-16.   Burnup of Actinides for Three Modes of Operation
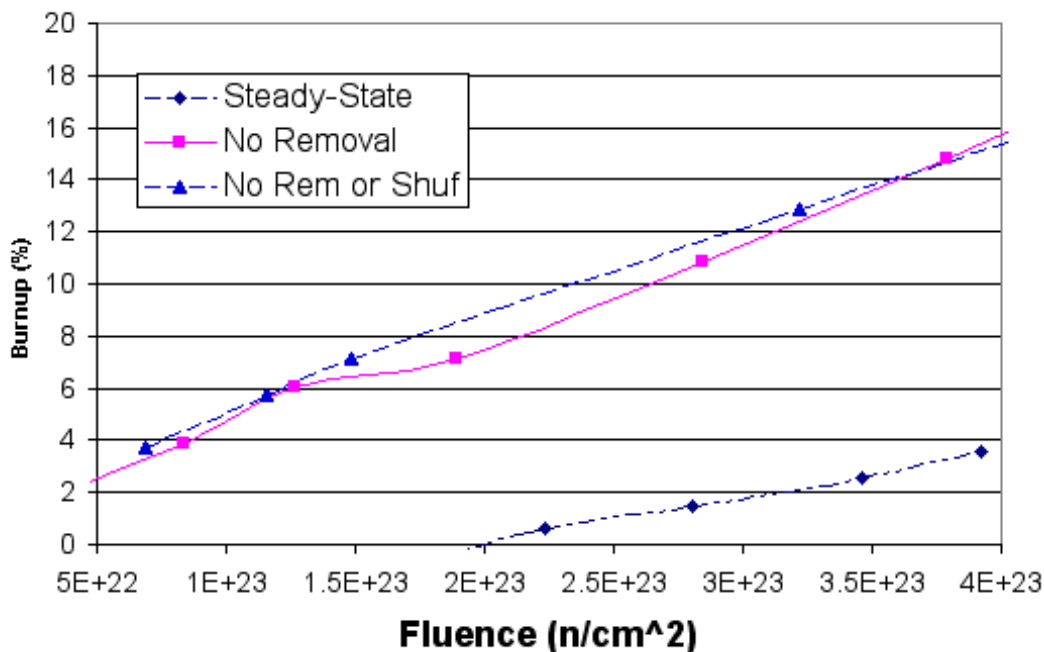
Figure 3-17.   Burnup of Technetium for Three Modes of Operation

3.4 System Point Design Specifications and Performance

This section describes the development of an LBE-cooled blanket point design based on the
results of parametric studies in the previous section. As a first step in specifying this point
design, inhomogeneous source calculations were performed for the preliminary design

described in the previous section. Because the spallation neutron source is concentrated in the target, explicit modeling of the source via inhomogeneous flux calculations yields higher peak fluxes and a higher peak power density than the corresponding eigenvalue calculation. This peaking of the flux and power occurs in an innermost fuel assembly (at a surface facing the target), and it increases over an irradiation cycle because the source intensity required to maintain the constant power level increases. As a result, the peak fast fluence value predicted by the inhomogeneous calculation is considerably higher than that of the eigenvalue solution.

In order to reduce the power peaking factor and the peak fast fluence value, the preliminary design was further refined. The intensity of the inhomogeneous source at the interface between LBE buffer and the innermost fuel assemblies was reduced by extending the buffer region surrounding the central target region from one to two rows of assemblies. The power distribution within the fueled region was further flattened by optimizing the split of the TRU loading among concentric planar zones of blanket. Three different blanket zones differing in the TRU mass fraction of the fuel (i.e., in "enrichment") were employed, and the zone sizes and enrichments were determined such that the peak linear powers of three zones are close to each other. The proposed blanket layout is shown in Figure 3-18; it consists of 19 hexagonal lattice positions containing the LBE target/buffer and 192 fuel assemblies. The blanket is surrounded by two hexagonal rows of steel reflector assemblies and one row of B_4C shield assemblies. The principal design parameters of the proposed design are summarized in Table 3-10. A semiannual 6-batch fuel management scheme is employed with 75% capacity factor. The fuel residence time in the innermost blanket zone was limited to 5 cycles to limit the peak fast fluence value.

Table 3-10. Design Parameters for the Proposed LBE-Cooled Blanket Point Design

Parameter			Value
Proton Energy (GeV)			1.0
Target Material			LBE
Fuel Material			(TRU-10Zr)-Zr
Pin Diameter (cm)			0.635
Cladding Thickness (cm)			0.056
Pitch-to-Diameter Ratio			1.727
Number of Pins per Assembly			217
Fuel Smear Density (%)			75
Volume Fraction (at operating temp.)	Fuel		0.140
	Structure		0.103
	Coolant		0.695
Hexagonal Assembly Pitch (cm)			16.142
Number of Assemblies	LBE target/buffer		19
	Fuel	Inner Zone	42
		Middle Zone	48
		Outer Zone	102
		Total	192
	Reflector		114
	Shield		66
TRU Fraction Split Factor (outer/ middle/ inner zone)			1.45/1.28/1.00
Active Fuel Height (cm)			106.68
Equivalent Fuel Region Diameter (cm)			246.21
Maximum Blanket Diameter (cm)			357.07
Number of Fuel Batches	Inner Zone		5
	Middle and Outer Zones		6
Cycle Irradiation Time (days)			145
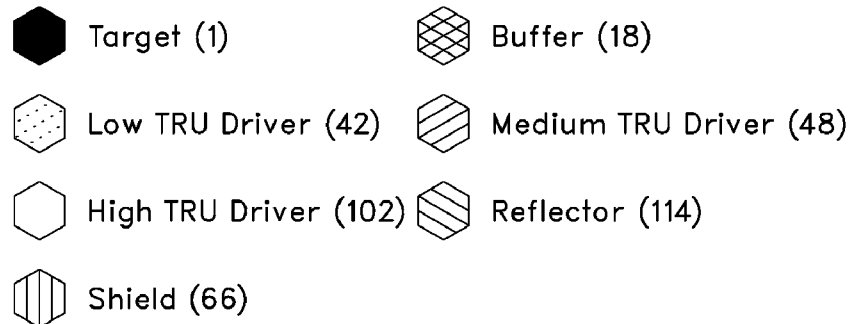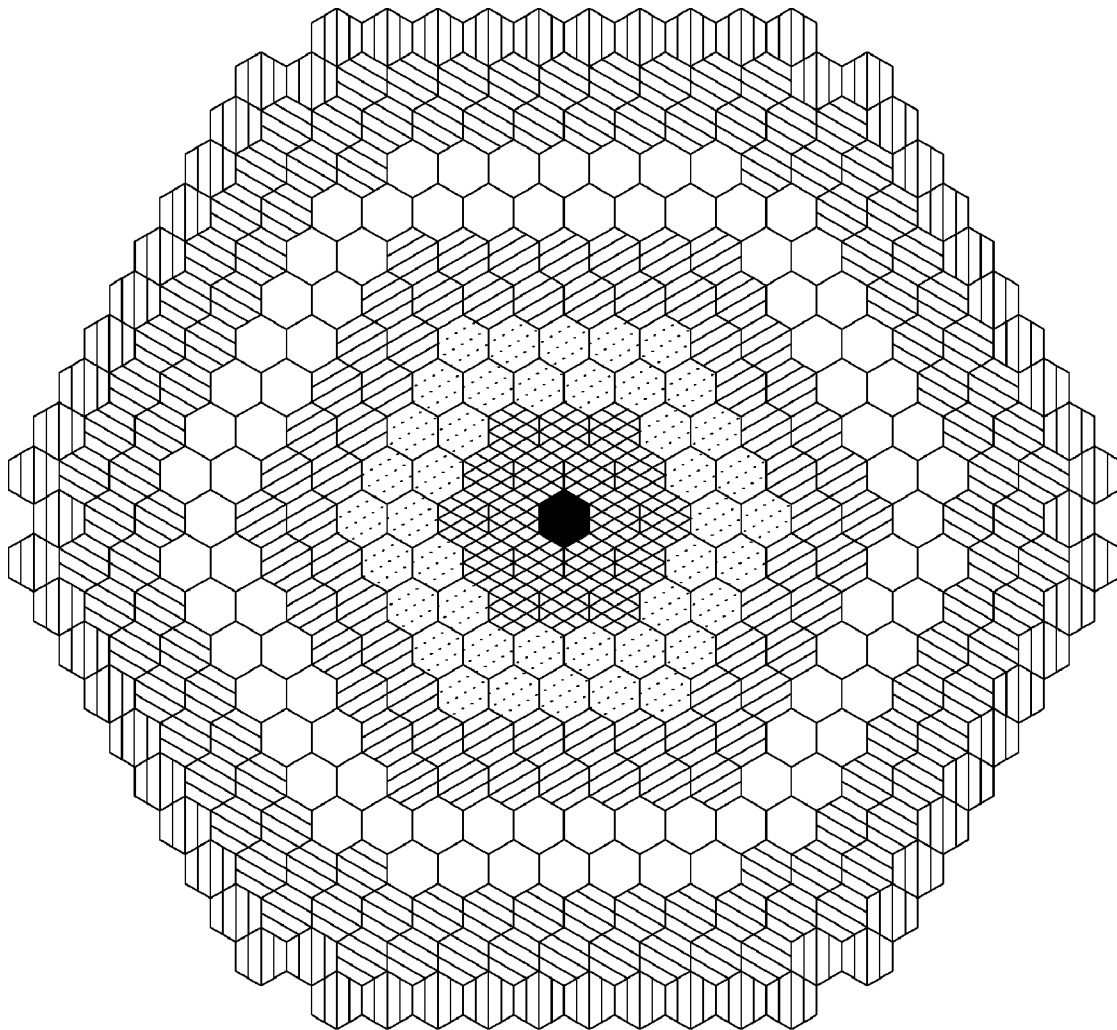
Figure 3-18.   Proposed LBE-Cooled Blanket Configuration (*192 Fuel Assemblies*)

The equilibrium-cycle neutronics performance of the proposed design was analyzed using
the REBUS-3 code. The (inhomogeneous) flux calculations were performed with the

triangular-Z finite difference option of DIF3D using a generic spallation neutron source
distribution generated for a 1-GeV proton beam and a prototypic LBE target [49]. A medium-
burnup (33,000 MWd/MT) PWR assembly with 25-year cooling time was used to specify a
composition of the LWR-discharge feed stream [54]. The isotopic composition of this feed
stream is compared in Table 3-11 with the equilibrium-cycle ATW discharge composition.
The fuel enrichments in each blanket zone were determined according to the enrichment
split factors shown in Table 3-10 such that the k_{eff} at BOEC is 0.97.

**Table 3-11. Isotopic Compositions of the Assumed LWR-Discharge Feed Stream and the LBE
Blanket Heavy Metal Discharge**

Isotope	25-year Cooled PWR TRU (wt%)	ATW-discharge TRU (wt%)
U-234	0.000[a]	0.475
U-235	0.004 [a]	0.121
U-236	0.002 [a]	0.177
U-238	0.478 [a]	0.001
Np237	5.023	1.945
Pu238	1.272	5.133
Pu239	53.196	18.384
Pu240	21.534	37.843
Pu241	3.782	7.674
Pu242	4.686	13.448
Am241	8.967	4.142
Am242m	0.014	0.376
Am243	0.926	4.592
Cm242	0.000	0.440
Cm243	0.002	0.040
Cm244	0.104	3.636
Cm245	0.009	0.962
Cm246	0.001	0.613

[a] It is assumed that 99.995% of the uranium is removed in the UREX process.

Computed equilibrium cycle performance parameters are summarized in Table 3-12. Compared to the performance of the preliminary design results (displayed in Table 3-3), the TRU inventory at BOEC is increased by 9% because of the extended buffer region, the modified enrichment zoning, and the use of a 25-year cooled LWR-discharge feed stream. Consequently, the average discharge burnup and the burnup reactivity loss are reduced slightly. The average discharge burnup is further reduced slightly by the reduced fuel residence time in the inner zone. Despite of these factors, an average discharge burnup of ~26% is achieved with a 3-year fuel residence time. The burnup reactivity loss is 5.7% with the assumed half-year cycle. The highest TRU fraction in the charged fuel (i.e., the outermost zone enrichment) is ~49 weight percent, which is well within the limit of the metallic dispersion fuel. The adopted enrichment zoning results in similar power peaking factors at BOEC (1.43) and EOEC (1.49). At BOEC, the peak linear power (31.0 kW/m) occurs in the outer fuel zone.

Because of the increased spallation source intensity and non-uniform TRU depletion, the peak power location moves to the middle fuel zone (33.0 kW/m) at EOEC. (The peak of the batch-averaged power density at EOEC is highest in the inner blanket zone. However, because of the smaller number of batches used in the inner zone, the stage factor accounting for the higher power density of fresh fuel assemblies is smaller in the inner zone than in the middle zone. Consequently, the peak linear power is higher in the middle zone than in the inner zone.) Note that the resulting peak linear powers in the three blanket zones are very close to each other as desired, and that they are within the limiting value of 33 kW/m. The peak fast fluence value of 3.73×10^{23} n/cm^2 occurs in the middle blanket zone, which is within the imposed fluence limit of 4×10^{23} n/cm^2.

Table 3-12. Performance Characteristics of the Proposed LBE-Cooled Blanket Point Design

TRU fraction in fuel (weight%)	Inner zone	37.4
	Middle zone	45.1
	Outer zone	49.3
Multiplication Factor	BOEC	0.9704
	EOEC	0.9130
Burnup reactivity loss (%Δk)		5.7
Core-average power density (kW/ℓ)		166.0
Power peaking factor	BOEC	1.43
	EOEC	1.49
Peak linear power (kW/m)	Inner zone	32.6 (at EOEC)
	Middle zone	33.0 (at EOEC)
	Outer zone	31.0 (at BOEC)
Discharge burnup (atom%)	Average	26.1
	Peak	38.3
Peak fast fluence (10^{23} n/cm^2)	Inner zone	3.53
	Middle zone	3.73
	Outer zone	3.08
Net TRU consumption rate (kg/year)		237
Equilibrium loading (kg/year)	LWR TRU	237
	Recycled TRU	668
	Total TRU	905
Heavy metal inventory (kg)	BOEC	2464
	EOEC	2338

3.5 Issues

The parametric studies leading to the proposed SPD have defined the characteristics of an LBE-cooled transmutation blanket that enables efficient consumption of LWR discharge TRU. The key system objective of high ATW fuel discharge burnup (to minimize the number of successive recycle stages and associated TRU losses) was shown to be achievable in a configuration with comparatively high power density (enabling small system size and potentially favorable economics) and relatively low burnup reactivity loss (to reduce requirements for reactivity and/or source control). System design and operating characteristics that satisfy these goals while meeting key thermal-hydraulic and materials-related design constraints were preliminarily developed. Perhaps more significantly, a systematic approach was devised for meeting these key objectives subject to the assumed constraints. This approach should greatly facilitate future efforts to optimize the system's performance, e.g., for updated values of the constraining variables or taking a broader set of performance objectives into consideration.

Two key assumptions made in developing the proposed point design are the power level of the transmutation system (840 MWth) and its minimum subcriticality level (k_{eff} = 0.97 at the start of cycle); both parameters strongly affect system characteristics and directly impact the accelerator beam power required per transmuter. The choice of transmuter (fission) power level is based largely on the recent design experience with the PRISM ALMR, which indicates that favorable economics and safety performance can be achieved with the 840 MWth system size. The applicability of this experience to the LBE-cooled ATW transmuter should be examined in future studies. With respect to degree of subcriticality, the assumed level is believed to be a good compromise between the competing objectives of minimizing accelerator power (favors high k_{eff}) and precluding the potential for criticality as a result of operational or accidental reactivity insertions (favors low k_{eff}). However, explicit dynamic and safety analyses will be required to optimize the choice of subcriticality level.

Future evaluations of system dynamic behavior and safety characteristics must be performed in conjunction with (a) development of the heat transport system NSSS, (b) design of the LBE spallation target and accelerator beam delivery system, and (c) development of the system control strategy. Key design objectives will be to incorporate passive safety features and to assure that the thermal stresses resulting from planned and unplanned accelerator beam interruptions do not excessively limit the lifetime of transmuter structures and components. These system development efforts and supporting dynamic analyses are currently at an early stage.

With respect to transmutation performance, the current study has focused on the equilibrium-cycle mass flows, assuming that TRU losses during recycle are negligible. Future studies are needed to assess the impact of non-zero TRU losses on the fuel cycle mass flows in general (including fuel composition effects) and the waste streams in particular. Moreover, a blanket management/control strategy should be developed for accommodating with the evolution of fuel composition (and reactivity) during the transition to the equilibrium, as well as for variations in the LWR feedstock composition and other deviations from the equilibrium conditions.

Significant R&D efforts will be required to confirm the feasibility of two key elements of the LBE SPD—adoption of LBE as target and coolant material and use of non-uranium fuels. These R&D requirements are discussed elsewhere [11, 17]. Related issues requiring attention in the Systems area include the activation of LBE coolant and the buildup of spallation products in the LBE target. These assessments should be conducted as part of a larger effort to characterize the waste generation for the entire ATW system—both during operation and in the stage of facility decontamination and decommissioning.

References

30. "A Roadmap for Developing Accelerator Transmutation of Waste (ATW) Technology—A Report to Congress," DOE/RW-0519, October 1999.

31. B. F. Gromov, *et al*., "Nuclear Power Plants with the Lead-Bismuth Coolant," *Atomic Energy,* 81, p. 340, 1996.

32. C. Williams and R. T. Schomer, "Liquid Metal Fuel Reactor and LMFRE-I, Proceedings of the 2nd UN International Conference On Peaceful Uses of Atomic Energy, Vol. 10, p. 487, UN, Geneva, 1958 (P/2355).

33. D. J. Hill, *et al*., "A Roadmap for Developing ATW Technology: Systems Scenarios and Integration," Argonne National Laboratory Report ANL/RE-99/16, September 1999.

34. F. Venneri, *et al*., "Roadmap for the Development of Accelerator Transmutation of Waste: Target and Blanket System," Los Alamos National Laboratory Report LA-UR-99-3022, September 1999.

35. B. W. Spencer, *et al*., "The Rush to Heavy Liquid Metal Reactor Coolants—Gimmick or Reasoned," ICONE-8729, *Proceedings of 8th International Conference on Nuclear Engineering (ICONE 8)*, Baltimore, MD, April 2000.

36. R. N. Hill, *et al*., "Physics Studies of Weapons Plutonium Disposition in the Integral Fast Reactor Closed Fuel Cycle," *Nuclear Science and Engineering*, 121, 17-31, 1995.

37. E. L. Gluecker, "U.S. Advanced Liquid Metal Reactor (ALMR)." *Progress in Nuclear Energy*, 31, 43-62, 1997.

38. R. D. Legett and L. C. Walters, "Status of LMR Fuel Development in the United States," *J. Nuclear Materials*, 204, 23-32, 1993.

39. M. Salvatores, I. Slessarev, A. Tchistiakov, and G. Ritter, "The Potential of Accelerator-Driven Systems for Transmutation or Power Production Using Thorium or Uranium Fuel Cycles," *Nucl. Sci. Eng.*, 126, 333, 1997.

References (continued)

40. P. A. Fomitchenko, "Physics of Lead-Cooled Reactors," Proceedings of the 1998 Frédéric Joliot Summer School in Reactor Physics, *Cadarache*, France, August 17-26, 1998.

41. D. C. Crawford, *et al*., "Accelerator Transmutation of Waste: Fuel Development Plan for FY'01 through FY'05, June 29, 2000 (draft).

42. B. J. Toppel, "A User's Guide to the REBUS-3 Fuel Cycle Analysis Capability," ANL-83-2, Argonne National Laboratory, 1983.

43. W. S. Yang and H. S. Khalil, "Analysis of the ATW Fuel Cycle Using the REBUS-3 Code System," *Trans. Am. Nucl. Soc.*, 81, 277, 1999.

44. K. L. Derstine, "DIF3D: A Code to Solve One-, Two-, and Three-Dimensional Finite-Difference Diffusion Theory Problems," ANL-82-64, Argonne National Laboratory, 1984.

45. R. D. Lawrence, "The DIF3D Nodal Neutronics Option for Two- and Three-Dimensional Diffusion Theory Calculations in Hexagonal Geometry," ANL-83-1, Argonne National Laboratory, 1983.

46. G. Palmiotti, E. E. Lewis, and C. B. Carrico, "VARIANT: Variational Anisotropic Nodal Transport for Multidimensional Cartesian and Hexagonal Geometry Calculation," ANL-95/40, Argonne National Laboratory, 1995.

47. H. Henryson II, B. J. Toppel, and C. G. Stenberg, "MC2-2: A Code to Calculate Fast Neutron Spectra and Multigroup Cross Sections," ANL-8144, Argonne National Laboratory, 1976.

48. W. M. Stacey, Jr., *et al*. "A New Space-Dependent Fast-Neutron Multigroup Cross-Section Preparation Capability," *Trans. Am. Nucl. Soc.*, 15, 292, 1972.

49. B. C. Na, P. Wydler, and H. Takano, "OECD/NEA Comparison Calculations for an Accelerator-Driven Minor Actinide Burner: Analysis of Preliminary Results," Second Workshop on Utilization and Reliability of High Power Proton Accelerators, OECD Nuclear Energy Agency, Aix-en-Provence, France, November 22-24, 1999.

50. D. I. Poston and H. R. Trellue, "User's Manual, Version 2.0 for Monteburns, Version 1.0," Los Alamos National Laboratory Report LA-UR-99-4999, September 1, 1999.

51. M. J. Bell, "ORIGEN—The ORNL Isotope Generation and Depletion Code," ORNL-4628, Oak Ridge National Laboratory, 1973.

References (continued)

52. R. N. Blomquist, "VIM—A Continuous Energy Monte Carlo Code at ANL," A Review of
the Theory and Application of Monte Carlo Code Methods, Proceedings of a Seminar-
Workshop, ORNL/RSIC-44, April 1980.

53. J. Laidler, private communication, March 23, 2000.

54. R. N. Hill, "LWR Feed Inventory Specification for ATW System Studies," Argonne
National Laboratory Intra-Laboratory Memo to H. Khalil, June 12, 2000.

4 Gas-Cooled System

4.1 Introduction

General Atomics (GA) has proposed [55] using an ATW concept based on a variant of the GT-MHR. This section summarizes the evaluation of that concept which was performed jointly by ANL and LANL teams, describes two proposed point designs and lists the major issues which need to be addressed during further phases of the ATW Roadmap implementation.

- Section 4.2 provides a general description of the system proposed by GA.

- Section 4.3 describes the major design parameters (degrees of freedom) that can be altered to optimize the system design, and also lists the constraints that guide the design and optimization studies.

- Section 4.4 describes the codes and the models used for the neutronics evaluation, and provides the main parameters of the proposed system.

- Section 4.5 provides an overview of the parametric studies which have been performed at the fuel block level to understand the major neutronic trade-offs related to basic design parameters.

- Section 4.6 extends these studies to analyze the effect of various fuel management schemes.

- Section 4.7 describes two possible system point designs, and compares their performances.

- Section 4.8 discusses the major issues that need to be addressed during further studies.

4.2 System Description

Figure 4-1 and Figure 4-2 provide a general description of the system proposed by GA [55]. The transmuter consists of a steel vessel housing, containing an annular transmutation region operating in a thermal neutron spectrum. This annular region contains the "fresh" TRU separated from the LWR spent fuel. The TRU is contained in TRISO-coated particles. These spherical particles consist of a 200μm-diameter TRUO$_{1.7}$ core surrounded by layers of graphite buffer (thickness: 100μm) to absorb gaseous fission products, pyrolitic graphite (thickness 35μm), silicon carbide (thickness 35μm) to serve as a stable barrier and pressure vessel, and an outside layer of pyrolitic graphite (thickness: 40μm). These particles are mixed with graphite powder and packed into cylindrical compacts. The compacts are loaded into cylindrical channels within hexagonal graphite blocks, as described in Figure 4-3. The blocks also have channels for helium coolant flow and channels for introducing erbium

burnable poison into the system. The blocks are 36 cm flat-to-flat, and contain 202 fuel channels, 108 coolant channels and 14 burnable poison channels, all arranged on a 1.88-cm triangular pitch. Fuel blocks are loaded into the fifth, sixth, and seventh radial rings of a hexagonal core (see Figure 4-2). Three rings of graphite reflector are arranged both inside and outside of this thermal region. The innermost layer is filled with fast fuel assemblies, composed of the TRU material that has undergone four years of burning in the thermal region. The core comprises ten active blocks stacked vertically. The fast assemblies have not yet been designed, and for the purpose of this study it is assumed that they are similar to the Gas-Cooled Fast Reactor (GCFR) design developed in the 70's and early 80's. At the center of the core is the location for a spallation target used during the period of subcritical operation.

The transmuter operates in the critical mode for approximately three years, which corresponds to 75% of its cycle length. In this mode, the critical thermal region drives the fission process and limited transmutation events are expected in the fast region. After these three years, the thermal region becomes subcritical and is driven by the spallation target during a fourth year. The local multiplication of spallation neutrons in the fast region might produce a significant fast flux thus helping the transmutation of the minor actinides. The plant would comprise four 600MWth transmuters, sharing one 15MW-beam accelerator.

Preliminary analyses by GA [55] indicate that this design will achieve deep levels of transmutation without requiring reprocessing, thanks to the encapsulation of the materials to be transmuted in the ceramic-coated microspheres.

The system is cooled by helium heated to an outlet temperature of 850°C. Helium is carried to a direct-cycle gas-turbine-generator system. The high operating temperatures and the characteristics of the direct Brayton power conversion system allow electric generation with a high net thermal efficiency of approximately 47%.

Fast Region

Thermal Region

Proton Beam

**Connection to
Power Conversion System**

**Transmutation:
MA
Tc, I**
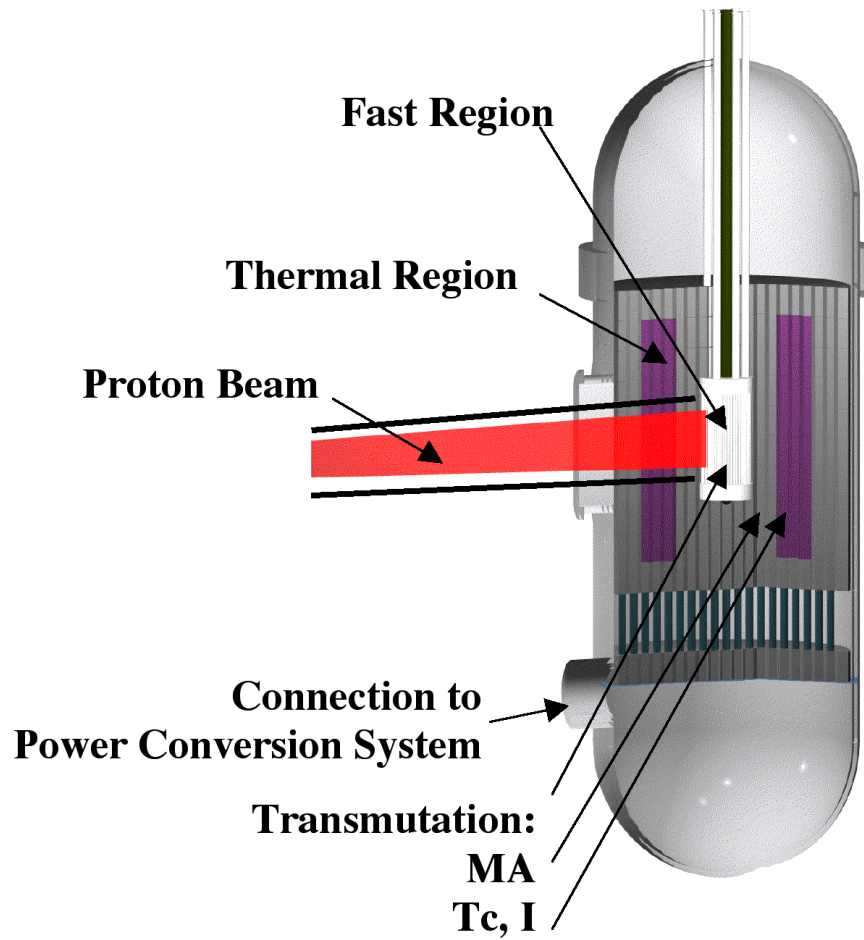
Figure 4-1.   Thermal-Fast Transmuter
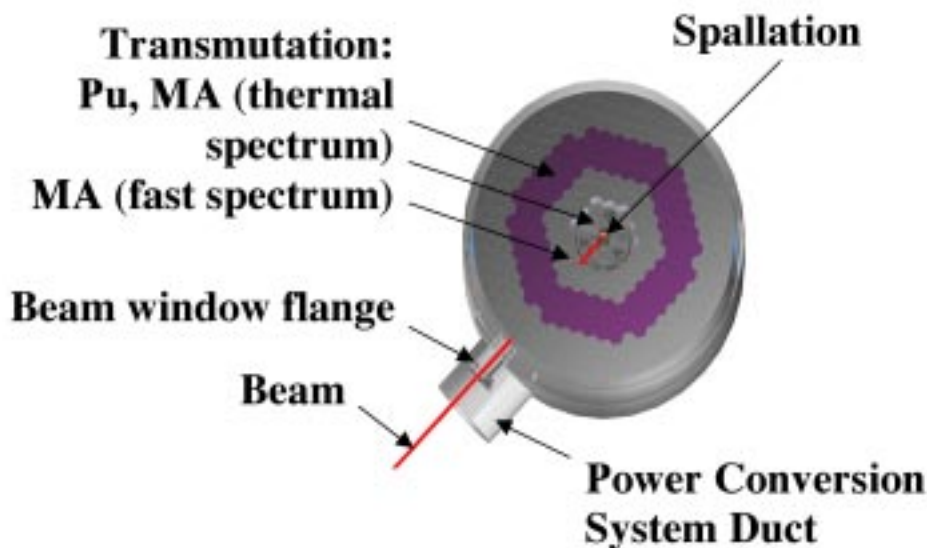
Figure 4-2.   Thermal-Fast Transmuter Cross Section

4.3 Objectives, Constraints, and Degrees of Freedom

The objectives of the system design activities are three:

3. Achieve very high burnup of the initial loading of Plutonium and Minor Actinides;

4. Maintain fuel particle integrity throughout the fuel cycle and into disposal, thus avoiding the need for intermediate reprocessing;

5. Maintain high operating temperatures needed to achieve a high net thermal efficiency.

Several constraints need to be taken into account:

• Fuel performance: this issue is addressed in Section 4.8. It should be noted that the very high burnup levels considered for this system are beyond the limits of the available experimental database.

• Safety: safety must be guaranteed at all times, in particular during critical operation. The fuel contains relatively little resonant absorbers, as compared to traditional LWR fuel. Thus, the fast acting Doppler coefficient might become quite small; the addition of erbium burnable poison might help create a moderator temperature effect, but this might also be offset by the creation of strong thermal absorbers during burnup.

• Coolability: fuel materials must remain within their nominal temperature ranges during both subcritical and critical stages. While the case of the MHR has been well studied, several new features of the system might make it more difficult to cool; the very deep expected burnup might create very large power peaks in the thermal region; the

subcritical operation might create very large power peaks in the fast region; the design of
the fast region will need to be considered with care to achieve coolability at all times,
including safety transients.

- Controllability: the very high objective burnup limits might imply significant changes in
  fissile material inventory during operations if a simple fuel management system is used.
  This might imply significant reactivity changes from beginning to end of cycle, and the
  need to control it through control rods, burnable poisons, and accelerator power grading.
  As much as possible, it is desirable to reduce the reactivity changes during operations.

- Cycle lengths: it is usually desirable to achieve long cycle lengths, in order to reduce the
  plant down time. Furthermore, it might be desirable to increase the critical cycle length
  and decrease the subcritical cycle length, in order to reduce the accelerator
  requirements.

For the purpose of the present study, it was decided to limit the degrees of freedom
available to the designers; while in the future it might become of interest to allow for
significant flexibility in the design parameters, the current study remains relatively close to
the design database developed by GA over the past decades of work. The following
parameters were fixed:
- Fuel block geometry as described in Figure 4-3
- Core and reactor overall dimensions as described in Figure 4-1 and Figure 4-2
- Core power level (600 MWth) and operating temperatures, as described by GA [55]

Nevertheless, the effect of several other design parameters on the system performance was
studied:

- The initial heavy metal loading is expected to have an effect on initial reactivity, cycle
  length, temperature coefficient, and achievable burnup;

- The initial burnable poison (erbium) loading is also expected to have an effect on initial
  reactivity, cycle length, temperature coefficient, and achievable burnup;

- The particle (fuel and erbium) dimensions are expected to have an effect on initial
  reactivity, cycle length, temperature coefficient, and achievable burnup;

- The core loading pattern (number of fueled blocks) is expected to have an effect on
  initial reactivity, cycle length, temperature coefficient, and achievable burnup;

- The fuel management scheme is expected to have an effect on initial reactivity, cycle
  length, temperature coefficient, and achievable burnup.

The effect of these degrees of freedom on fuel assembly neutronics and core neutronics are
described in Sections 4.4 through 4.6.
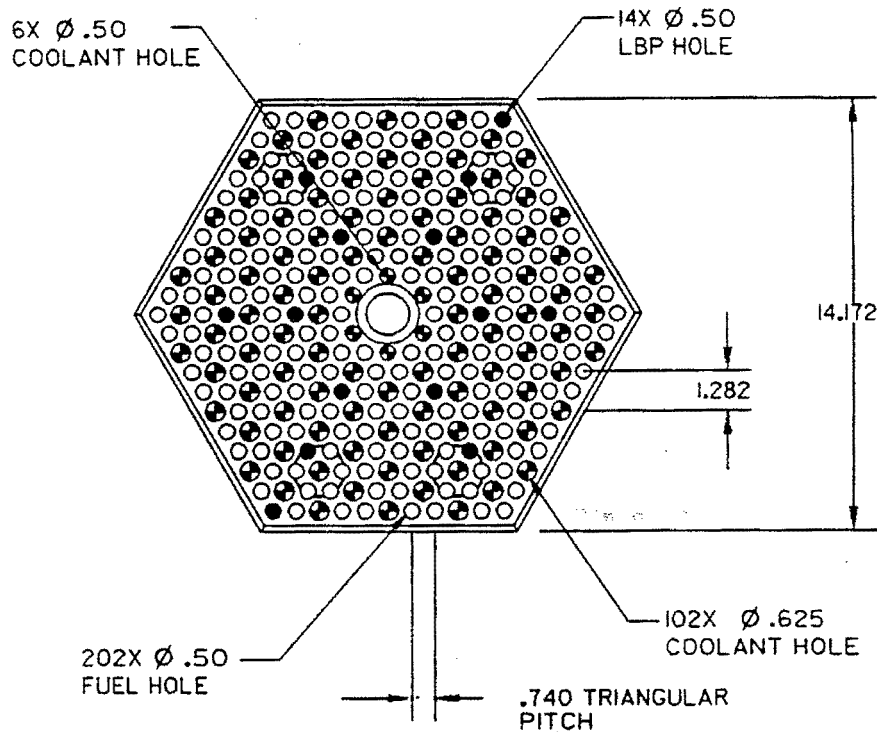
Figure 4-3.   Cross-Sectional View of the Thermal Assembly (*Dimensions in inches*)

4.4 Codes and Models Used for Neutronics Calculations

Two complementary computational paths have been implemented for the GT/AD-MHR (Gas
Turbine/Accelerator-Driven Modular Helium Reactor) studies:

- A deterministic path based on DRAGON/DIF3D/REBUS codes has been developed at
  ANL. While it promises fast running times and allows for multiple perturbation
  calculations, it relies on a series of energetic and spatial homogenization steps which
  might decrease its accuracy. Thus, it needs to be carefully validated. Therefore, an
  independent stochastic path based on MONK [56] has been utilized to validate the
  predictions of the deterministic path and to provide a reference database. A validation
  report will be issued to document the validation results and to provide a reference
  database for future work.

- A stochastic path, based on MCNP-X, MCNP, and Monteburns has been implemented
  at LANL. This path promises high computational accuracy, at the cost of long running
  times.

4.4.1 ANL Path

The GT/AD-MHR design includes several levels of heterogeneity effects that require proper
treatment in order to obtain accurate physics predictions for the core. The fuel elements are

hexagonal prismatic blocks of graphite containing parallel vertical holes, arranged in a triangular pitch, into which fuel or burnable poison (BP) compacts are loaded or which are vacant to serve as coolant flow paths. Other holes are utilized for control rods and fuel loading devices, but have not been modeled in this study. The fuel and BP compacts comprise of multi-layer ceramic-coated particles dispersed in a graphite matrix. Significant neutronic heterogeneities are created by these small particles. Fuel element heterogeneity arising from the heterogeneous arrangement of fuel, BP and coolant channels in the element, also exists in this design. Core heterogeneity is also present because of the annular core layout that employs inner and outer reflector zones and the fueled fast and thermal core zones. Data are presented in Table 4-1.

Table 4-1. GT/MHR Core Parameters

Parameter	Value
Fuel Kernel Properties	
Form, Density	$TRUO_{1.7}$, 10.2 g/cc
Diameter	200 mm
Fuel Particle Coating Properties	
Buffer, Density	100 mm, 1.0 g/cc
Inner Dense PyC, Density	35 mm, 1.87 g/cc
SiC, Density	35 mm, 3.2 g/cc
Outer Dense PyC	40 mm, 1.83 g/cc
Particle Diameter	620 mm
Erbium Kernel Properties	
Form, Density	Er_2O_3, 8.64 g/cc
Diameter	400 mm
Erbium Particle Coating Properties	
Buffer, Density	100 mm, 1.0 g/cc
Inner Dense PyC, Density	35 mm, 1.87 g/cc
SiC, Density	35 mm, 3.2 g/cc
Outer Dense PyC	40 mm, 1.83 g/cc
Particle Diameter	820 mm
Fuel Heavy Metal Composition	
Np-237	4.10%
Pu-238	1.20%
Pu-239	51.55%
Pu-240	23.88%
Pu-241	7.99%

Pu-242	5.00%
Am-241	5.00%
Am-242m	0.10%
Am-243	1.00%
Cm-242	0.00%
Cm-243	0.00%
Cm-244	0.20%
Cm-245	0.00%
Core Temperatures	
Average Thermal Assembly Fuel Temperature	770 ^{o}C
Temperature Operating Range	580 ^{o}C to 1250°C
Average Graphite Temperature	700 ^{o}C
Average Fast Assembly Fuel Temperature	770 ^{o}C
Thermal Assembly Fuel Element Data	
Fuel Element Pitch (includes gaps)	36.1 cm
Fuel Element Height	79.3 cm
Graphite Block Density	1.74 g/cc
Number of Fuel and BP Holes	216
Hole Diameter	1.27 cm
Compact Diameter	1.2446 cm
Coolant Holes	
Number of Inner/Outer Holes	6/102
Diameter Inner/Outer Holes	1.27/1.5875 cm

The core heterogeneities have been evaluated using Monte Carlo and deterministic models. The Monte Carlo model is based on the MONK code, which employs JEF2.2 nuclear data library. A deterministic scheme based on the DRAGON [57] lattice code, the ENDF/B-VI nuclear data library, and the DIF3D/REBUS3 [58, 59] suite of core analysis codes has also been developed. Most of the design evaluations are currently being performed with the deterministic codes because of the fast running time of these codes relative to the Monte Carlo codes. In order to verify the accuracy of the deterministic code predictions, the results of homogeneous-cell, compact-cell, fuel-lattice, and whole-core configurations performed with these codes have been compared to those obtained with the MONK code or other deterministic codes. More effort is required to validate the burnup results.

4.4.1.1 Lattice Model

Burnup-dependent, assembly-average microscopic cross-sections were obtained using the DRAGON lattice code, using ENDF/B-VI based 69-group library; a 172-group library that could be used with DRAGON is also available at ANL. The DRAGON code was selected because it handles accurately the dispersion fuel in a graphite matrix design of the GT/MHR block and permits full-block calculations using the collision probability method. Resonance self-shielding and depletion calculations in the particles are possible because DRAGON allows explicit representations of the multi-layer fuel and BP particles, the matrix graphite and the block graphite of the GT-MHR design.

The need to provide such an explicit model for the fuel block was assessed using the MONK code. MONK has the capability to explicitly model the geometry under consideration and to perform criticality and burnup analyses in an integrated manner. The particles are modeled as a hexagonally close-packed lattice of spheres. The lattice forms a regular octahedron and is cut by a cylinder to represent the compact. MONK criticality calculation can be performed with quasi-continuous energy or multigroup data sets. The quasi-continuous energy data set is processed in a fine-energy mesh (13193 or 8220 groups). The multigroup libraries are processed in a much coarser set (172 or 69 groups). The burnup analyses only use the coarser data sets. The nuclear data libraries are based on JEF version 2.2. Three different models for representing the fuel or burnable poison compacts in the fuel block were evaluated. These are:

- Explicit modeling of the assembly including the multi-layer fuel and the burnable poison particles inside the compacts as shown in Figure 4-4 through Figure 4-6.

- Assembly model using a homogeneous mix of the particle layers inside the compact (homogeneous particles).

- Assembly model employing a homogeneous mix of particle layers and matrix graphite (homogeneous compact).
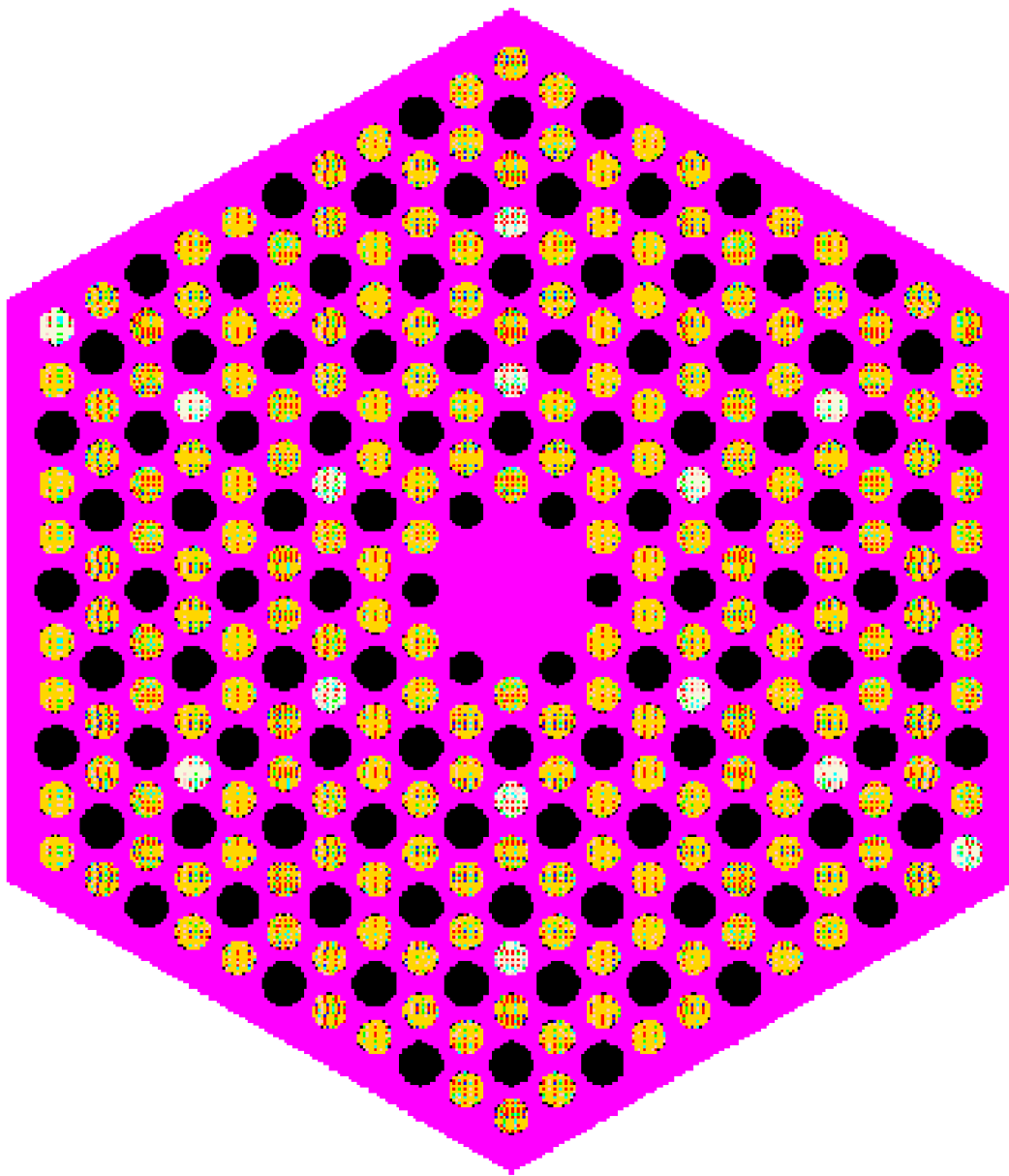
Figure 4-4.   Thermal Assembly Model
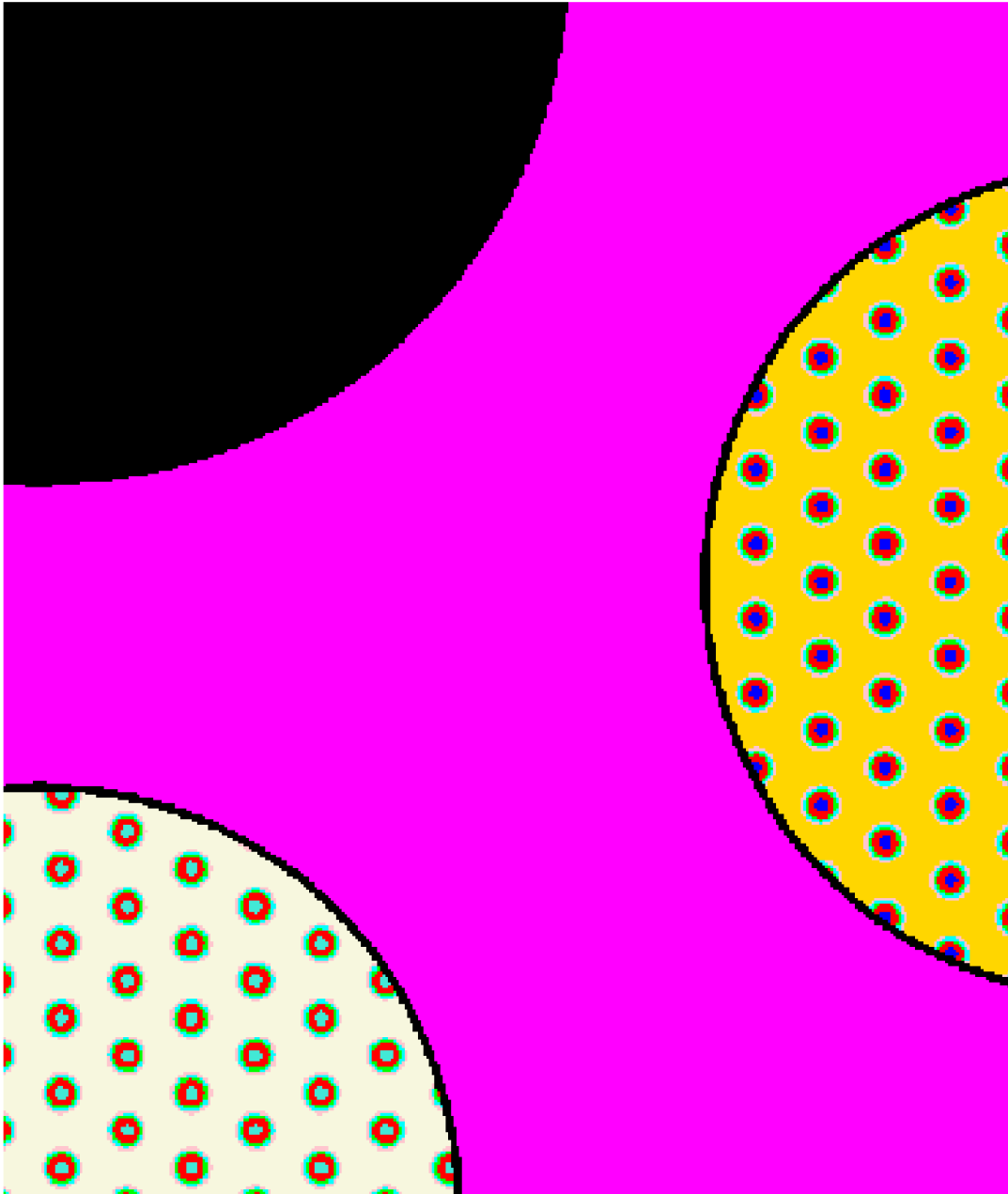
Figure 4-5. **Enlarged Assembly Section Featuring a Section of the Coolant Channel** *(top left)***, Fuel Compact** *(right)***, and Burnable Poison Compact** *(bottom left)*
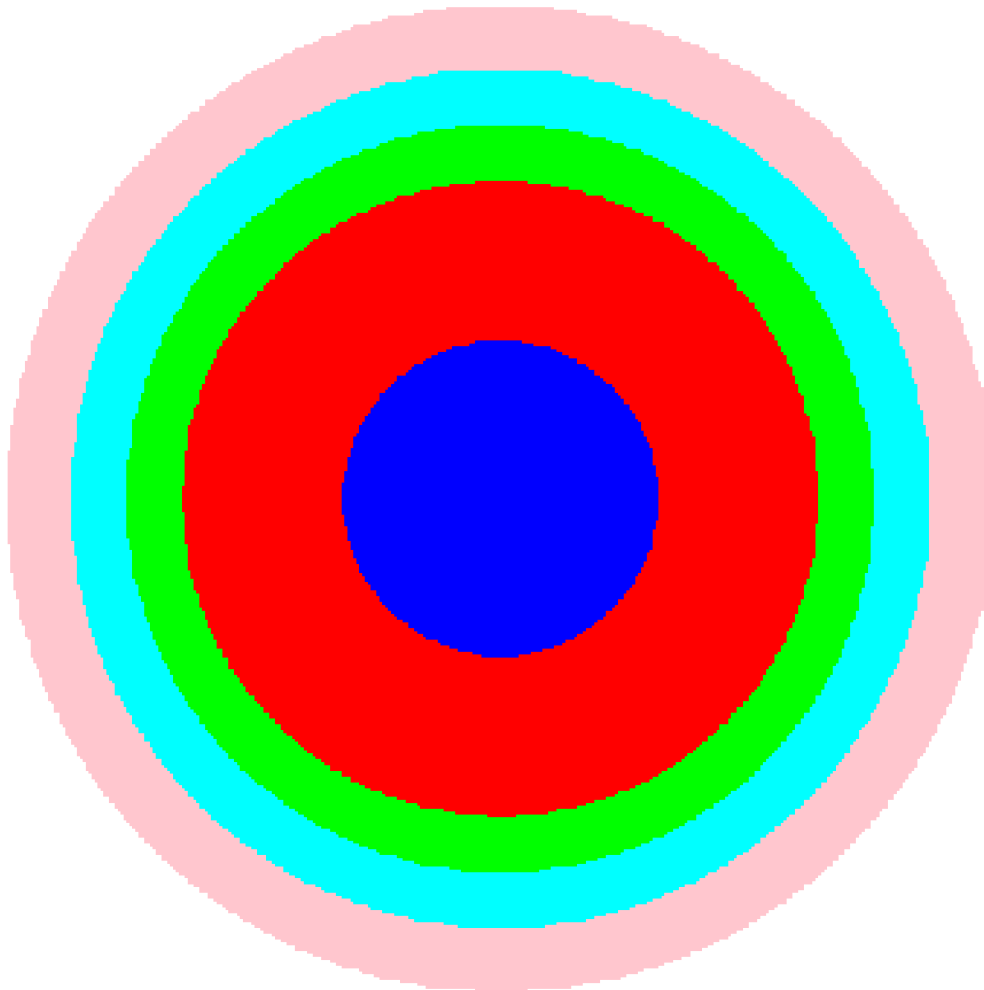
Figure 4-6. Fuel Particle Model

The difference in the k_∞ of the thermal assembly, between the first and either of the two cases provide an estimate of the heterogeneity effect due to the particles in the compact. Table 4-2 summarizes the MONK results using the quasi-continuous energy nuclear data library (13193 groups) for a case employing a heavy-metal loading of 771 grams per assembly. In this MONK analysis, it was assumed that the fuel block is loaded with fuel compacts and helium coolant channels, without erbium poison compacts and without the fuel-handling hole. The MONK results show a strong heterogeneity effect. Similar results were also obtained from DRAGON models for the same configurations as shown in Table 4-2.

Table 4-2.   Fuel Compact Heterogeneity Effect

Fuel Model	Computer Code			
	MONK		DRAGON	
	k_∞	$\Delta k_\infty/k_\infty$(%)	k_∞	$\Delta k_\infty/k_\infty$(%)
Explicit Modeling	1.2764	—	1.2539	—
Homogenized Particles	1.1101	-13.02	—	—
Homogenized Compact	1.0928	-14.38	1.0778	-14.05

The detailed assembly model shown in Figure 4-3 is used to study the burnable poison heterogeneity effect. The volume packing fractions for the fuel and the burnable poison particles are 0.1238 and 0.1, respectively. The MONK code with the quasi-continuous energy nuclear library (13193 groups) based on JEF2.2 was used for the analysis. Similar to the fuel analysis, three cases were analyzed for the burnable poison. The particle homogenization under predicts k_∞ by about 1.8% relative to the explicit modeling as shown in Table 4-3. The homogenized compact increases the difference to -2.2%. These results show the same trend observed in the fuel heterogeneity analysis. In this case, the self-shielding change caused by the erbium absorption resonance explains the change in k_∞ of the assembly. The burnable poison heterogeneity effect is smaller than the corresponding value for the fuel because the assembly has only 14 burnable poison compacts relative to 202 fuel compacts.

Table 4-3.   MONK Burnable Poison Heterogeneity Effect

Burnable Poison Model	k_∞	$\Delta k_\infty/k_\infty$ (%)
Explicit Modeling	1.1864	
Homogenized Particles	1.1649	-1.81
Homogenized Compact	1.1604	-2.19

The homogeneous models (without additional homogenization techniques) give inaccurate k_∞'s because they significantly under-predict the self-shielding of the strong absorption resonances in the plutonium isotopes (particularly Pu-240) and Er-167 in the BP. This is caused by the fact that the fuel or the BP particle dimension is relatively large compared to the mean free path of neutrons in the low-energy-lying resonances of these isotopes. Because of this effect, the inner zone of the particle is shielded from neutrons by the outer zone and simple homogenization of cross sections does not account correctly for the self-shielding effect. For both the fuel and BP compact cases, the heterogeneity effect was found to be dependent on the particle composition and the packing fraction. The difference in k_∞ between the homogeneous and explicit models decreases as the packing fraction increases or as the fuel radii decreases.

Thermal fuel assembly power distributions predicted by MONK and DRAGON have also been compared. The comparison for a thermal fuel assembly containing 14 BP compacts at the cold state (293°K) indicated that DRAGON accurately predicts the power distribution in the assembly. The difference in the maximum compact power predicted by the codes is about 1.1%. The maximum power in this case occurs in a fuel compact located close to the assembly boundary because of the extra (non-cell) graphite present in this zone, which causes a softer neutron spectrum. The maximum compact power difference is about 2.9% and occurs for a compact operating close to the average block power and also neighboring a coolant channel at the inner compact ring in the assembly.

In summary, the DRAGON and the MONK codes give consistent results on a series of calculations from simple compact cells to full assembly analyses. These results provide confidence in the validity of the deterministic calculations, with respect to a high-fidelity method. The strong double heterogeneity effects observed for the fuel and erbium particles imply that a detailed modeling of these particles will be required in calculations.

The depletion model for the GT-MHR compact-cell (fuel compact and surrounding graphite) cases has been verified by comparing results from DRAGON to those obtained with the WIMS8 deterministic code. The compact-cell calculations were done primarily to check the performance of DRAGON compared to another deterministic code, which also employs a different base cross-section library (JEF-2.2 versus ENDF/B-VI used in DRAGON). The WIMS8 code has been used for evaluating high-temperature gas-cooled reactor systems employing particulate fuel in graphite matrix, and hence is adequate for the comparison. (The two codes predicted very similar k_∞'s for an at-power conditions in which the fuel particles and matrix graphite were explicitly represented and another case in which they were smeared together into a single composition.) The WIMS8 depletion chain was judged to be superior because it modeled more transmutation events; the modeling of transmutation events by DRAGON is limited only by the information available in the cross section library. The two codes however gave very similar trend of k_∞ with burnup for a constant-flux depletion case. For this case, the codes predicted practically the same time evolutions of the number densities of the primary nuclides. The slight differences in the time evolutions of the number densities of Pu-238 and Pu-242 were attributed to the differences in the depletion chains.

4.4.1.2   Core Models

Two three-dimensional core models were developed for performing the neutronics calculations of this study. The first is a Deterministic model for DIF3D [59] code and the second is stochastic model for MONK [56] code. The DIF3D code solves the multigroup transport equations or approximations of the equations by either nodal or finite difference approaches. It is also the computational engine of the REBUS3 fuel-cycle analysis package [60]. Both the eigenvalue and external source problems that are pertinent to the GT/AD-MHR system analysis are solved by DIF3D.

The whole-core, DIF3D-nodal diffusion theory model is used for calculating both the power distributions and reactivity states of the MHR core. A 23 neutron-energy group structure is

currently used in the model. This detailed group structure was selected to provide a good representation of the Pu and the Er resonances in the 0.2 to 1.1 eV energy range.

In the DIF3D calculations, 11 rings of hexagonal-prismatic assemblies are modeled, consistently with the GT-MHR design; this results in 331 radial computational nodes. A radial map of the core is provided in Figure 4-7. The central location can contain either inner reflector graphite elements or the spallation neutron-source target depending on whether the GT-MHR or AD-MHR is of interest. Similarly, the second ring can contain either inner reflector graphite elements or GCFR-type assemblies employing fuel particles that have been irradiated for more than four years in the system. The fourth and fifth rings contain the inner graphite reflectors. The GT-MHR thermal-zone fuel blocks are located in rings six to eight. Rings 9 to 11 contain the outer graphite reflector blocks. Axially, the whole length of the active core (about 793 cm), and additional lower and upper graphite reflector zones (100 cm each), are modeled. Forty axial computational nodes (30 in the active core) are employed in the DIF3D model. A void boundary condition is imposed on all external surfaces. It is currently being assumed that the reflector zones contain full density graphite.

The REBUS3 depletion model for the MHR core uses the DIF3D-nodal model discussed above for its neutronics calculations. The 23-group, microscopic cross sections obtained from the DRAGON unit-element depletion calculations are used for the REBUS3 model. The REBUS3 code capability that permits the fitting of both capture and fission cross sections of the active isotopes is employed in the calculations. This approach approximately accounts for cross section variations due to changes in the neutron spectrum as a function of the depletion. Seventeen heavy-metal nuclides are tracked in the full-core depletion calculations; these are all Pu, Np, Am, Cm and U isotopes. Additionally, 35 fission-product (FP) and one lumped-fission-product nuclides are employed in the REBUS3 model. The 35 FP nuclides account for about 95% or so of the overall reactivity effect attributable to fission products, and it is expected that this model is more than adequate for the current study. The heavy metal, the FP nuclides, and two erbium isotopes (Er-166 and Er-167) are specified as depletable active isotopes in the REBUS3 model.
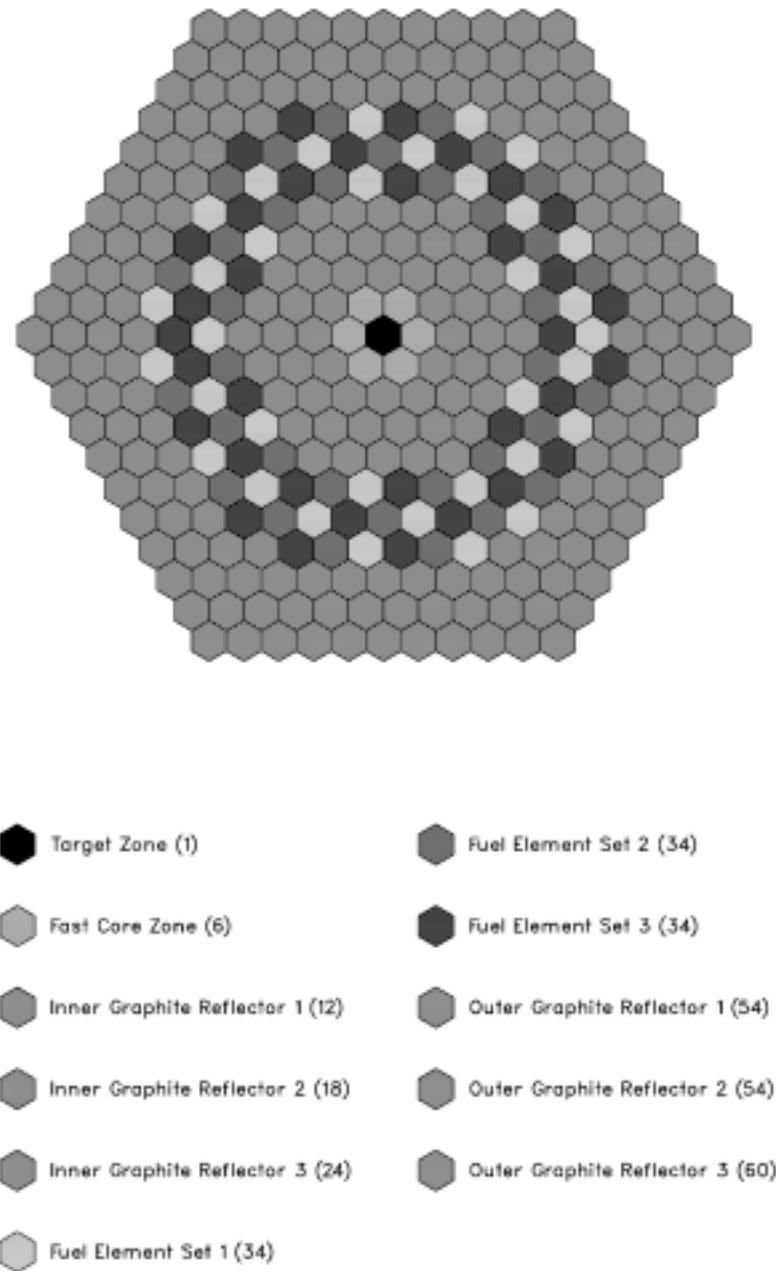
Figure 4-7.   A Sample Radial Core Map for the GT/AD-MHR

4.4.1.3 The MONK Model

The MONK model has explicit modeling for the fuel and burnable poison particles and all the geometrical details of the core as described above. A cylindrical boundary is used for the radial reflector to match the actual configuration shown in Figure 4-1. The model is shown in Figure 4-8 and Figure 4-9. The details of the particle model and fuel assembly are shown in Figure 4-4 through Figure 4-6. All the MONK calculations were performed at room temperature except the burnup analysis was performed at the average operating temperatures for each material. Also, the MONK burnup analyses used the 172-group nuclear cross section library with the explicit geometrical modeling. The reactivity standard deviation is 0.001.
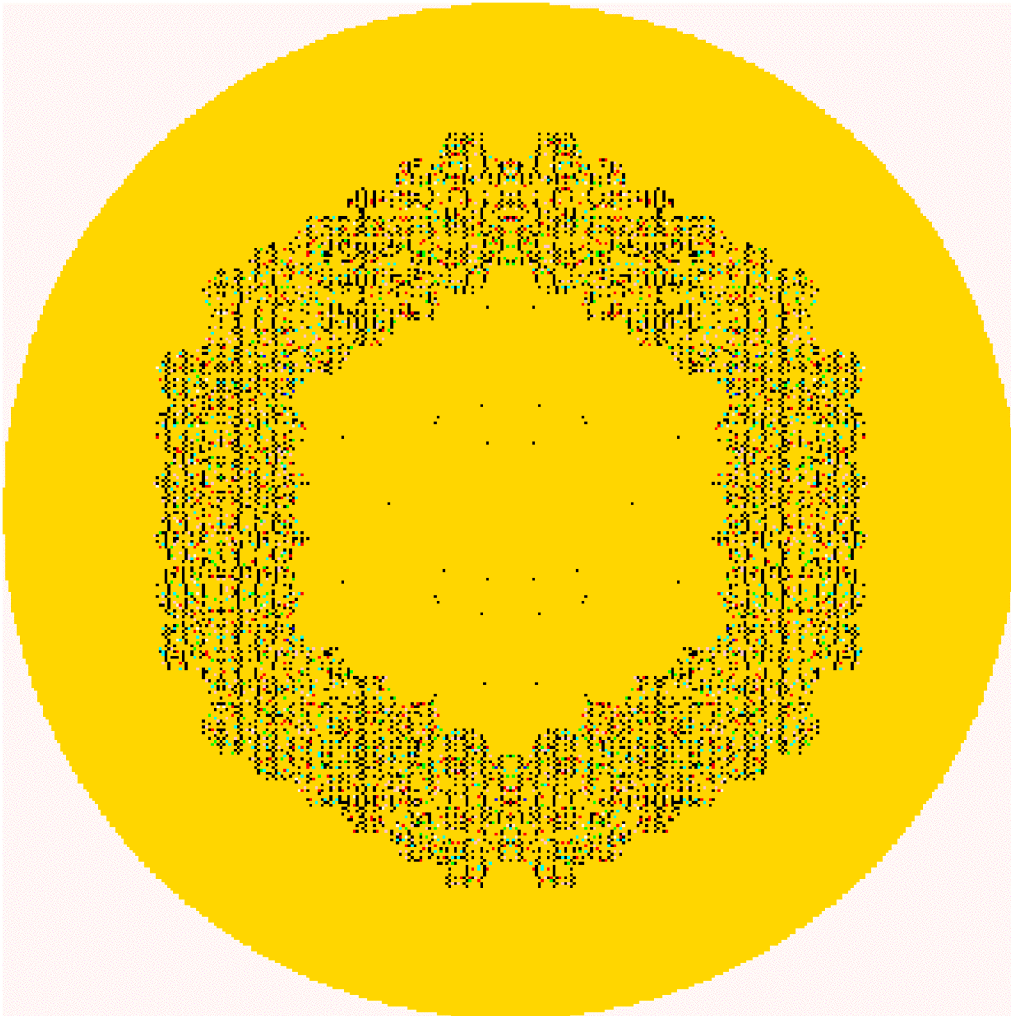
Figure 4-8.   MONK Core Model

Core power distributions predicted by MONK and DIF3D have been compared for a fresh core state having a heavy metal loading of 787 kg and an Er-167 loading of 27.7 kg. The

results indicated that the deterministic approach provides a very accurate model of the whole-core. The DIF3D model using assembly-average cross sections generated by DRAGON (but currently with no additional assembly homogenization factors) gave a maximum assembly power that is different by 0.4% from the MONK value. The maximum difference in assembly power is 2.5.

The results so far obtained in the verification calculations indicate that the deterministic models currently being employed by Argonne for assessing the GT-MHR design give accurate predictions of core performance parameters when compared to MONK results. Further effort is required to validate the burnup predictions.

Figure 4-9.   MONK Enlarged Core Section

4.4.2 LANL Path

The Monte Carlo radiation transport code MCNP was used to model neutron transport in the GA core. ENDF/B-VI continuous-energy cross sections were used, except for erbium isotopes with masses 162, 164, 168, and 170, for which cross sections from the Russian BROND-2.2 library were used.

Time-dependent nuclide build-up and depletion were modeled using Monteburns, a code that couples MCNP with ORIGEN-2. In the ORIGEN-2 burnup calculations, Monteburns replaces one-group neutron absorption cross sections from the ORIGEN-2 library with more accurate one-group cross sections calculated by MCNP. Monteburns automatically updates nuclide inventories in the MCNP transport calculation at each time step. Nuclides for which ENDF/B-VI data do not exist were ignored. Near the end of a cycle this may amount to 50% of the fission product inventory. However, fission product isotopes with large absorption cross sections are found in the ENDF/B-VI library and are therefore taken into account in the MCNP calculation.

A first step in this process is the evaluation of the required fidelity of geometric modeling. Even though the $TRUO_{1.7}$ kernels within the TRISO-coated particles are only 200μm in diameter, strong resonances in the absorption cross section of some isotopes (notably, ~100,000 b near 1 eV in Pu-240) may cause flux depression within the kernel at certain neutron energies. In this case, modeling the fuel particle atoms as being homogeneously distributed throughout the graphite matrix, which is simpler to model, may give erroneous results. Instead, the TRISO-coated particles may need to be modeled explicitly.

To evaluate the degree of geometric modeling required in MCNP, a lattice element was modeled two ways:

- Each TRISO-coated particle was modeled in detail, including all layers, and arranged in a uniform, body-centered cubic lattice structure within the graphite matrix of the fuel pin;

- The TRISO-coated particles and graphite matrix within a fuel element were homogenized, with the fuel "smeared" throughout the graphite matrix of the fuel pin;

For each case, one-sixth of a fuel block was modeled, as shown in Figure 4-10, and given reflecting boundaries. The central fuel-handling hole shown in this figure is present only near the top and bottom of the block. In all cases where erbium poisoning is included, the erbium compacts are a homogeneous mix of 15v% erbium and 85v% graphite. Other dimensions, materials, and densities were obtained from GA [1].
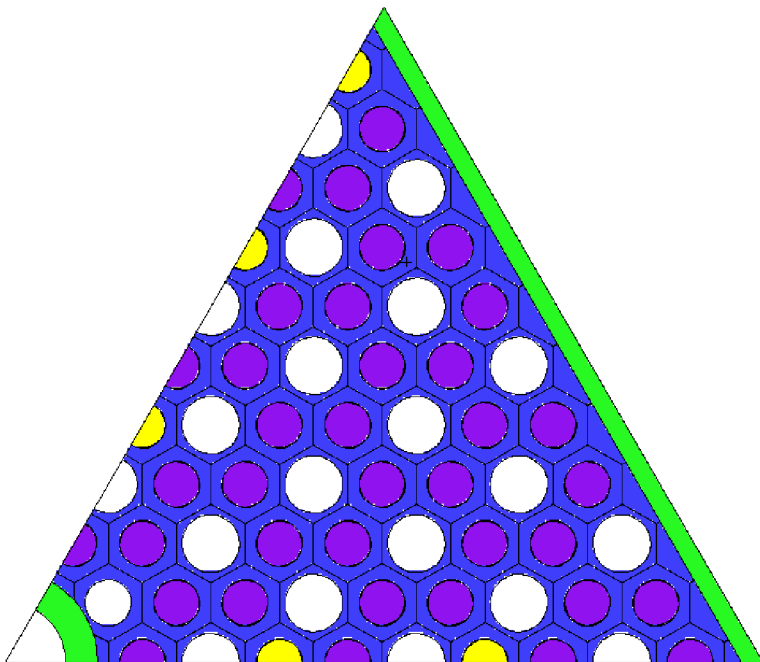
Figure 4-10.   MCNP Model of One-Sixth of a Thermal Fuel Assembly.

The results obtained from MCNP for both of these cases with and without the use of the erbium burnable poison are shown in Table 4-4. This table shows results for a 10% packing fraction of fuel particles with 200-μm-diameter kernels. The statistical error in k_∞ is ~0.001 in all cases.

Table 4-4.   Dependence of k_∞ on Fidelity of Geometric Modeling and Erbium Loading.

Fuel Pin Lattice	Erbium Loaded	k_∞	Pu-239 $\_f$ (barns)	Pu-239 $\_c$ (barns)	Pu-240 $\_c$ (barns)	Neutron Fraction Lost to Erbium
Discrete	yes	1.035	96.5	52.7	96.5	0.144
Smeared	yes	0.918	92.7	51.9	214.6	0.124
Discrete	no	1.235	105.4	57.2	139.8	n/a
Smeared	no	1.076	99.5	55.5	215.1	n/a

Table 4-4 shows k_∞ is appreciably different between the two models, with the smeared model having a significantly lower value. This is because the smeared model does not sufficiently self-shield the Pu-240 capture resonance just above 1 eV. The inadequacy of the smeared model to correctly predict the Pu-240 self-shielding allows more captures in Pu-240 and thus lowers k_∞ (the self-shielding of the Pu-239 resonance at 0.3 eV is not as severe, plus it affects both fission and capture). Comparison of the flux spectra for the two cases, shown in Figure 4-11, clearly illustrates the flux depression at 1 eV that arises from Pu-240 absorption. The self-shielding of the discrete model leads to more severe flux depression at this energy as compared to the smeared model. Also evident in Figure 4-11 is the flux

depression at 0.3 eV arising from the absorption resonance in Pu-239 at this energy. However, its magnitude is smaller than the depression at 1 eV.
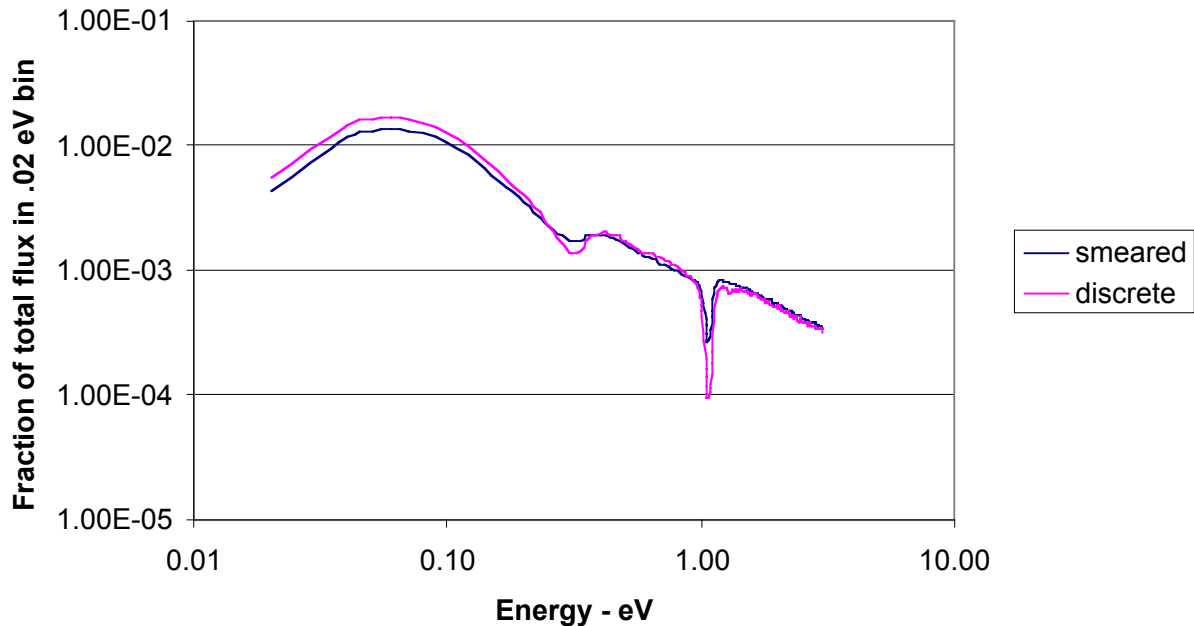
Figure 4-11.   Neutron Energy Spectra in the Fuel Pin for the Smeared and Discrete Models.

4.5 Parametric Studies: Fuel Block Neutronics

Criticality calculations of a lattice element were performed to gain an understanding of the dependence of the assembly reactivity on erbium loading, fuel kernel diameter and packing fraction, and operating temperature.

The reactor physics of the GT-MHR is complicated by the presence of the low-lying plutonium and Er-167 resonances (0.2 to 1.1 eV) and by the fact that the neutron spectrum has a low-energy peak about this energy range. This peak can change depending on the core state or material loading. The location of the peak and the direction of the spectral shift greatly affect both the resonance fission and capture rates and dictate the core or assembly criticality state and the magnitude and sign of reactivity coefficients.

4.5.1 Sensitivity to Fuel and Erbium Packing Fractions, and to Particle Size

The DRAGON model has been used to perform some parametric studies of the fuel block in order to obtain an understanding of the variables that affect the lattice reactivity. Figure 4-12 shows the variation of the assembly k_∞ as a function of the fuel-particle packing fraction for three different BP-particle packing fractions, at the hot operating state. (The blocks analyzed in the current GT/AD-MHR study have a packing fraction of 0.1 to 0.18.) The variation of k_∞ versus the packing fraction shows a peak below 0.05 packing fraction. The primary reason

for the trend is the shift in the neutron spectrum with the packing fraction. Above a packing fraction of 0.05 and as the packing fraction decreases, the carbon-to-heavy-metal ratio increases and leads to an increase in the thermalization of neutrons, causing the neutron spectrum to become softer. There are also competing effects arising from the decrease in the particle self-shielding with packing fraction. The relatively improved utilization of neutrons (relative increase in Pu-239 absorption rate), resulting from the softer spectrum however dominates and results in the k_∞ increasing as the packing fraction decreases. The increase in k_∞ with packing fraction, below the peak, is due to the fact that increase in the fissile content dominates. The packing fraction corresponding to the highest k_∞ differs for the three curves because as the BP loading increases, the spectrum hardens (increasing the relative absorption in Pu-240 and Er-167) and requires more fuel to achieve the same k_∞.
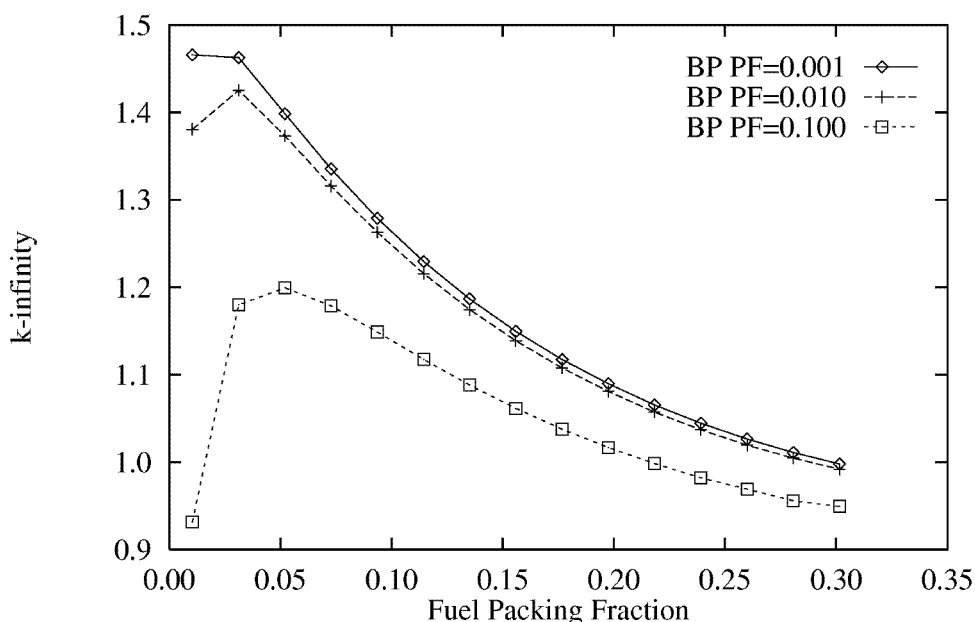
Figure 4-12. Unit Block k_∞ as a Function of Packing Fraction

Similar analyses were performed with MONK assembly model shown in Figure 4-4. The fuel-packing factor was varied from 0.05 to 0.25 in the compact at the col conditions to define the impact on k_∞ of the assembly. The MONK analysis used the 172-groups cross section data set. The erbium packing factor is 0.1. The results show a continuous decrease in k_∞ as the fuel-packing factor increases, as displayed in Figure 4-13. The MONK and the DRAGON results show the same effect on the assembly reactivity due to the changes in the fuel loading (packing factor).
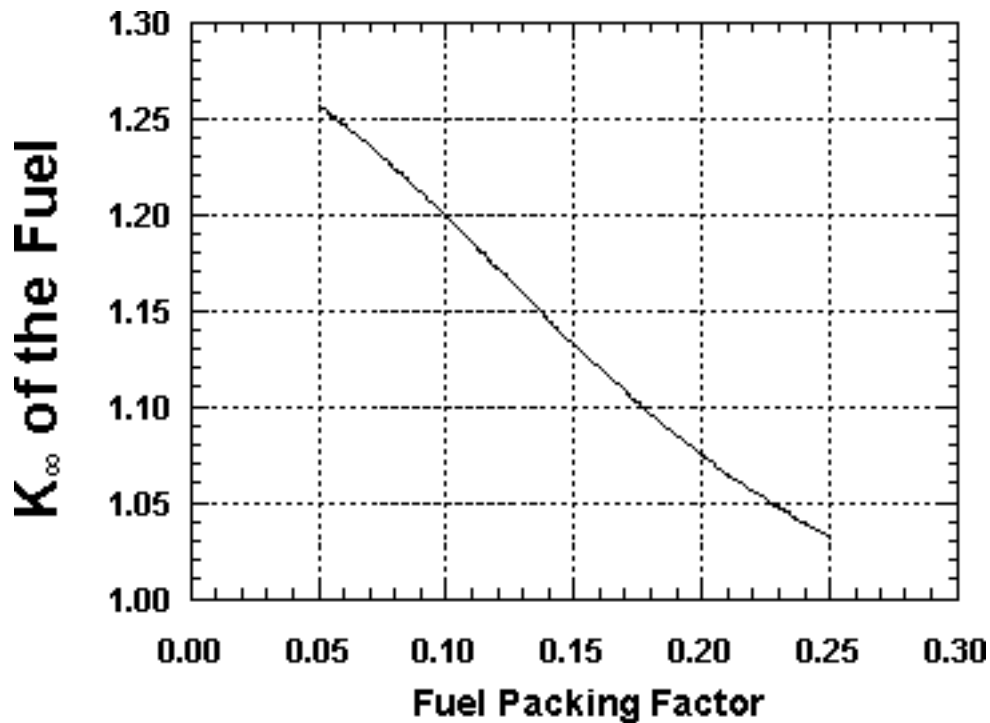
Figure 4-13. k_∞ **as a Function of the Fuel Packing Factor in the Compact**

Additional calculations were also performed to determine the effect of the fuel kernel diameter on the assembly k_∞, for an assembly with a BP particle packing fraction of 0.10. In these calculations, the thickness of the other particle layers was kept constant. Results for three fuel diameters (base diameter, double the base diameter, and half the base diameter) are displayed in Figure 4-14. These results were obtained by changing the fuel packing fraction in the same range as that used for generating Figure 4-12. The results show that for a given heavy-metal mass, the assembly k_∞ increases as the particle diameter increases.

An increase in the fuel kernel diameter leads to a decrease in the packing fraction and an increase in the distance between kernels. This causes a relative increase in the thermalization of neutrons and leads to a softer spectrum. Additionally, the larger diameter increases the self-shielding of the resonance absorbers (particularly Pu-240). Note that the Pu-239 resonance fission cross-section is also reduced by the self-shielding effect. However, the reduction of the Pu-240 absorption cross-section is the predominant effect.

MONK analyses were performed to study the effect of the burnable poison-packing factor on k_∞ of the assembly. The burnable poison-packing factor was varied from 0.05 to 0.40. The analysis used the 172-groups cross-section data set and the assembly model shown in Figure 4-4. The fuel-packing factor is 0.1287 in the compact. The results show a continuous decrease in k_∞, as the burnable poison-packing factor increases. The results are displayed in Figure 4-15.
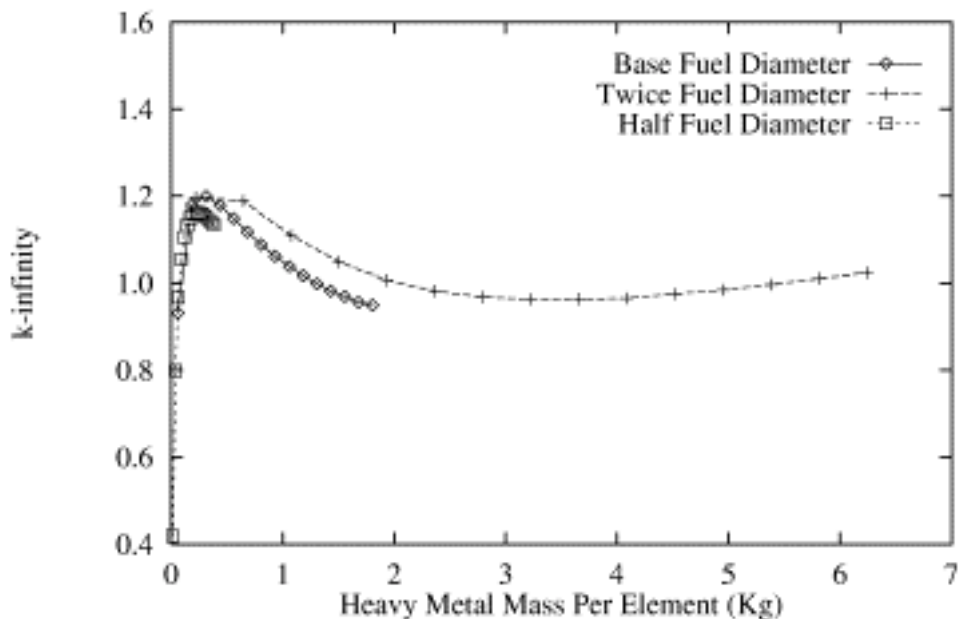
Figure 4-14. Assembly k_∞ vs. Heavy-Metal Mass (*BP PF = 0.1*)
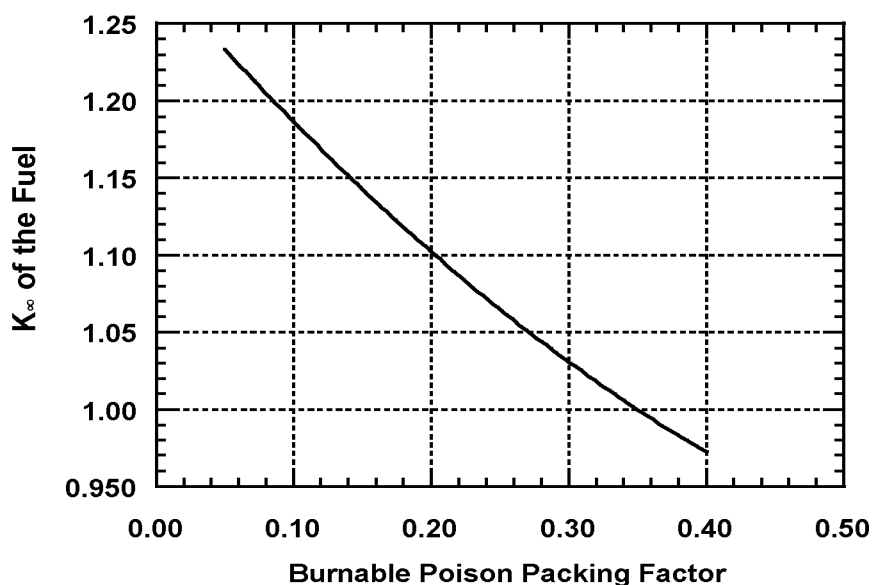
Figure 4-15. k_∞ as Function of the Burnable Poison Packing Factor in the Compact

Figure 4-16 shows the dependence of k_∞ on fuel particle packing fraction within the fuel compact using two different models, smeared and discrete representation of the compact calculated with MCNP. The value of k_∞ for the smeared and discrete cases approach each

other as the packing fraction increases because the composition more closely resembles a mix, but more importantly because the fuel loading increases such that the Pu-240 resonance approaches total self-shielding. These calculations demonstrate the need to model the TRISO-coated fuel particles discretely in order to obtain accurate results with MCNP.
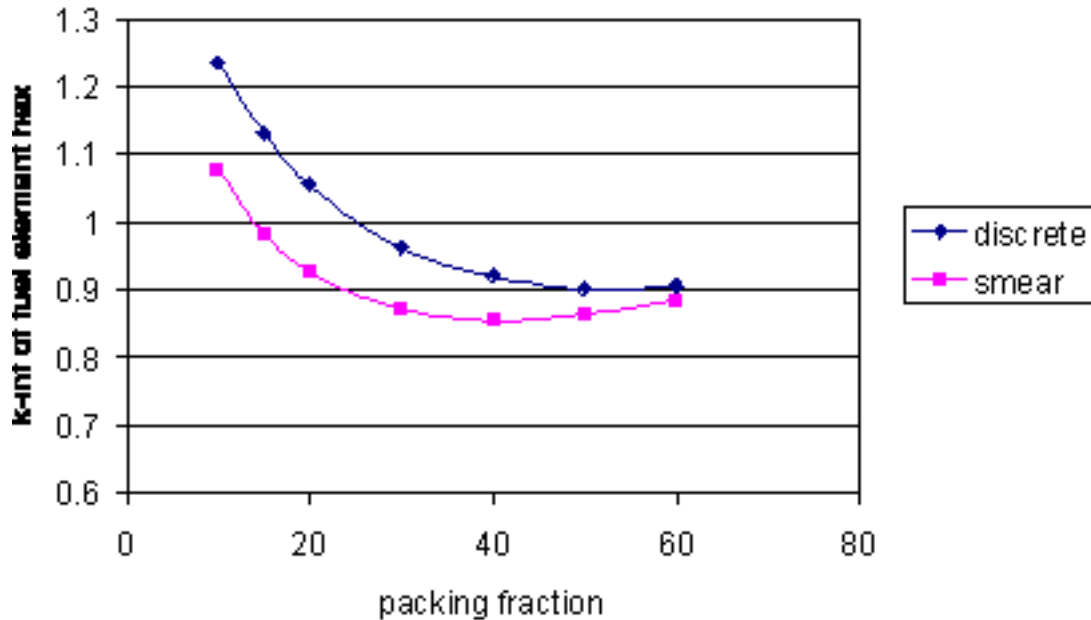
Figure 4-16. Reactivity vs. Packing Fraction for GT-MHR Fuel Block Modeled Discretely and Homogeneously (*200-µm-diameter TRUO$_{1.7}$ Kernels, no Erbium*).

The assembly reactivity depends sensitively on fuel loading and kernel size, as illustrated in Figure 4-17, where k_∞ is plotted as a function of the average fuel density in the compact. Minimum reactivity occurs in the range of 0.15 to 0.2 g/cm^3 of fuel, depending on the kernel diameter. Note that the fuel kernel density is 10.2 g/cc. Below this range, reactivity increases with decreasing fuel pin density because neutrons have a greater probability of downscattering through the Pu-240 resonance without encountering a fuel kernel. Above the range of minimum reactivity, reactivity increases with increasing fuel density for two reasons. First, at some point the Pu-240 resonance becomes sufficiently self-shielded such that adding additional Pu-240 does not negatively impact reactivity. Second, the decrease in graphite density that results from higher fuel density hardens the neutron spectrum, shifting more flux into the 0.3-eV resonance of Pu-239, which raises reactivity. In Figure 4-17, reactivity is plotted for two fuel kernel diameters, 200 µm and 400 µm. At a fixed fuel density, the packing fraction for the 200-µm kernels 2.3 times greater than for the 400-µm kernels. This lower packing fraction for the larger kernels means the neutrons undergo a higher average number of collisions with graphite between interactions with the fuel kernels. Thus there is a greater probability of downscattering through the Pu-240 resonance region without being absorbed, and so reactivity is higher for larger diameter kernels.
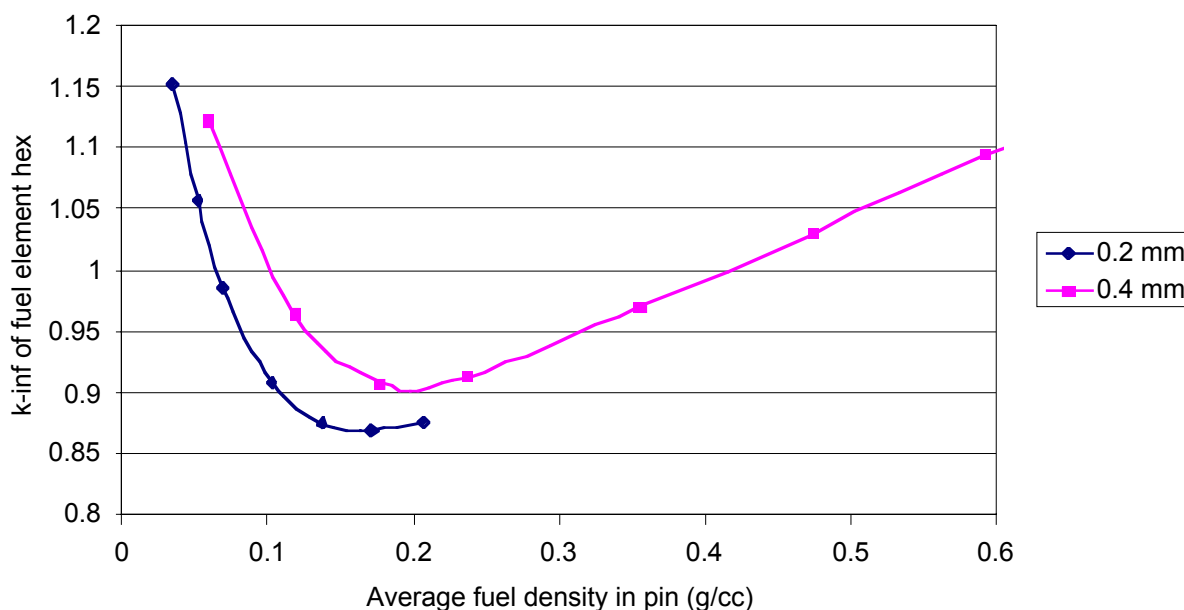
Figure 4-17.   Reactivity as a Function of Average Fuel Density for Two Kernel Diameters.

4.5.2 Sensitivity to Operating Temperatures

One important feature of the AD-MHR core is the net negative temperature coefficient between cold and operating conditions. As the core temperature increase, the neutron spectrum shift increases the neutron loss to the erbium-167 absorption resonance. The analysis was performed in steps to define the contribution of each material to this effect. The assembly model shown in Figure 4-4 was used for the analysis. MONK code was utilized to perform the calculation with the 172-groups nuclear data library. Four cases were analyzed as shown in Table 4-5. The packing factors are 0.15 and 0.1 for the fuel and the burnable poison, respectively. The first case has all the materials at 293.16°K. In the second case, the fuel particle temperature was changed to the average operating temperature without changing the temperature of the other materials. The third case is similar to the second case with the graphite temperature of the compact changed. The last case increased the temperature of the graphite assembly. The results from these cases show that heating the graphite material increases the neutron capture which results in a negative temperature coefficient.

Table 4-5. Temperature Effect on k_∞

Material Temperature	k_∞	Relative Difference (%)
Cold Conditions	1.1327	—
Hot Fuel Particles	1.1112	-1.90
Hot Compact	1.0954	-3.29
Hot Block	1.0562	-6.75

Also, sensitivity calculations performed with the DRAGON code indicate that the graphite temperature coefficient is the dominant contributor to the total temperature coefficient of the fresh, unburned fuel element. This trend indicates a need for a detailed analysis of the GT MHR system response to a fast transient, in which the graphite temperature feedback may be slow acting. It was also observed that both the fuel and graphite temperature coefficients become more negative with temperature.

4.5.3 Stochastic Burnup Analyses

Results of a burnup calculation using Monteburns for a discrete representation of the fuel lattice (10% fuel packing fraction of 200-µm-diameter kernels, 15% erbium packing fraction) are shown in Figure 4-18. Burnup was performed at an average flux ~4×10^{14} n/cm^2, which corresponds to a power of ~1 GW for the entire core. Results show the system can remain critical for about one year at this power level. Beyond this period, accelerator-driven subcritical operation would be required. Just over 60% of the actinide content is burned during the year of critical operation, and up to 80% is burned if driven by an accelerator for an additional 200 days.
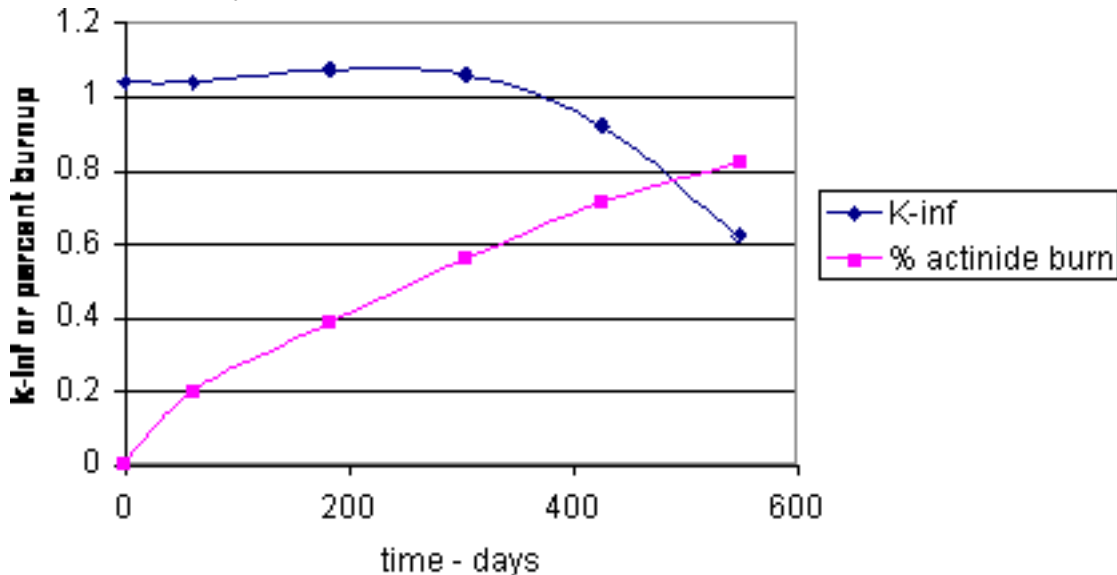
Figure 4-18. Burnup of a GT-MHR Fuel Block.

MONK burnup calculation was performed for the whole core using the core model shown in Figure 4-8. In this calculation the fuel compact, graphite block, and the reflector block temperatures are 1043.16°K, 993.16°K, and 993.16°K, respectively. The explicit representation of the geometry was maintained in the Monte Carlo and the burnup calculations. The standard deviation for the Monte Carlo calculation is 0.0025. The calculation was performed at constant fission power of 600 MW for 900 days. The packing factors for this core are 12.87 and 10% for the fuel and the burnable poison, respectively.

The results show that the fresh core has k_∞ of 1.1005. k_∞ drops to 1.0 after 600 days. At 900 days, k_∞ is about 0.8. About 49% of the TRUs are burned in the first 600 days, and 71% are burned at 900 days. At k_∞ of 0.9, the burnup is 64%. Er-167 is consumed at much faster rate as shown in Figure 4-19. Further investigation is required to define the optimum TRUs and Er packing factors to achieve 900 days of operation, if it is required, with adequate reactivity and Er-167 concentration.
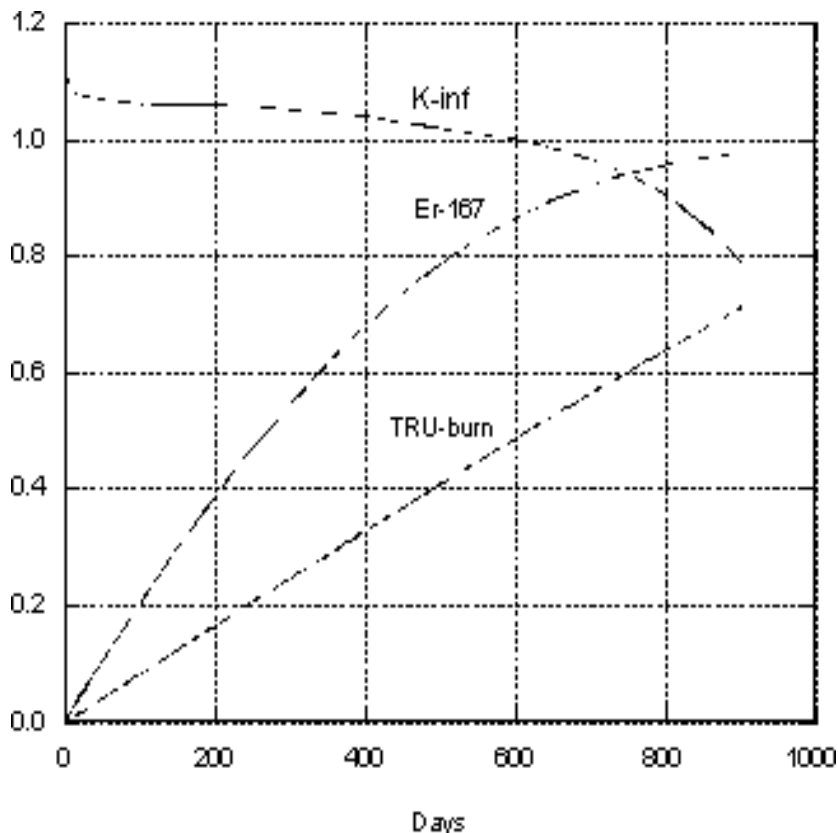
Figure 4-19. k_∞ **as Function of the Burnable Poison Packing Factor in the Compact.**

4.6 Parametric Studies: Core Neutronics

The DIF3D/REBUS3 models have been used to evaluate the feasibility of achieving very high Pu-239 and total plutonium consumption rates in the GT-MHR system. Two sets of core parametric studies were performed. These calculations employed no fast zone in order to

obtain a better understanding of the GT-MHR core design. The first set of calculations was for the single-batch fuel-loading scheme, originally proposed with the "Teledial" strategy. These calculations were used to investigate the effect of the initial masses of heavy metal and burnable poison (Er-167) on the design. The second set of calculations focused on the three-batch fuel-loading scheme. The results of these studies are presented in the following sections. In addition to these calculations a system point design analysis was performed for one of the cases. The results for this latter case are presented in Section 4.7.

4.6.1 Core Studies For Single-Batch Loaded Cores (No Fast-Zone)

Results for the single-batch-loaded cores with no fast-zone are summarized in Table 4-6. The two design parameters varied in this study are the initial heavy metal and Er-167 masses. Note that the final heavy-metal consumption rate, when k_{eff} is 0.92 (indicative of the end of residence time in the accelerator-driven system), depends very slightly on the initial masses. The critical cycle length and ITC at the end of the critical cycle are however quite sensitive to the parameters. The effects of variations in these initial masses are discussed in the following subsections.

Table 4-6. Single Batch Core Performance for Different Fuel and BP Masses (No Fast Zone)

Parameter	Case							
	00	01	02	03	04	05	06	07
Core Heavy Metal Loading (kg)	787	1010	1010	1010	1010	1054	600	600
Core Erbium-167 Loading (kg)	27.73	27.73	13.86	6.93	0.6186	0.6186	0.6186	12.0
Core Initial k_{eff}	1.0924	1.0687	1.1046	1.1250	1.1453	1.1382	1.2296	1.1752
ECOC, Length and Consumption Rates								
Length, Effective Full Power Days	405	450	540	585	585	585	360	333
k_{eff}	0.9974	0.9988	0.9999	0.9967	1.0012	1.0038	1.0118	1.0121
Pu-239 Consumption (%)	69	61	70	74	74	72	79	75
Total Pu Consumption (%)	34	30	36	39	39	37	40	37
Total Heavy Metal Consumption (%)	32	27	33	36	36	34	37	34
ITC at 300°C, pcm/°C		-2.16		5.81	6.12	5.11	12.01	10.10
Consumption Rates when k~0.92								
Length, Effective Full Power Days	630	855	855	855	855	855	480	467
k_{eff}	0.919	0.9125	0.9169	0.9189	0.9206	0.9189	0.9078	0.9153
Pu-239 Consumption (%)	91	92	92	92	92	92	93	92
Total Pu Consumption (%)	54	57	57	57	57	58	53	52
Total Heavy Metal Consumption (%)	49	52	52	52	52	53	49	48
ITC at 300°C, pcm/°C		12.84				12.22		
Peak Fast Fluence, 1.0E+21 n/cm^2	1.96	2.21	2.54	2.70	2.66	2.67	1.68	1.55

4.6.1.1 Effect of Variation in Initial Fuel Mass

For the same Er-167 amount (case00 versus case01 or case04 versus case06), the unburned-core k_{eff} increases as the initial mass of heavy metal decreases. This trend was also observed in unit assembly studies. A lower heavy-metal mass implies a higher carbon-to-plutonium ratio, which enhances neutron thermalization and results in a softer neutron spectrum. A softer spectrum also additionally reduces the resonance absorption in Pu-240 and Er-167 relative to that of Pu-239. These effects increase the fission rate in Pu-239 and hence the k_{eff}. While the higher k_{eff} ensures that the system would be critical during

operation, it however could be a disadvantage because it indicates a higher excess reactivity, which implies an increase in the control requirements.

A lower initial heavy metal mass gives a higher relative consumption level of plutonium and heavy metal at the end of critical operation cycle (ECOC). The critical operation cycle length is however shorter for this case. These can be explained by noting that the fissile mass required to produce a given power is fairly constant, given the similarity in the energy conversion factors. Therefore, for a given cycle length, the consumption level of heavy metal would be greater in a core with the lower initial mass. A certain amount of fissile material is however required to hold critical, causing the lower heavy-metal mass case to reach a k_{eff} value of unity faster (i.e., shorter cycle length). The rate at which the end of cycle is reached is also additionally affected by the relative absorption of neutrons in fission products, burnable poison and structural material, which are in turn affected by the neutron spectrum.

One primary disadvantage of the lower initial heavy metal design is the increase in the end of cycle isothermal temperature coefficient (i.e., becomes less negative or actually positive), in the temperature range below 300°C. This results because of the softer spectrum in the lower mass case and its accompanying reduction in neutron capture by Pu-240 and Er-167 and increase in neutron capture by certain fission products (see additional discussion on the ITC below).
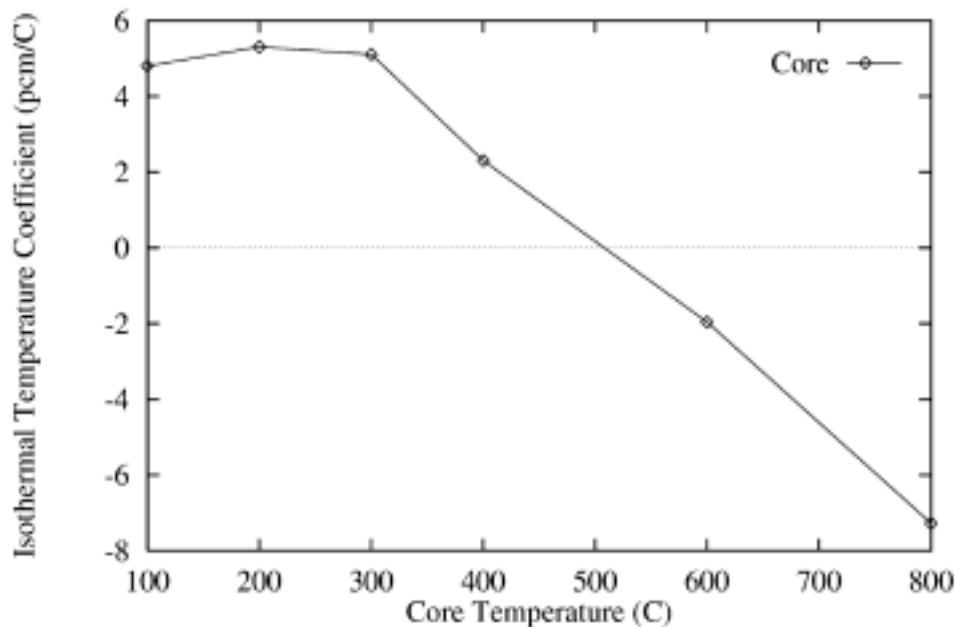
Figure 4-20. Temperature Dependence of ITC for Case05 (*ECOC Single-Batch Core*)

The ITC however becomes more negative with increase in temperature, as shown in Figure 4-20 for case05, and is negative at the full-power average temperature of about 770°C. (The core ITC values were obtained from DIF3D calculations employing 69-group cross sections obtained from DRAGON unit assembly calculations.)

In summary, a longer cycle length is achievable by using a higher heavy-metal mass. A higher heavy-metal loading however implies a lower specific power, which results in a reduction of the relative consumption level per unit time.

4.6.1.2 Effect of Variation in Burnable Poison

The Pu-239, total plutonium and heavy-metal consumption rates increase as the Er-167 mass decreases (case01 to case 04, and case06 versus case07). The primary cause of this is the softening of the neutron spectrum as the initial Er-167 mass decreases. The Er-167 loading cannot however be made arbitrarily small because Er-167 provides a strong negative component that help keep the ITC negative (or less positive) at lower temperatures. Additionally, Er-167 is also used to control the initial excess reactivity at BOC.

The results for case03 and case04 are fairly similar because the two cases have a very low Er-167 loading.

4.6.1.3 Isothermal Temperature Coefficient

The isothermal temperature coefficient (ITC) for the recycled LWR-discharge fuel proposed for use in the ATW becomes more positive in the gas-cooled system as the masses of Pu-240 and Er-167 decrease, for low operating temperature range. The decrease of these nuclides occurs with fuel burnup and additionally with a decrease in the initial loading specified for a given design. Typically, the presence of fission products with strong thermal absorption cross sections (e.g., Xe-135 and Sm-149) is a major cause of the ITC being positive with burnup. Both Er-167 and Pu-240 provide strong negative components to the ITC. An optimum Er-167 loading is therefore required to ensure a negative ITC.

While it is desirable for the ITC to be negative, a positive ITC alone is not enough to discard a design, particularly if the prompt Doppler coefficient is sufficiently negative, and since the positive ITC occurs in the low temperature range. The ITC becomes more negative with temperature (Figure 4-20) and is actually negative at the full-power operating temperature (average of about 700 – 800 ^{o}C). This is because the Doppler contribution from Pu-240 increases with temperature.

If it is required that the ITC be negative at all operating temperatures, getting a single batch loaded case that would give a k_{eff} of unity at the fresh unburned state might be a problem in this design (see for example the initial k_{eff} of case01). This is because the initial k_{eff} decreases with increases in both the initial heavy metal and Er-167 masses. One would be forced to employ a lower heavy-metal mass to get the system critical initially.

4.6.1.4 Fast Fluence

The peak fast fluence (E > 0.1 MeV) presented on Table 4-6 was obtained by finding a representative peak fast flux over the cycle and multiplying it by the discharge cycle length.

The peak fluxes for all the cases were fairly similar (typically within 10% of each other). The differences in the peak fast fluence are due primarily to the residence time.

4.6.2 Core Studies for Three-Batch Loaded Cores (No Fast-Zone)

Three of the cases studied under the assumption of a single-batch loading scheme were also re-evaluated assuming a three-batch loading scheme (the core comprises three equal sized fuel regions uniformly distributed in the thermal core region, and having three different ages of fuel. One segment is discharged at the end of each irradiation period, and replaced with a fresh batch). These cores (case01, case05, and case07) represent different combinations of initial heavy metal and Er-167 masses. The results for these cases are summarized on Table 4-7. Comparing the results for the three cases to their respective single-batch core results, we observe that the excess reactivity (initial k_{eff}) is smaller for the three-batch core. This trend arises because the beginning of critical operation cycle (BCOC) state is composed of a mixture of fresh, once-burned, and twice-burned fuel. Additionally, the fuel discharge length (3 times the cycle length in the 3-batch scheme) is generally higher than for the single batch case, and the Pu-239, total plutonium, and heavy metal consumption levels are also higher, primarily because of the higher discharge burnup.

Table 4-7. Three-Batch Core Performance for Different Fuel and BP Masses (No Fast Zone)

Parameter	Case		
	Case01	Case05	Case07
Core Heavy Metal Loading, kg	1010	1054	600
Core Erbium-167 Loading, kg	27.73	0.6186	12.0
Core Initial k_{eff}	1.0307	1.0660	1.0911
Cycle Length and Discharge Consumption Rates			
Length, Effective Full Power Days	160	260	150
k_{eff}	1.0062	1.0002	1.0027
Pu-239 Consumption (%)	64	86	90
Total Pu Consumption (%)	32	50	50
Total Heavy Metal Consumption (%)	29	46	46
Peak Fast Fluence, 1.0E+21 n/cm^2	2.36	3.54	2.17
Single Batch Initial k_{eff}	1.0687	1.1382	1.1752

The general trends observed for the single-batch core are still valid for the three-batch core. Specifically, as the Er-167 loading increases, the consumption levels and the cycle lengths are greatly reduced. The cycle length is also significantly reduced as the heavy-metal mass is decreased, because of the higher consumption rates.

4.7 System Point Designs

In view of the parametric studies described in the previous sections, two system point designs were developed:

- The first design by Taiwo (ANL) attempts to stay close to the original GA concept and optimizes the initial fuel and erbium loadings; it uses a three-batch core to reach a significant cycle length and high burnup.

- The second design by Poston (LANL) uses a larger fuel particle and a larger core to achieve similar performances.

4.7.1 The ANL Design

The GA "Telediel" concept aims to run a transmuter island containing four transmuters operating concurrently, with three units running in the critical mode, and the fourth running in the accelerator (source) driven mode. It is therefore expected that the cycle length of both the critical and accelerator-driven modes would be the same, if no unit were to be idle for a long time. The preliminary GA proposal specifies a cycle length of a year. Of the cases studied so far case05 is the only one that meets this requirement, assuming a capacity factor of about 0.71 to 0.74. For this reason, case05 was selected for the SPD analysis. Note that if the single batch scheme is the preferred fuel management path a higher fuel mass than those studied so far, would be required to get a single-batch cycle length of more than 800 days.

Both the single-batch and three-batch fuel loading schemes with an inner fast-zone were analyzed. The nuclide mass flow in the system has been the focus of the current study and so no explicit fast element design has been used. The fast-zone is represented similarly as the thermal-zone, using the thermal assembly dimensions. Nuclide masses representative of the zone composition are however used. In the final design, the fast-zone elements will have a smaller pitch and different fuel pin dimensions. The elements would however be required to fit in the slots vacated by graphite columns in ring around the target.

Obtaining the initial nuclide masses for the fast-zone required some iteration. This is because in the GA proposal, the fuel that is loaded into the fast-zone is one that has been burned in a critical operation cycle (for three cycles or one cycle, for the three-batch or one-batch scheme, respectively), and has additionally undergone a one-year irradiation in an accelerator-driven cycle. The fuel is then additionally burned in the fast-zone for another four 1-year cycles in the three-batch loading scheme and four-years in the one-batch loading scheme. (The four years in the latter case is equivalent to one critical operation cycle and one accelerator-driven cycle.)

4.7.1.1 Steps for Obtaining the Initial Fast-Zone Nuclide Masses for the Three-Batch Core

The approaches used for getting the initial fuel masses for the fast-zone were slightly different for the two cases. In the three-batch core model, the following steps were used:

1. A three-batch calculation employing the REBUS3 critical equilibrium cycle model, and with no fuel in the fast zone, was depleted at a power level of 600 MW. This case was also used to get an estimate of the cycle length. For case05, the cycle length was found to be about 260 days (see Table 4-7).

2. The homogeneous discharge masses from the end of equilibrium cycle case (step 1), representative of the average thrice-burnt thermal-zone fuel, are used in a REBUS3 non-equilibrium problem. This case was burned at 540 MW (~90%) for one year (i.e., 270 effective full power days) in an accelerator-driven cycle. Again no fast-zone is present in this case. The assumption of using uniform masses is sufficiently accurate since it is likely that fuel elements would be both axially and radially shuffled to give a uniform power distribution in the accelerator-driven system. Also the peak-to-average burnup from step 1 is about 1.10 (min-to-average is about 0.90).

3. The homogeneous thermal-zone, heavy-metal masses corresponding to the end of the accelerator-driven cycle (EADC), are used in the second row of assemblies (fast-zone) of a REBUS3 critical non-equilibrium model. Fresh fuel is initially loaded in the thermal zone of this model. This case is burned using a power level of 600 MW. The discharge times of the thermal batches are staggered by one cycle and the fast-zone assemblies reside in the core for three cycles, in the model. The procedure it then repeated for 5 fuel management operations to get an equilibrium state.

4. The homogeneous, fast-zone and thrice-burned thermal-zone masses are retrieved from step 3 and then used in a REBUS3 accelerator-driven non-equilibrium cycle model. (The fast-zone and thermal-zone masses remain in their respective positions.) The REBUS3 run is made for one cycle using an external source that maintains a power level of 600 MW. It is the fast-zone masses at the end of this cycle that are of interest. Note that in the actual design, the thermal zone masses come from three cycles (they correspond to the ECOC masses). In that case, 2/3 of the elements has been in storage for two cycles.

5. Since this process was initiated with guess masses, it is necessary to go back to step 3 with the thermal-zone masses and iterate until convergence of these masses.

4.7.1.2 Steps for Obtaining the Initial Fast-Zone Nuclide Masses for the Single-Batch Core

The approach used for obtaining the initial heavy-metal masses for the fast-zone of the single-batch core is different from that outlined above. The modified steps for the single-batch core follow:

1. A single-batch, no fast-zone, REBUS3 critical non-equilibrium cycle calculation is run to 900 days at a power level of 600 MW. This case is also used to get an estimate of the cycle length. For case05, the cycle length was found to be about 585 days (see Table 4-6).

2. Using the step 1, homogeneous, thermal-zone masses at ECOC (at 585 days) and at about 810 days (an additional ~1/3 cycle length), in the thermal zone and fast zone, respectively, setup a REBUS3 accelerator-driven non-equilibrium cycle model. Run this case with an external neutron source that maintains a power level of 600 MW, for 200 days. (Because the thermal-zone fuel is still neutronically active, an additional load of Er-167 was used in the thermal-zone, to ensure a sub-critical state.)

3. Get the nuclide masses from the thermal-zone at EADC of step 2, and use these masses in the fast-zone of another REBUS3 critical non-equilibrium cycle model. Fresh fuel is loaded in the thermal-zone of this cycle. Burn this cycle at a power level of 600 MW, to the end of critical cycle when k = 1.00 (about 720 days).

4. Retrieve the homogeneous, fast-zone and thermal-zone masses and used them in a REBUS3 accelerator-driven non-equilibrium cycle model. (The fast-zone and thermal-zone masses remain in their respective positions.) Again, additional Er-167 loading is required to ensure a sub-critical state. This case is burned for 1/3 of the critical cycle length (240 days) using an external source that gives a power level of 600 MW. It is the fast-zone masses at the end of this cycle that are of interest.

5. Since this procedure was initiated with guess masses in step 2, proceed to step 3 with the thermal-zone masses and iterate until convergence of these masses.

4.7.1.3 Discussion of Results

Table 4-8 and Table 4-9 contain the system performance results for the three-batch core employing a fast-zone in both critical and accelerator-driven cycles. The Pu-239, total plutonium and heavy-metal consumption rates at ECOC and EADC are provided in Table 4-8. The EOC discharge masses are provided in Table 4-9; the total heavy-metal mass reported on Table 4-9 includes those for uranium isotopes. The consumption rates are relative to the initially fresh fuel masses. The final consumption rates of interest are those for the fast-zone at EADC. Additionally, the consumption rates at the end of 90 days are provided, since this is when the multiplication factor is about 0.90 in the three-batch

accelerator-driven cycle. The system k_{eff} and multiplication factor during the critical operation and accelerator-driven cycles are summarized in Table 4-10. Similar results are presented for the single-batch core in Table 4-11, Table 4-12, and Table 4-13.

Table 4-8. Three-Batch Core Consumption Rates in the GT/AD-MHR System

	Discharge ECOC	Accelerator-Driven Cycle, After 90 Days		Accelerator-Driven Cycle, EADC (270 Days)	
	Thermal-Zone	Thermal-Zone	Fast-Zone	Thermal-Zone	Fast-Zone
Pu-239 (%)	86	90	96	95	97
Total Pu (%)	50	55	67	63	71
Total Heavy-Metal (%)	45	50	61	57	64

Table 4-9. Er-167 and Heavy Metal Masses for Three-Batch Core

		Discharge at ECOC		Discharge at EADC	
Nuclide	Initial Mass (Kg)	Thermal Zone Mass (Kg)	Fast Zone Mass (Kg)	Thermal Zone Mass (Kg)	Fast Zone Mass (Kg)
Er-167	0.61	—	0.00	0.00	0.0
Np-237	43.20	25.52	18.54	20.41	14.91
Pu-238	12.65	46.07	56.52	49.33	52.94
Pu-239	543.21	74.68	22.79	27.13	17.08
Pu-240	251.64	133.47	73.95	84.81	63.50
Pu-241	84.20	134.50	63.96	85.42	44.41
Pu-242	52.69	86.21	107.35	104.39	98.67
Am-241	52.69	19.05	17.60	11.15	13.10
Am-242	1.05	0.46	0.26	0.24	0.26
Am-243	10.53	29.45	37.52	35.34	43.06
Cm-242	0.00	7.83	0.60	7.15	3.00
Cm-243	0.00	0.26	0.17	0.21	0.18
Cm-244	2.11	15.61	21.28	22.29	24.31
Cm-245	0.00	1.53	2.78	1.53	6.18
Total Heavy-Metal Mass	1054.0	574.6	423.42	449.4	381.6

Table 4-10. Three-Batch Core, k_{eff}, Multiplication Factor and Power Sharing

Critical Operation Cycle			
Burn Time (Days)	k_{eff}	Power Fraction	
		Thermal Zone	Fast Zone
0	1.074	0.97	0.03
135	1.030	0.97	0.03
270	1.006	0.97	0.03
Accelerator-Driven Cycle			
Burn Time (Days)	Multiplication Factor	Power Fraction	
		Thermal Zone	Fast Zone
0	0.963	0.90	0.10
90	0.896	0.81	0.19
180	0.817	0.70	0.30
270	0.732	0.59	0.41

Table 4-11. Single-Batch Core Consumption Rates in the GT/AD-MHR System

	Discharge, ECOC	Accelerator-Driven Cycle, EADC (240 Days)	
	Thermal-Zone	Thermal-Zone	Fast Zone
Pu-239 (%)	80	91	94
Total Pu (%)	44	56	61
Total Heavy-Metal (%)	40	51	56

Table 4-12. Er-167 and Heavy Metal Masses for Single-Batch Core

Nuclide	Initial Mass (Kg)	Discharge at End Critical Operating Cycle		Discharge at End of Accelerator-Driven Cycle	
		Thermal Zone Mass (Kg)	Fast Zone Mass (Kg)	Thermal Zone Mass (Kg)	Fast Zone Mass (Kg)
Er-167	0.61	0.09	0.00	2.29	0.0
Np-237	43.20	27.58	22.07	23.02	19.16
Pu-238	12.65	40.60	52.53	46.22	51.58
Pu-239	543.21	106.60	42.81	47.78	33.36
Pu-240	251.64	173.42	133.45	134.81	122.56
Pu-241	84.20	129.29	81.48	97.77	66.57
Pu-242	52.69	79.63	93.62	93.33	90.32
Am-241	52.69	21.31	21.22	14.53	18.50
Am-242	1.05	0.54	0.34	0.31	0.38
Am-243	10.53	26.26	32.86	31.40	36.99
Cm-242	0.00	9.13	0.91	7.72	2.66
Cm-243	0.00	0.23	0.24	0.26	0.23
Cm-244	2.11	11.62	14.68	15.74	15.31
Cm-245	0.00	2.24	3.65	2.73	6.58
Total Heavy-Metal Mass	1054.0	628.50	499.9	515.68	464.29

Table 4-13. Single-Batch Core, k_{eff}, Multiplication Factor and Power Sharing

Critical Operation Cycle			
Burn Time (Days)	k_{eff}	Power Fraction	
		Thermal Zone	Fast Zone
0	1.137	0.96	0.04
80	1.100	0.96	0.04
240	1.079	0.96	0.04
480	1.042	0.96	0.04
720	0.991	0.95	0.05
Accelerator-Driven Cycle			
Burn Time (Days)	Multiplication Factor	Power Fraction	
		Thermal Zone	Fast Zone
0	0.963	0.87	0.13
80	0.927	0.80	0.20
160	0.880	0.72	0.28
240	0.827	0.64	0.36

The results in Table 4-8 to Table 4-13 can be summarized as follows:

1. The consumption rates at the end of the critical operation cycles of the single-batch and three-batch cores with the fast-zone are similar to those presented on Table 4-6 and Table 4-7 for the same cores without the fast-zone. The relatively larger differences for the single-batch core results because of the much longer cycle length for the case with the fast zone.

    The reactivity trends of the critical operation cycle are also similar to the trends obtained for the case with no fast-zone. Specifically, the three-batch core has a lower excess reactivity at BCOC and higher plutonium and heavy-metal consumption rates at the ECOC.

2. The multiplication factor of the three-batch core varies from 0.963 to 0.732, implying a seven-fold increase in the source strength over the cycle, to keep the power level constant. (A five-fold increase is required for the single-batch core.) Limitations on the maximum source level might restrict the cycle length for these cases. In that event, there could be a mismatch between the cycle lengths of the critical operation and the accelerator-driven cycles that could complicate the "Teledial" concept.

    The single-batch and three-batch cores both have the same multiplication factor (0.963) at the beginning of the accelerator-driven cycle. The EADC multiplication factor of the three-batch core however falls off drastically over the cycle relative

to that of the single-batch core (0.73 versus 0.83). This is because the initial state reactivity of the single-batch core is much higher than that of the three-batch core; this initial reactivity was suppressed using additional burnable poison particles.

3. The power fractions of the fast and thermal zones are fairly constant during the critical operation cycle in both single-batch and three-batch cores. The fast-zone accounts for about 3-5% of the total power in both the single-batch and three-batch cores.

   The power fraction of the fast–zone increases with burnup in the accelerator-driven cycle, for both the single-batch and three-batch cores. This is because the neutron flux falls off with increase in distance from the source, attenuated by the material properties of the zones along the path. As the system becomes more subcritical, and as the neutron multiplication in the thermal-zone decreases with burnup, a more pronounced tilt results.

   The core radial power distributions are presented on Figure 4-21 and Figure 4-22, for the three-batch core and Figure 4-23 and Figure 4-24 for the single-batch core. The axial power profiles in the fast-zone of the critical operation and in the accelerator-driven cycles are also displayed in Figure 4-25 and Figure 4-26. (The radial and axial power profiles are normalized to the core average power density.) The critical operation power distributions are relatively flat and the peak is within acceptable limits. The power peaking is more pronounced in the accelerator-driven cycle than in the critical operation cycle. The highest power densities are recorded in the fast-zone of the accelerator-driven cycle, and they increase with irradiation time.
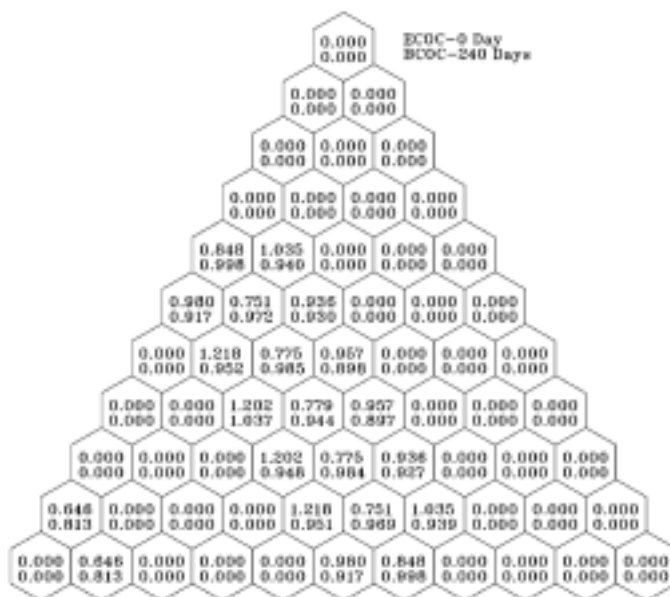
Figure 4-21. Sixth-Core Radial Power Distribution for Three-Batch Core in Critical Operation Cycle (*Lower left hexagon is the core central location*)

The axial power profile of the fast-zone peaks significantly at the center, because this is the level that the external source is located.

4. Because the fast zone sees about 3 to 5% of the total power during the critical operation cycle, the plutonium and heavy-metal consumption rates of the fuel residing in this zone is quite small. Additionally, since the fast zone also sees about 10 to 20% or so during its stay in the accelerator-driven cycle (for a reasonable multiplication factor), the overall consumption of fuel in this zone is not very great. Note from Table 4-7 and Table 4-10 that the total heavy-metal (implying minor actinides) benefit more from the fast–zone irradiation than Pu-239. This is due to the harder neutron spectrum in the zone.

5. A harder neutron spectrum exists in the fast zone relative to the thermal zone, as evident in the spectra displayed in Figure 4-27, for the three-batch core. The fast-zone spectrum is however softer than that possible in a fast transmuter (see Figure 4-26). Figure 4-28 was obtaining using the beginning of accelerator-driven cycle fast-zone composition in a zero current boundary calculation.

BADC−0 Day
EADC−240 Days

Figure 4-22 data (each hexagon shows BADC / EADC values):

- 0.000 / 0.000
- 0.000 / 0.000 | 0.000 / 0.000
- 0.000 / 0.000 | 0.000 / 0.000 | 0.000 / 0.000
- 0.000 / 0.000 | 0.000 / 0.000 | 0.000 / 0.000 | 0.000 / 0.000
- 0.731 / 0.531 | 0.805 / 0.505 | 0.000 / 0.000 | 0.000 / 0.000 | 0.000 / 0.000
- 0.932 / 0.640 | 0.701 / 0.577 | 0.770 / 0.520 | 0.000 / 0.000 | 0.000 / 0.000 | 0.000 / 0.000
- 0.000 / 0.000 | 1.169 / 0.808 | 0.737 / 0.639 | 0.798 / 0.539 | 0.000 / 0.000 | 0.000 / 0.000 | 0.000 / 0.000
- 0.000 / 0.000 | 0.000 / 0.000 | 1.203 / 0.954 | 0.748 / 0.657 | 0.798 / 0.538 | 0.000 / 0.000 | 0.000 / 0.000 | 0.000 / 0.000
- 0.000 / 0.000 | 0.000 / 0.000 | 0.000 / 0.000 | 1.203 / 0.847 | 0.737 / 0.640 | 0.770 / 0.519 | 0.000 / 0.000 | 0.000 / 0.000 | 0.000 / 0.000
- 2.223 / 6.197 | 0.000 / 0.000 | 0.000 / 0.000 | 0.000 / 0.000 | 1.169 / 0.809 | 0.701 / 0.576 | 0.805 / 0.504 | 0.000 / 0.000 | 0.000 / 0.000 | 0.000 / 0.000
- 0.000 / 0.000 | 2.223 / 6.197 | 0.000 / 0.000 | 0.000 / 0.000 | 0.000 / 0.000 | 0.932 / 0.640 | 0.731 / 0.531 | 0.000 / 0.000 | 0.000 / 0.000 | 0.000 / 0.000 | 0.000 / 0.000

Figure 4-22. Sixth-Core Power Distribution for Three-Batch Core in Accelerator-Driven Cycle (*Lower left hexagon is the core central location*)

BADC−0 Day
EADC−240 Days

Figure 4-23 data (each hexagon shows BADC / EADC values):

- 0.000 / 0.000
- 0.000 / 0.000 | 0.000 / 0.000
- 0.000 / 0.000 | 0.000 / 0.000 | 0.000 / 0.000
- 0.000 / 0.000 | 0.000 / 0.000 | 0.000 / 0.000 | 0.000 / 0.000
- 0.731 / 0.531 | 0.805 / 0.505 | 0.000 / 0.000 | 0.000 / 0.000 | 0.000 / 0.000
- 0.932 / 0.640 | 0.701 / 0.577 | 0.770 / 0.520 | 0.000 / 0.000 | 0.000 / 0.000 | 0.000 / 0.000
- 0.000 / 0.000 | 1.169 / 0.808 | 0.737 / 0.639 | 0.798 / 0.539 | 0.000 / 0.000 | 0.000 / 0.000 | 0.000 / 0.000
- 0.000 / 0.000 | 0.000 / 0.000 | 1.203 / 0.954 | 0.748 / 0.657 | 0.798 / 0.538 | 0.000 / 0.000 | 0.000 / 0.000 | 0.000 / 0.000
- 0.000 / 0.000 | 0.000 / 0.000 | 0.000 / 0.000 | 1.203 / 0.847 | 0.737 / 0.640 | 0.770 / 0.519 | 0.000 / 0.000 | 0.000 / 0.000 | 0.000 / 0.000
- 2.223 / 6.197 | 0.000 / 0.000 | 0.000 / 0.000 | 0.000 / 0.000 | 1.169 / 0.809 | 0.701 / 0.576 | 0.805 / 0.504 | 0.000 / 0.000 | 0.000 / 0.000 | 0.000 / 0.000
- 0.000 / 0.000 | 2.223 / 6.197 | 0.000 / 0.000 | 0.000 / 0.000 | 0.000 / 0.000 | 0.932 / 0.640 | 0.731 / 0.531 | 0.000 / 0.000 | 0.000 / 0.000 | 0.000 / 0.000 | 0.000 / 0.000

Figure 4-23. Sixth-Core Radial Power Distribution for Single-Batch Core in Critical Operation Cycle (*Lower left hexagon is the core central location*)
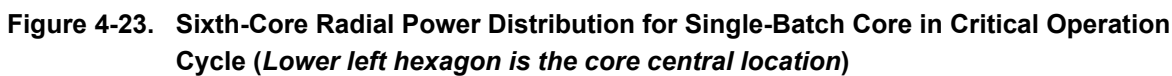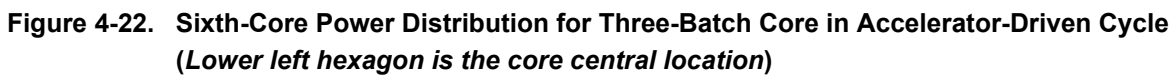
Figure 4-24. Sixth-Core Power Distribution for Single-Batch Core in Accelerator-Driven Cycle (*Lower left hexagon is the core central location*)
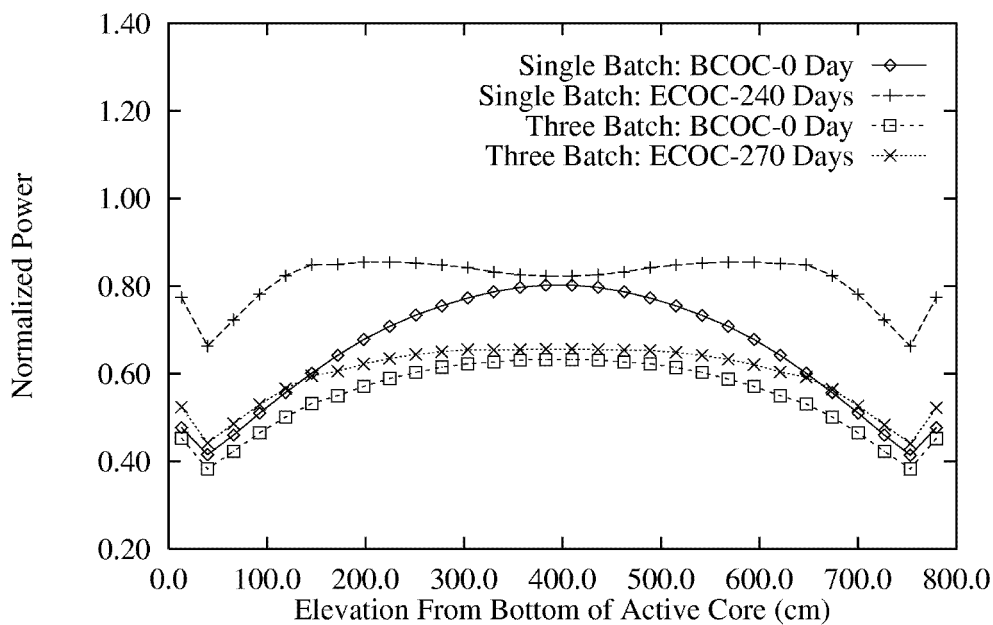

Figure 4-25. Axial Power Distribution in the Fast-Zone During Critical Operation Cycle
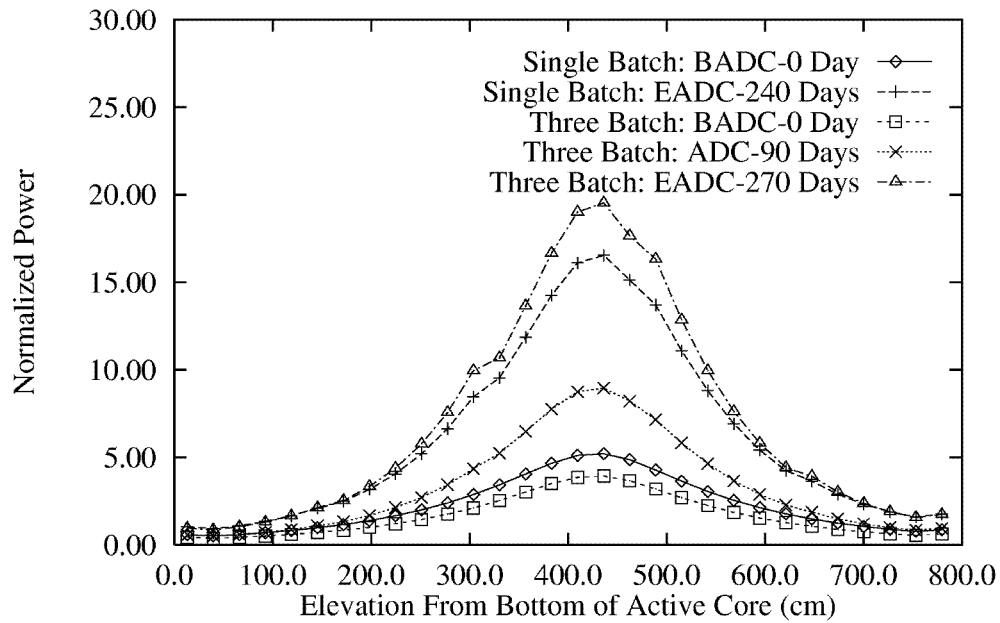
Figure 4-26. Axial Power Distribution in the Fast-Zone During Accelerator-Driven Cycle
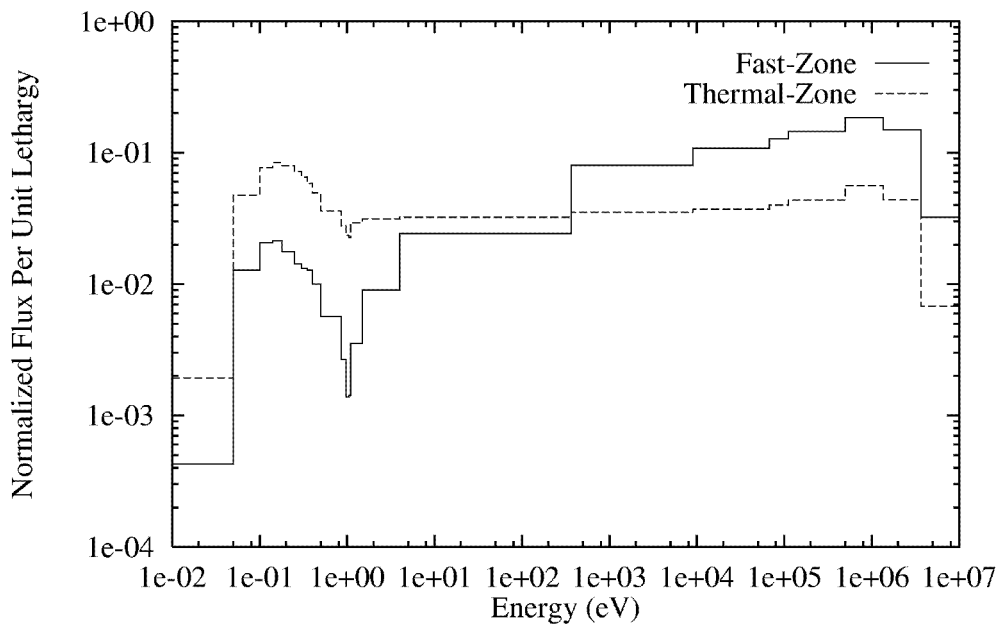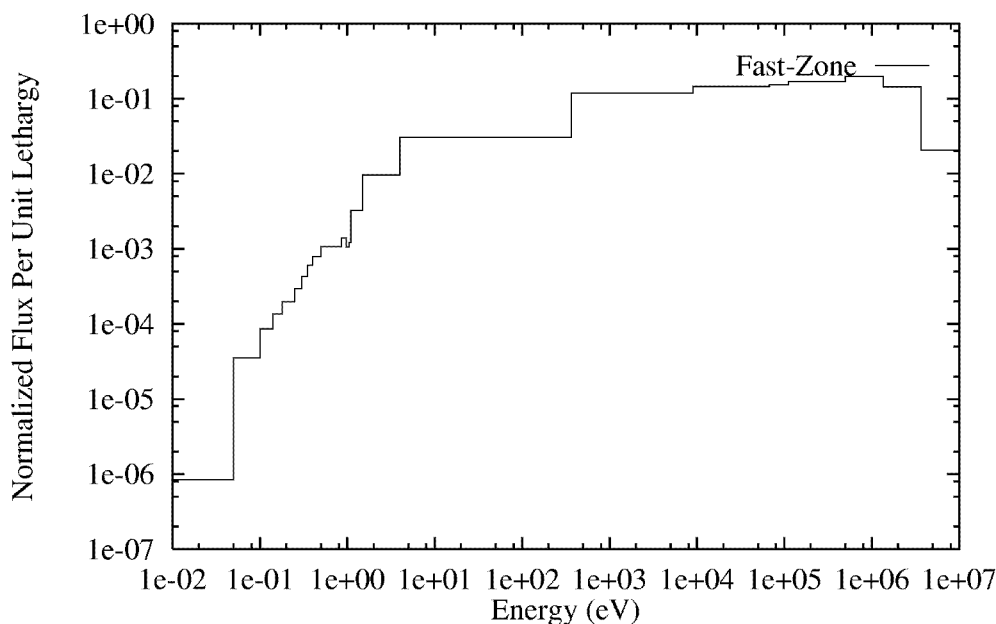

Figure 4-27. Zonal Spectra for Beginning of the Accelerator-Driven Cycle (*Three-Batch Core*)

**Figure 4-28. Fast-Zone Critical Spectrum Using Beginning of Accelerator-Driven Cycle
Composition (*Three-Batch Core*)**

4.7.1.4 *Preliminary Thermal Hydraulic Analysis of the Fast Region*

An estimate of the allowable power density in the fast spectrum zone of the ATW/GT-MHR
conceptual design is made based on the thermal-hydraulic characteristics of:

1. the proposed GCFR design, and
2. the proposed GT-MHR design.

Table 4-1 compares the performance characteristics of these reactor designs. The GCFR
design data were taken from Reference 60, and the GT-MHR design data were taken from
Reference 61.

The fast spectrum zone of the ATW/GT-MHR is assumed to consist of an array of hexagonal
GCFR subassemblies, made up of fuel pins clad with stainless steel arranged on a
triangular mesh. For reference, the cladding outer diameter, pin pitch, and pin length are
assumed to be identical to the GCFR design.

The power density in the fast zone will be limited by the available coolant flow rate provided
by the core pressure drop in the GT-MHR design. According to the information presented in
Table 4-14, the core pressure drop available in the GT-MHR design is 0.051 MPa. In
contrast, an average GCFR core subassembly, operating at a power density of 120 W/cc,
was cooled by a pressure drop of 0.29 MPa. The axial distribution of the GCFR pressure
drop is indicated in Table 4-15, which was taken from Reference 60. Note that 44% of the
GCFR subassembly pressure drop occurs in the active core region, in which the cladding
surface has been roughened to enhance heat transfer. If the GCFR subassembly were to be

cooled by a 0.051 MPa coolant pressure drop, then assuming the pressure drop is approximately proportional to the square of the flow rate, the new flow rate is $(0.051/0.29)^{1/2}$ = 42% of the original GCFR flow rate, if all other factors remain fixed. Thus, the ATW/GT-MHR pressure drop would provide 42% of the heat removal capability of the GCFR design, if the subassembly hydraulic characteristics (flow area, hydraulic diameter, length) remained the same.

A second consideration is the coolant pressure, which determines the size of the cladding-to-coolant heat transfer coefficient. Note that the GT-MHR operates at a pressure of about 7 MPa, compared to the GCFR pressure of about 10 MPa. The heat transfer coefficient is proportional to the 0.8 power of the Reynolds number, which is directly proportional to the density, and hence to the pressure through the ideal gas law. So the heat transfer coefficient is approximately proportional to the 0.8 power of the pressure. Taking the lower GT-MHR pressure into account reduces the GCFR heat removal by a factor of $(7.0/10.0)^{0.8}$ = 75%.

Consideration must also be given to changes in the hydraulic characteristics of the GCFR subassembly design. The overall GCFR subassembly length is 490 cm, considerably shorter than the GT-MHR core height of 793 cm. Extension of the GCFR pin length would increase the friction pressure drop in direct proportion to the length increase, and reduce the heat removal capability accordingly.

Assuming that the fast region has a volume equivalent to that of six standard fuel block columns, it can accommodate, by comparison to the GCFR characteristics, an average power density such that the total power of the fast region is roughly 26% of the total core power.

Table 4-14. Comparison of Reactor Design Characteristics

	GCFR	GT-MHR
Core Power, MW	1088	600
Coolant Pressure, MPa	10.5	7.07
Core ΔP, MPa	0.29	0.051
P_{avg}, W/cc	120.	6.6
P_{peak}, W/cc	180.	-
Core ΔT_{avg}, ^{o}C	232	360
Core Height, cm	120	793
He Flow, kg/s	949	320

Table 4-15. Pressure Drop in Various Parts of the GCFR Fuel Subassembly.

|	% P	Length, cm
Inlet	8.3	-
Lower Axial Blanket	4.8	60
Core Region (Roughened Cladding)	44.0	120
Upper Axial Blanket	7.0	60
Spacers	22.6	-
Acceleration	2.1	-
Outlet	11.2	-

4.7.2 The LANL Design

Whole core studies use 400-µm-diameter kernels with a 7.4% packing fraction. In order to achieve a 1000-kg actinide inventory in the core, an additional ring of fuel hexes was added to the GA point design, increasing the number of fuel hexes from 108 to 156. A two-dimensional MCNP model of this core design was developed. All features of the TRISO-coated fuel particles were modeled explicitly. Erbium poison was not used.

Burnup calculations were performed for two years in critical mode. Accelerator-driven subcritical operation followed for a period of one year. Various scenarios for the transition from critical to subcritical operation exist. The one chosen in this point design is a step reactivity insertion at the transition point that brings the initial subcritical core k_{eff} down to 0.97. In practice, this reactivity insertion might be effected via the insertion of control rods in the outer reflector region. For calculational expediency, this negative-reactivity insertion was simulated by adding boron to the outer reflector region. This boron was left for the first quarter of the subcritical burn, whereupon it was removed.

Results of the Monteburns burnup calculations are shown in Figure 4-29. The reactivity is somewhat flat during the two-year critical mode of operation, with an initial k_{eff} just below 1.05. The duration of the burn without erbium in the system is due to the Pu-240 in the fuel. It is, in a way, better than a traditional burnable poison because its destruction (via neutron absorption) creates fuel in the form of fissile Pu-241. The step decrease in reactivity at the transition between critical and subcritical operation is due to the addition of boron in the outer reflector, which simulates the insertion of control rods into this region. The boron is removed after 3 months of subcritical operation, leading to the observed jump in reactivity at this time.

Note two definitions of k are plotted during the subcritical mode of operation; the difference between them is the source definition. One is the classical k_{eff} that represents the multiplication factor when the source is fission neutrons distributed spatially throughout the fuel. The second, k_{acc}, represents the multiplication factor for a source of spallation neutrons distributed within the spallation target region, that is, within the center hex of the core. The

difference between k_{eff} and k_{acc} is indicative of the neutronic coupling between the spallation target and subcritical blanket. For purposes of calculating accelerator beam current required to sustain a specific blanket power, k_{acc} must be used. In this particular example, approximately 100 mA of 1-GeV beam would be needed to drive the transmuter at 600 MWth at the end of subcritical burn where k_{acc} = 0.77.
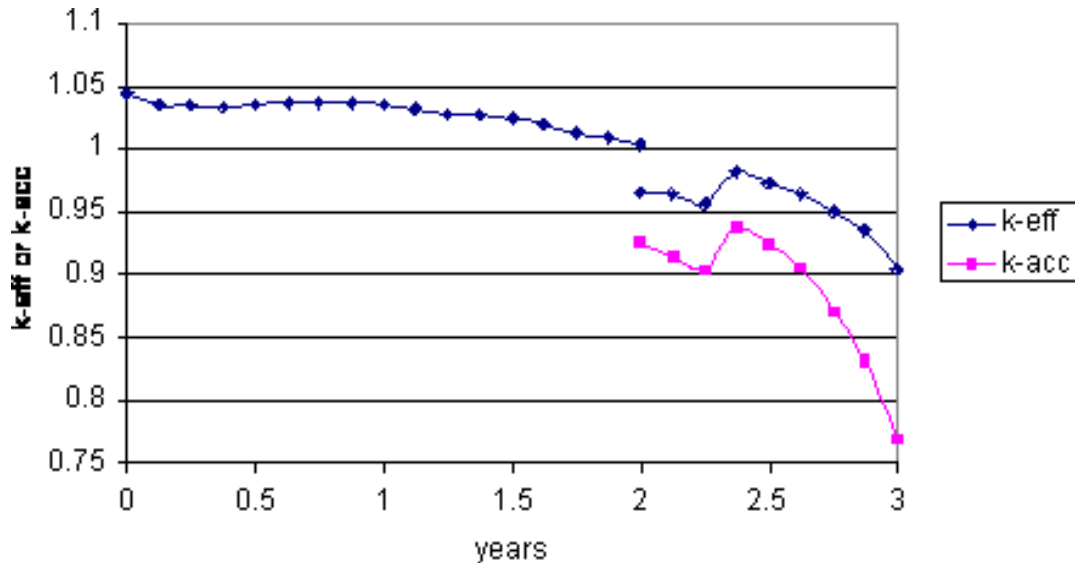
Figure 4-29.   Reactivity as a Function of Burnup for the Full Core Model

Actinide burnup over a six-year period for this point design is shown in Figure 4-30. Fuel remains in the outer thermal region for a three-year period (two years critical plus one year subcritical), at which time it is transferred to the inner "fast" region surrounding the spallation target. During the time the fuel reside in the thermal region, actinide destruction proceeds at a nearly constant rate of just over 200 kg/y. For the three-year period in the fast region, the burn rate of actinides is much lower, about 20 kg/y. As expected, plutonium is the primary transmuted element, while curium builds up in this mostly thermal system. In fact, the curium inventory continues to increase even after the fuel is transferred to the fast region because the spectrum in this region is actually largely thermal.
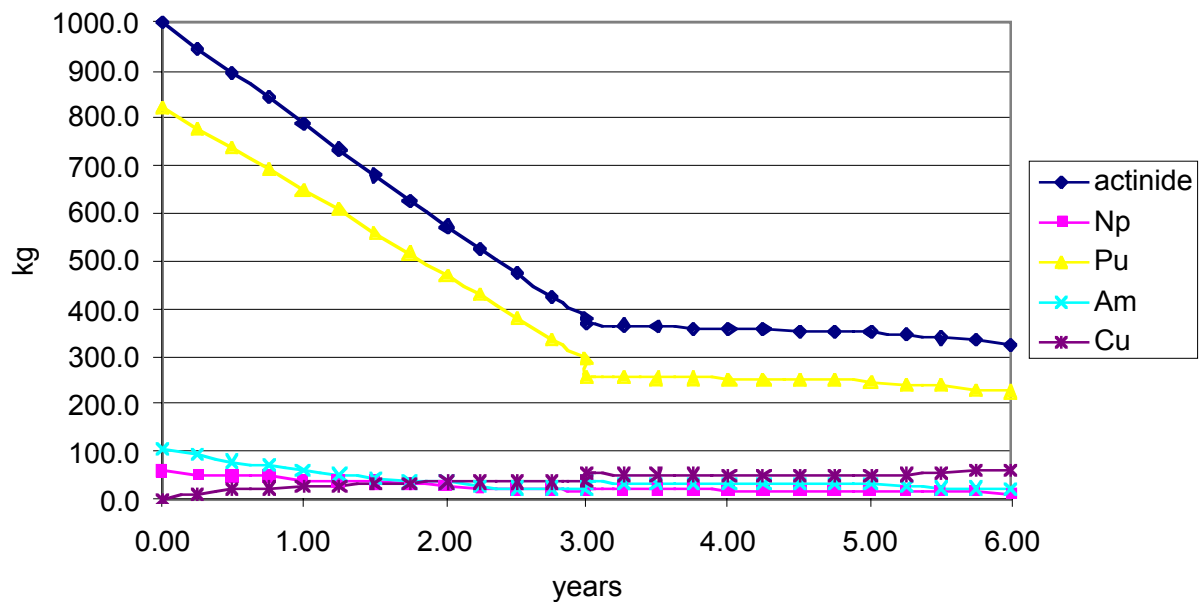
Figure 4-30. Actinide Burnup of the System Point Design over a Six-Year Cycle
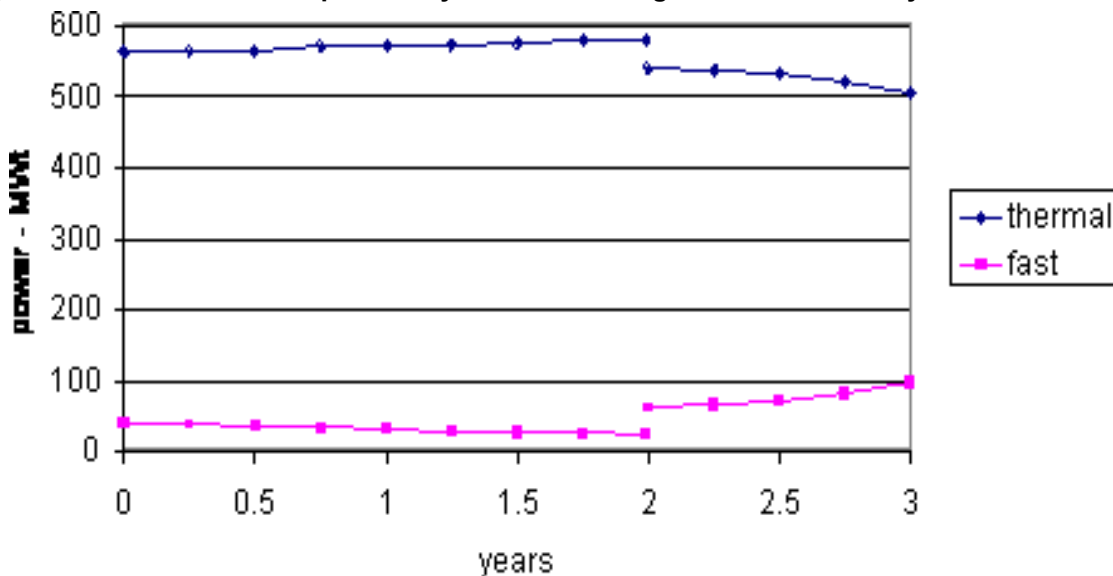
**Figure 4-31. Distribution of Power between the Thermal and Fast Regions as a Function of
Time**

The distribution of power between the thermal and fast regions as a function of time is
shown in Figure 4-31. During the critical portion of the burn most of the power, and hence
most of the actinide burning, occurs in the thermal region. A step increase in the power in
the fast region occurs when the system is driven by an accelerator in subcritical mode.
However, the power in the thermal region still dominates the total transmuter power.

Examination of the reactivity dependence on temperature shows the system has a strong negative temperature coefficient. Figure 4-32 shows k_{eff} as a function of operating temperature, both at the beginning of life (BOL), and at the end of the two-year critical burn (EOB).

Figure 4-32.   Dependence of Core Reactivity on Operating Temperature

4.8 Required Future R&D Activities

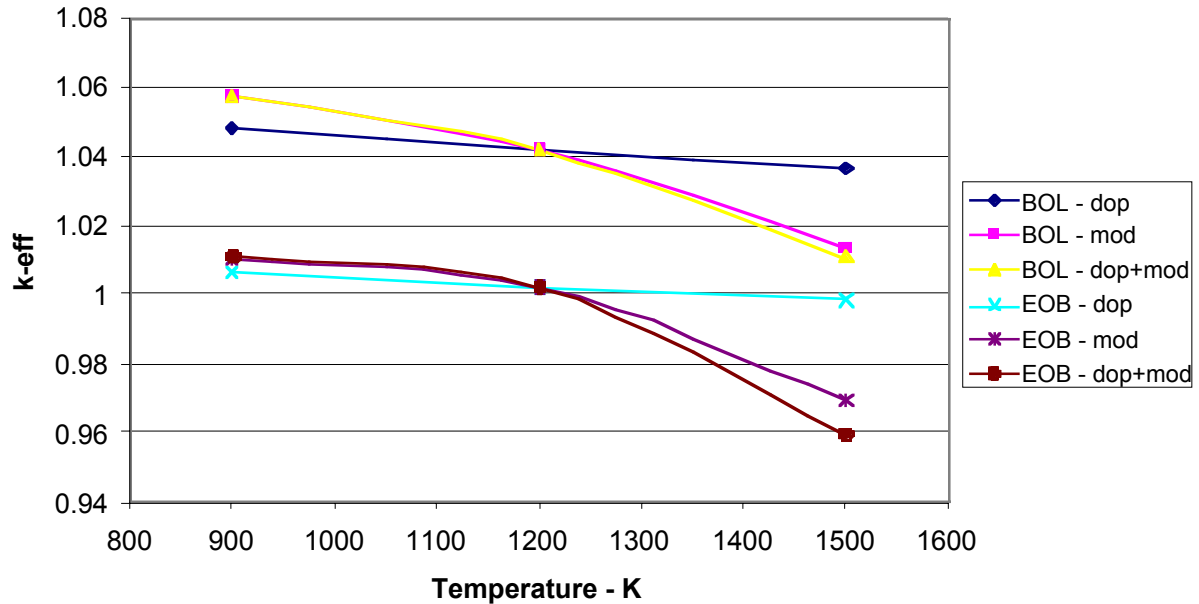The two point designs described in this chapter achieve very high plutonium burnup and significant Minor Actinides burnup while appearing to be operable. Nevertheless, the studies leading were very preliminary and did not address several potential issues:

4.8.1 Neutronic Optimization

While high burnups have been calculated for the discharge fuel, it was also observed that the final burning stage in the fast region was not very effective due to the relatively soft spectrum in the central fast region (this softening is due to the return of moderated neutron from the graphite reflector). Return of these neutrons could probably be prevented by adding thermal absorbers (such as boron, cadmium, or certain LLFP's) in the graphite blocks around the fast region. Nevertheless, this would not raise the fast flux in the central region, necessary for effective transmutation of the higher minor actinides. More efficient solutions have been discussed between ANL, GA, and LANL. One straightforward solution would be to adopt a double strata system, where a thermal (accelerator driven or not) gas-cooled transmuter would be used to burn as much plutonium as possible; the fuel would then be reconstituted (potentially after an intermediate reprocessing step) and introduced into an accelerator-driven GCFR for deep burning of the minor actinides. Separation of the fast and

thermal burning functions, while less elegant than the proposed GA approach, might avoid complex engineering issues. Another solution is to redesign the fast region within the proposed concept to make it a better neutron multiplier, thus generating its own sustained fast flux; this could be achieved by enlarging it and providing it with more fissile material for example from partially burned fuel.

Several paths have been identified for increasing the performance of the thermal region: for example lower inventories and larger particle sizes might result in deeper burnups, though the resulting shorter cycle lengths and potential power peaking might be an operational issue. Also, larger core outer diameters might result in higher performances, but at the cost of having to significantly improve the shielding characteristics of the outer reflector.

Control issues will need to be addressed: means to contain the initial excess reactivity need to be developed; furthermore, means to control the system reactivity, or the accelerator beam intensity, during the subcritical stage, need to be addressed. As much as possible, it seems desirable to obtain a flat reactivity profile during operations (in order to avoid excessive power peaking): this would give the preference to cores with large fissile inventories and elaborate fuel management schemes (for example, a long life core with several fuel batches).

No attempt has yet been made to find suitable modes for incinerating Long Lived Fission Products. Positions in the inner or outer reflector seem ideally suited for these tasks. Burning rates will need to be estimated and LLFP target design will need to be optimized.

4.8.2 Coolability

Coolability of the thermal and fast regions has been studied in a preliminary manner. For the thermal region, comparison of calculated average and peak power densities to those calculated by General Atomics indicate that the thermal region of the core is probably coolable; this needs to be verified by adequate calculations once a preliminary design has been developed.

Coolability of the fast region seems to be feasible, on average, but there is a serious danger of reaching very high peak powers close to the target. This region of the core seems particularly delicate to design, with a significant level of interaction between the fuel design and the target design. It should be noted that at this point, no design exists for either of these two components.

4.8.3 Safety

The original designs of the GT-MHR have achieved high levels of passive safety through the use of the TRISO coated fuel and the introduction of large masses of graphite which provide significant thermal inertia. Features added to the AD/GT-MHR require that a new safety assessment be performed: in particular, the fast region will have significantly lower thermal inertia, unless creative means are devised to either increase it (e.g. addition of matrix

material in the fuel); specific heat conduction paths could also be designed in the fuel subassembly to dissipate excess heat during safety transients.

Of more concern is the relatively large positive temperature coefficient observed at cold temperatures (see Figure 4-20). While it is not clear that there is a safety risk associated with that behavior, this issue needs to be addressed. Several neutronic design options can be utilized to reduce this positive value: for example the addition of erbium and the use of multiple fuel batching would both have beneficial effects.

4.8.4 Fuel Behavior

While the TRISO coated particles have been extensively tested in the past, they have never achieved the very high burnup required for the ATW program: the highest burnup achieved for Pu bearing fuels is 80% [62]. Furthermore, there is no experience fabricating TRISO coated particles with significant Minor Actinide contents, and delicate fabrication problems might occur, for example related to the volatility of Americium.

The reconstitution of the fuel into a fast assembly needs to be investigated. In particular, it is not clear whether the irradiated compacts can be integrally transferred to the fast region, potentially providing excessive neutron thermalization. In that case, the fuel particles would need to be separated from the graphite matrix, and recast into a form suitable for cooling in the fast assembly.

The fast assemblies and the fast region need to be designed to provide a high-energy spectrum, while maintaining coolability at all times. Means to achieve a fast spectrum have been discussed above. Coolability during normal operations will require designing the assemblies, potentially with enhanced cooling abilities, such as ribbed cladding; the definition of coolant pressure and flow rates needs to be studied. Off normal and accidental conditions need to be studied to provide for passive safety at all times. Several means to that end can be envisioned: for example, the addition of inert matrices would increase the fuel's thermal inertia; the use of thermal bridges would help dissipate decay heat during a loss of coolant accident.

In the current studies, it was assumed that the fuel would withstand the very high calculated burnups. Nevertheless, if the fuel performance could not be demonstrated up to these levels an intermediate reprocessing step (probably between the thermal and fast irradiation steps) would need to be devised. This would imply separating the TRISO particles from the graphite binder; mechanically or otherwise breaching the silicon carbide protective coating; dissolving and recuperating the fuel contents; and reforming a new fuel form.

The design of LLFP bearing elements will need to be assessed.

4.8.5 Target Design

The current system design leads to excessive power peaking in the fast region; this is due to the concentrated source used in the calculation, and also to the very low k_{eff} reached at the end of the subcritical cycle. Two R&D actions are required to alleviate this potential problem:

- The system design should be such as to keep a relatively high end of cycle k_{eff}

- The target and fast region designs need to be performed with the objective of spreading the source as much as possible.

4.8.6 System Design

The preliminary studies performed for this document have been constrained by the desire to maintain the design and operating conditions of the GT-MHR. There is no guarantee that these dimensions and operating conditions are optimal for the mission of burning transuranic waste. Global system optimization studies are needed to achieve this goal.

References

55. Private Communications, General Atomics, March 2000.

56. The ANSWERS Software Package, MONK—A Monte Carlo Program for Nuclear Criticality Safety and Reactor Physics Analyses, User Guide for Version 8, ANSWERS/MONK(98)6, AEA Technology, UK.

57. G. Marleau, *et al*., "A User's Guide for DRAGON," IGE-174, Rev. 3, Ecole Polytechnique de Montreal, Dec. 1997.

58. K. L. Derstine, "DIF3D: A Code to Solve One-, Two-, and Three-Dimensional Diffusion Theory Problems," ANL-82-64, Argonne National Laboratory, 1984.

59. W. S. Yang and H. Khalil, "Analysis of the ATW Fuel Cycle Using the REBUS-3 Code System," *Trans. Am. Nucl. Soc.*, 81, 277, 1999.

60. A. E. Waltar and A. B. Reynolds, Fast Breeder Reactors, Pergamon Press, 1981.

61. T. W. Chan, R. D. Pfremmer, and V. Tangirala, "Preliminary Transient Analyses of Gas Turbine Modular Helium Reactor (GT-MHR)," *Proceedings of the International Topical Meeting on Advanced Reactors Safety*, American Nuclear Society, Pittsburgh, Pennsylvania, April 17-21, 1994.

62. C. M. Miller and W.J. Scheffel, "Postirradiation Examination and Evaluation of Peach Bottom FTE-3," GA-906939, November 1975.

5 System Point Design Employing a Molten Salt Blanket

5.1 Introduction

Many ATW designs and proposals for the destruction of weapons-grade plutonium using an accelerator are based upon the use of a molten salt blanket and a liquid lead target [63]. In the ATW Roadmap [64], it was stated that molten salt and other liquid fuels have an advantage because of their ability to control burnup better than in other systems (i.e., burnable poisons are more effective at controlling reactivity change, and the ability to have continuous addition of fuel and removal of fission products allows the fissile to poison ratio of materials in the system to remain fairly constant). However, it was not listed as a potential target/blanket option and was not described in detail. This is because there are still quite a few unknowns associated with molten salt fuel, and it would require much research before it could be used. Despite this, research has continued on a molten salt ATW system. A recent design and proposal for using molten salt is called the Tier 1 approach [65]. This involves the continuous feed of molten salt-containing nuclear fuel into and out of the system without the need for separations (as has been necessary in previous designs). Even more effective burnup can be obtained by doing continuous removal of fission products (back-end separations), which controls the neutron fission-to-capture ratio in the molten salt and thus the value of the effective multiplication factor (k_{eff}).

Molten salt was recognized several decades ago as a potential medium for harvesting nuclear reactions. The first studies involving salt were conducted at Oak Ridge National Laboratory and comprised the Molten Salt Reactor (MSR) program from the 1950s to 1970s [66]. For this program, a mixture of LiF-BeF$_2$ salt surrounded by Hastelloy N (chosen for its corrosion resistance properties) containment was run in a reactor configuration. Though fairly resistant to corrosion, the Hastelloy N was not resistant to radiation damage and suffered helium embrittlement from (n,α) reactions. After the MSR was shut down, some materials modifications were made and tested (such as adding tellurium to the mixture) to increase resistance to radiation damage, but this affected the oxidation potential unfavorably. The advantages of molten salt that were discovered because of this program included good neutronic performance, high resource utilization, and good proliferation resistance. Additional studies on the molten salt system still need to be performed to optimize resistance to both corrosion and radiation damage while taking critical design considerations (mechanical strength, system operating temperature, type of protective environment, and oxidation potential) into account.

Since the work performed by Oak Ridge, other molten salt nuclear systems have also been developed. For example, an Accelerator Molten-Salt Breeder (AMSB) [67] was proposed, which involved using molten fluorides such as ThF$_4$ or UF$_4$ to breed plutonium. Studies have also been done on modeling the natural circulation of molten fluoride salt fuel [68] and establishing that molten nitrate salt is an efficient working fluid for generating electric power [69].

In addition, basic physics issues for both internally and externally moderated molten salt blankets [70] as well as chemical properties of fission product behavior in molten fluorides [71, 72] have been examined. Physics issues include burnup, reactivity temperature coefficients, and kinetics, while chemical characteristics include solubility, redox behavior, and chemical activity. From these initial studies, it was concluded that keeping fission products in the molten salt mixture (i.e., no removal) could be difficult both neutronically and chemically, so processing and recycling of fuel may be necessary for efficient future molten salt systems. Additional advances have been made in preparation and clean-up processes for fuel and carrier salts (front- and back-end electrochemistry) for molten salt accelerator-driven transmutation systems [73] and in pyrochemical/ pyrometallurgic processes, including reductive extraction, electrowinning, and electrorefining [74]. The cation exchange process has also been studied and optimized for recovering americium and plutonium from molten salt extraction residues [75].

Although the technology forms may not be as advanced as for other proposed target/blanket systems, molten salt has potential advantages that the other ones do not. As will be described later in this chapter, some advantages of molten salt are that its reactivity change is smaller, which reduces the accelerator power required to drive the transmuter, and the fuel is more proliferation resistant than in other methods. Disadvantages include its low fissile-to-capture ratio (leading to greater buildup of higher actinides as compared to fast-spectrum transmuters), lower neutron economy (making fission product transmutation difficult), and a potentially positive reactivity temperature coefficient. This document presents results for some of the basic aspects of a molten salt accelerator-driven system (ADS), but more accurate descriptions can be found in the other references mentioned here.

5.2 Results from Preliminary Neutronics Point Design Studies

Results from a representative molten salt system are given below. The main advantage of the molten salt system is that the value of k_{eff} remains constant as a function of burnup. This is because burnable poison (in the form of boron) can be employed effectively, whereas in the liquid metal systems, it cannot. The parameters for the molten salt system examined are:
- 5 meter diameter and height
- 90% Graphite, 10% Salt
- Continuous, not discrete feed
- Continuous fission product removal
- k_{eff} ~ 0.95 throughout cycle
- Initial Salt Composition
    - 66% LiF
    - 29% BeF
    - 5% ZrF$_4$–0.02w% TRUThe same initial and feed compositions were used

here as for the previous cases, and the total amount of actinide and Tc-99 destruction at the end looks higher for this case because it is a longer amount of time that passes. The burn rates of actinide and Tc-99 are shown in Figure 5-1, and the beginning and ending actinide inventories for molten salt are in Figure 5-2. The molten salt system has continuous feed of

actinides and removal of fission products and uranium, which means that it also achieves a
steady-state inventory of actinides (with no known worry of fluence limitations as are seen in
the lead-bismuth case). This corresponds to less final actinide waste than seen for the other
systems; actinides are just removed at the end of the system's lifetime; not throughout. It
also means that the feed rate is equal to the burn rate, which is why higher rates of burnup
can be achieved for this case. However, it must also be realized that the burnup achieved
without fission product removal will be significantly reduced.
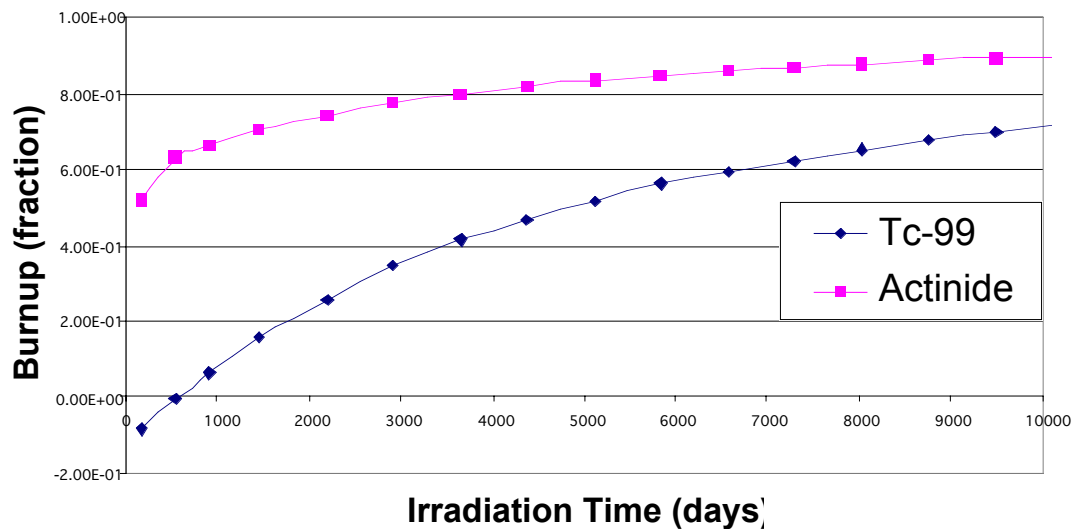
Figure 5-1.   Fraction of Destruction as a Function of Irradiation Time for Molten Salt

Also, due to a low neutron economy, it took a much larger amount of fission product (i.e. Tc-
99) initially to reach steady state in a reasonable amount of time than in the fast spectrum.
This "spiked" Tc-99 amount must be taken into account when comparing the system's
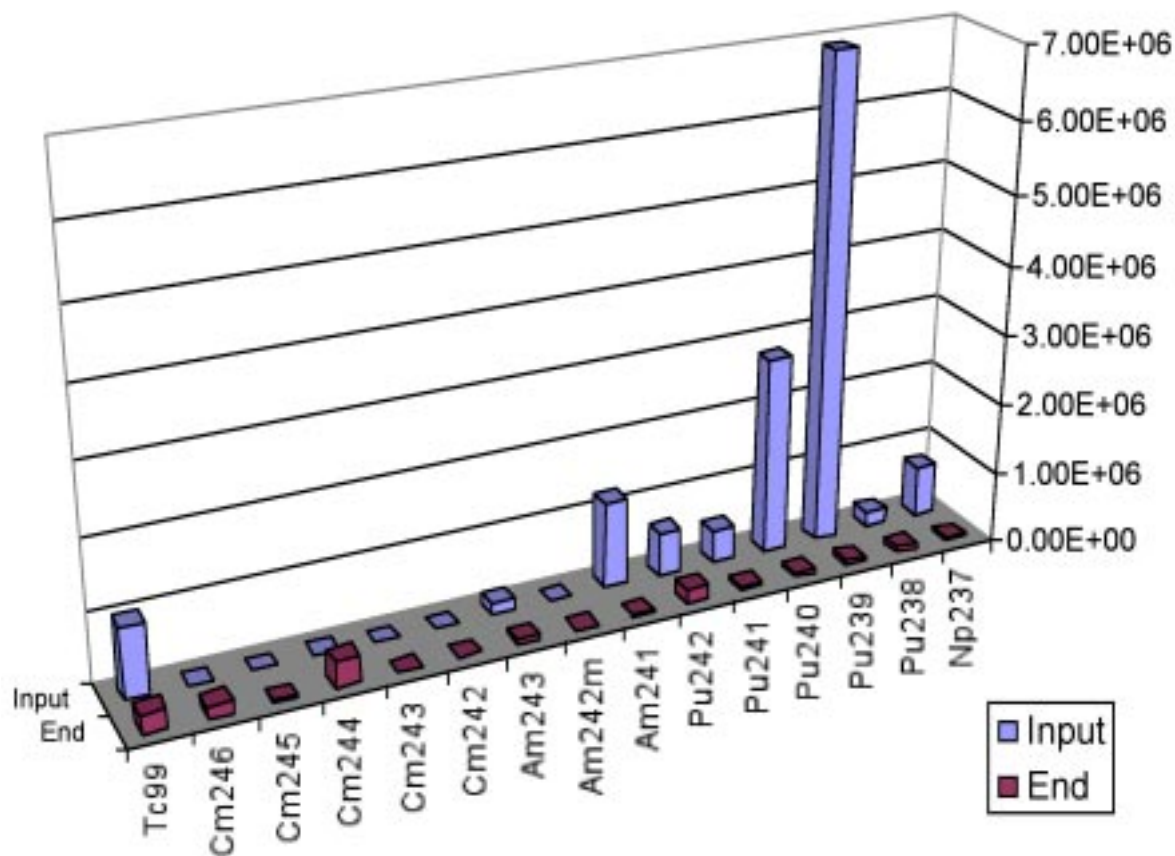effectiveness at burning fission products.

Figure 5-2.   Molten Salt Beginning and Ending Inventories

References

63. C. D. Bowman and F. Venneri, "High-Value Use of Weapons-Plutonium by Burning in Molten Salt Accelerator-Driven Subcritical Systems or Reactors", Los Alamos National Laboratory Report LA-UR-93-3077.

64. F. Venneri, *et al*., "A Roadmap for Developing ATW Technology: Target-Blanket Technology", Los Alamos National Laboratory Report LA-UR-99-3022, September 1999.

65. C. D. Bowman, "Once-Through Thermal-Spectrum Accelerator-Driven System for LWR Waste Destruction Without Reprocessing: Tier-1 Description," ADNA Corporation, ADNA/98-04, 1998.

References (continued)

66. J.R. DiStefano, *et al*, "Materials Considerations for Molten Salt Accelerator-Based Plutonium Conversion Systems", CONF-9407103-34, Oak Ridge National Laboratory, 1994.

67. N. G. Kenkyujo, "Single-fluid-type accelerator molten-salt breeder (AMSB)", JAERI-M-83-050

68. K. Mikitiouk, "Modeling of the Experiments with Natural Circulation of a Molten Fluoride Salt Fuel", P. A. Sterne, *et al*. (eds), *Actinides and the Environment*, Kluwer Academic Publishers, pgs. 191-194.

69. Sandia National Laboratories, "Sandia Technology, Volume 9, No. 4", SAND-85-0799.

70. M. G. Houts, *et al*., "Accelerator-Driven Molten-Salt Blankets: Physics Issues", Los Alamos National Laboratory Report LA-UR-94-3661, January 1995.

71. L. M. Toth, *et al*., "Molten fluoride fuel salt chemistry", Oak Ridge National Laboratory, CONF-9407103-28, 1994.

72. L. M. Toth, *et al*., "Review of ORNL's MSR technology and status", CONF-960639-6, Oak Ridge National Laboratory, 1996.

73. M. A. Williamson and F. Venneri, "Front-End and Back-End Electrochemistry of Molten Salt in Accelerator-Driven Transmutation Systems," *Global '95: Evaluation of Emerging Nuclear Fuel Cycle System*, Versailles, France, September 11-14, 1995.

74. N. Li, "Performance Estimates for Waste Treatment Pyroprocesses in ATW", Los Alamos National Laboratory Report LA-UR-97-0758, 1997.

75. G. H. Thompson, *et al*., "Chemistry research and development. Progress Report, July 1977–April 1978", RFP-2803, November 1978.

6 Interim Progress on Tokamak-Driven Transmutation of Spent Nuclear Fuel Waste

6.1 Background

Although the world's fusion scientists appear to be years or decades from achieving the conditions necessary to build an electricity generator powered by thermonuclear fusion, the same may not be true for transmutation applications or experiments. The requirement for "break-even" in a fusion reactor is to have an energy gain much greater than 1 (or Q>>1, where Q is fusion power produced divided by energy input to heat and contain a plasma). In a fusion transmuter, however, because of a large energy gain from fission in a blanket surrounding the fusion reactor, Q~1-2 may be sufficient for transmutation of all transuranics from spent fuel [76]. For transmutation of only minor actinides Q~10 may be sufficient, and Q~100 would be necessary for transmutation of some fission products.

Recent advances in tokamak engineering and physics and an expenditure of $750 million on research for an International Tokamak Experimental Reactor (ITER) have resulted in the belief inside the fusion community that these conditions (Q~1) could be achieved with high confidence. Based on this belief, Stacey and others have recently put forth a proposal for research to develop tokamak-driven transmutation of waste (TTW) from spent nuclear fuel. They produced a white paper early this year promoting transmutation as an intermediate objective for magnetic fusion research [77]. Then, in March, they submitted a recommendation to the ATW Subcommittee of the Nuclear Energy Research Advisory Committee (NERAC) to reconsider thermonuclear fusion as an alternative developmental path for transmutation [78]. Recent advances supporting this concept include fusion powers produced from deuterium-tritium fusion in excess of 10 MW in two large tokamaks: TFTR at Princeton Plasma Physics Laboratory and JET in Culham, England. This power level is on the order of the source strength needed to drive a subcritical transmuter experiment. In addition, plasma conditions sufficient for a fusion reactor have been achieved in other tokamaks, some of them smaller than TFTR and JET. Thus, Stacey *et al*. state "… there now exists a knowledge base sufficient to design tokamak reactors or neutron sources that with high confidence will achieve Q>>1." Because of these beliefs and statements, the ATW Project is examining the extensive literature on TTW so that we have a complete picture of alternatives to ATW.

As a basis for comparison of ATW and TTW, Krakowski previously reported a quantitative analysis of generic accelerator-based and fusion-based subcritical transmutation systems [79]. Much of the economic modeling (input data) in that method and other similar work has been made obsolete by an ongoing transition from a utility-based to a commercial nuclear power industry and the modernization of manufacturing, construction and construction management. However, the results of this and other studies are useful to give a feeling for comparative costs, advantages, benefits, and technological disadvantages. This work includes a quantitative listing of differences in configuration and operation between TTW and ATW systems.

An initial review of these and other references indicates that the physics and engineering issues to be addressed in a TTW program would be on the order of those of the ATW program, with different and possibly greater technological challenges. Some of these challenges are listed in the next section; this list will be expanded upon in further work for this phase of the ATW Project.

6.2 Technological Challenges

- Steady state operation has been identified in the ATW Program as a requirement for fuel and reactor longevity. This has not been demonstrated in any fusion device in existence, nor has the mechanism to produce steady state operation of any tokamak configuration. Demonstration may be necessary before considering fusion as an alternative.

- Transmutation rates may compete with tritium breeding (both require neutrons and blanket space), which is required for a sustainable fusion system.

- System lifetime under neutron radiation environments. Special materials (steels) may be required because of high neutron wall loading (>1 MW/m^2) or the forms of transmutation fuel or fission-product targets.

6.3 Analyses in Progress

In previous systems studies of generic concepts at Los Alamos requirements for TTW and cost tradeoffs have been analyzed, and several studies of specific tokamak designs or concepts have been reported by others. These studies are listed below and will be analyzed along with others for the final paper that details the prospects for TTW along with technological challenges.

6.3.1 Generic Studies

Numerous researchers have published generic studies relevant to TTW.
- "Fusion-driven transmutations of nuclear waste—a misconception or an incentive for promotion of fusion energy?" [80]
- "Magnetic fusion driven transmutation of nuclear waste" [81]
- "Tokamak transmutation of (nuclear) waste (TTW): parametric studies" [82]
- "Conceptual design of a fusion-fission hybrid reactor for transmutation of high level nuclear waste" [83]
- "Fusion neutrons transmutation of actinide wastes" [84]
- "Global physics approach to transmutation of radioactive nuclei" [85]
- "Prospect of nuclear waste transmutation and power production in fusion reactors" [86] "Waste transmutation and nuclear energy generation using a tokamak fusion-fission hybrid reactor" [87]

6.3.2 Point Designs and Concept Studies

There are also a few relevant concept studies and system point designs:
- "Transmutation of nuclear wastes in a fusion breeder" [88]
- "Spherical tokamak (ST) transmutation of nuclear wastes" [89]
- "Transmutation of fission products by high-field tokamak reactor with force-balanced coils" [90].

6.3.3 Other Materials

Two other publications that may be relevant are:
- "Recent progress in fusion reactor materials studies: Focus on transmutation and radioactivation aspects" [91]
- "Advanced nuclear energy systems without long-lived high-level waste." [92]

References

76. Cheng, E. T., "Transmutation of Nuclear Waste in Fusion Reactors," *Global '93: Proceedings of the International Conference and Technology Exposition on Future Nuclear Energy Systems: Emerging Fuel Cycles and Waste Disposal Options*, Sep. 12-17, Seattle, Wash., p. 1207-1251, 1993.

77. Stacey, W. M., D. E. Baldwin, R. R. Parker, and J. A. Schmidt, "Neutron Transmutation of Spent Nuclear Fuel—an Intermediate Term Objective for Magnetic Fusion," white paper, January 26, 2000.

78. Stacey, W. M., D. E. Baldwin, R. R. Parker, and J. A. Schmidt, "Neutron Transmutation of Spent Nuclear Fuel Using a Magnetic Fusion Neutron Source," Public Comment submitted to the Public Meeting on ATW held by the Nuclear Energy Research Advisory Committee in Albuquerque, NM, March 30, 2000.

79. Krakowski, R. A., "Tokamak Transmutation of (Nuclear) Waste: Preliminary Considerations and Comparisons," LA-UR-94-80, (check for proceedings of Meeting on Transmutation of Nuclear Waste in Small Driven Fusion Reactors, Dec 16-17, 1993, Del Mar, CA. 1994.

80. Taczanowski, S., G. Domanska, and J. Cetnar, "Fusion-driven transmutations of nuclear waste—a misconception or an incentive for promotion of fusion energy?," *Fusion Engineering and Design*, 41, Pt B, p. 455-460, Sep 2 1998.

81. Peng, Y-K. M., E. T. Cheng, "Magnetic fusion driven transmutation of nuclear waste," *Journal of Fusion Energy*, 12, no. 4, p. 381-384, Dec 1993.

References (continued)

82. Krakowski, R. A., E. T. Cheng, Y.-K. M. Peng, "Tokamak transmutation of (nuclear) waste (TTW): parametric studies," *Fusion Technology*, 26, no. 3 pt.2, p. 1207-1215, Nov 1994.

83. Qiu, L. J., Y. C. Wu, Y. W. Yang, Y. Wu, G. S. Luan, Q. Xu, Z. J. Guo, B. J. Xiao, "Conceptual design of a fusion-fission hybrid reactor for transmutation of high level nuclear waste," *Fusion Engineering and Design*, 25, no. 1-3, p. 169-177, Aug 1994.

84. Wong, C. P. C., E. T. Cheng, and K. R. Schultz, "Fusion neutrons transmutation of actinide wastes," *1991 IEEE International Conference on Plasma Science*, Jun 3-5, 1991, Williamsburg, VA, USA.

85. Salvatores, M., I. Slessarev, and M. Uematsu, *Nuclear Science and Engineering*, 116, no. 1, p. 1-18, Jan 1994.

86. Cheng, E. T. and R. J. Cerbone, "Prospect of nuclear waste transmutation and power production in fusion reactors," *Fusion Technology*, 30, no. 3, Pt 2B, p. 1654-1658, 1996.

87. Yican, W. and Q. Lijian, "Waste transmutation and nuclear energy generation using a tokamak fusion-fission hybrid reactor," *High Technology Letters*, 1, no. 1, p. 82-86, Jun 1995.

88. Feng, K. M. and G. Hu, "Transmutation of nuclear wastes in a fusion breeder," *Fusion Engineering and Design*, 41, Pt B, p. 449-454, September 2, 1998.

89. Peng, Y-K. M., E. T. Cheng, J. D. Galambos, and R. J. Cerbone, "Spherical tokamak (ST) transmutation of nuclear wastes," *Proceedings—Symposium on Fusion Engineering*, v.2, p. 1423-1429, 1995.

90. Tsutsui, H., H. Yamaguchi, J. Kondoh, S. Tsuji Iio, and R. Shimada, "Transmutation of fission products by high-field tokamak reactor with force-balanced coils," *Fusion Engineering and Design*, 41, Pt B, p. 431-436, Sep 2, 1998.

91. Garner, F. A., Greenwood, L. R., "Recent progress in fusion reactor materials studies: Focus on transmutation and radioactivation aspects," *Materials Transactions*, JIM, 34, no. 11, p. 985-998, Nov 1993.

92. Li, S., "Advanced nuclear energy systems without long-lived high-level waste," *Yuanzineng Kexue Jishu/Atomic Energy Science and Technology*, 31, no. 6, p. 558-567, 1997.

7   Electron Beam-Driven Transmutation

It is possible to drive a subcritical transmuter using an electron beam. In this concept, a powerful electron beam strikes a heavy metal (e.g., tantalum or tungsten) target located at the center of a subcritical core. A continuous spectrum of x-rays (bremsstralung) is created as the electrons are stopped in the target. Source neutrons are created when these x-rays subsequently participate in photonuclear reactions in the heavy-metal target.

The power requirements of an electron beam-driven system can be scaled from an existing electron beam-driven neutron source, the ORELA facility at Oak Ridge National Laboratory. This facility generates 10^{14} n/s with 50 kW of 180-MeV electrons [93]. The number of source neutrons required by a subcritical transmuter with k_{eff} = 0.97 operating at 1 GW of thermal power is 2.8×10^{18} n/s. Scaling from the ORELA facility, such a system would require a 1.4-GW electron beam. Thus, the thermal load in the target (1.4 GW) would exceed the thermal power generated in the blanket (1 GW). By contrast, a 1-GeV, 14-MW proton beam can drive this same transmuter.

The fact that an electron beam requires 100 times more power than a proton beam to produce an equivalent number of neutrons stems from the two-step process of first producing photons through atomic reactions, and then having these photons interact with target nuclei to release neutrons via low-probability photonuclear reactions. This process is much less efficient than the spallation process that ~1-GeV protons undergo for neutron production.

The huge power requirement of an electron beam precludes its practical implementation as a driver for subcritical transmuters. An additional complication arises from the mechanical and thermal-hydraulic design of a target whose heat load exceeds 1 GW. Such a target would be unreasonably large and expensive. For these reasons, electron beam-driven systems may be reasonably excluded from consideration for further research and development.

Reference

93. ORELA web site, http://www.phy.ornl.gov/orela/orela.html.